DISSERTATION | DOCTORAL THESIS

Titel | Title

In silico investigation of metal-free C-H activation processes in organic reactions

verfasst von | submitted by

Ricardo José Cruz Meyrelles

angestrebter akademischer Grad | in partial fulfilment of the requirements for the degree of

Doktor der Naturwissenschaften (Dr.rer.nat.)

Wien | Vienna, 2025

Studienkennzahl lt. Studienblatt | Degree programme code as it appears on the student record sheet:	UA 796 605 419
Dissertationsgebiet lt. Studienblatt | Field of study as it appears on the student record sheet:	Chemie
Betreut von | Supervisor:	Univ.-Prof. Dr. Dr. h.c. Leticia Gonzalez Herrero | Univ.-Prof. Dr. Nuno Maulide

The work presented in this doctoral thesis was conducted between August 2020 and August 2024 at the University of Vienna (Austria) under the supervision of Univ. -Prof. Dr. Nuno Maulide, Univ. -Prof. Dr. Leticia González and Dr. Boris Maryasin.

Referees:

Prof. Dr. Dean Tantillo

Dr. Per-Ola Norrby

Herewith, I would like to authenticate that I have written this thesis on my own. I have not used other resources, tools or assistance than those reported in this thesis.

Ricardo Meyrelles, August 2024

Zusammenfassung

Diese Doktorarbeit befasst sich mit der Untersuchung metallfreier C-H-Aktivierungsprozesse durch einen computergestützten chemischen Ansatz. Quantenchemische Berechnungen wurden durchgeführt, um bekannte und neue chemische Systeme zu untersuchen, mit dem Ziel, effizientere Methoden zur Funktionalisierung von C-H-Bindungen zu entwickeln. Die Arbeit gliedert sich in drei Hauptkapitel, die jeweils einem anderen Typ von C-H-Aktivierungsprozessen gewidmet sind.

Im ersten Kapitel werden Umlagerungsreaktionen in Karbokationensystemen untersucht, insbesondere Hydridverschiebungen. Karbokationen sind sehr instabile Spezies, und solche Hydridverschiebungen sind in der Regel schwer zu kontrollieren. Die rechnerische Arbeit in dieser Studie konzentrierte sich auf die Bewertung der mechanistischen Machbarkeit verschiedener Arten von Hydridverschiebungen in verschiedenen kationischen Substraten, mit dem Ziel, experimentelle Systeme zu entwerfen, in denen die Reaktivität leicht vorhersagbar und kontrollierbar ist.

Das zweite Kapitel erforscht Cyclopropanierungsreaktionen in kationischen Systemen. Der Schlüsselprozess bei solchen Transformationen wurde als die direkte Bildung einer nicht-klassischen Karbokationsspezies identifiziert, die in der Literatur als protoniertes Cyclopropan bezeichnet wird. Von diesen Spezies aus erfolgt die C-H-Aktivierung durch eine heterolytische Bindungsspaltung, die zur Bildung von Cyclopropanprodukten führt. Die mechanistische Untersuchung dieser Umwandlung ermöglichte das erfolgreiche Screening von Substraten zur Verbesserung der Effizienz kationischer Cyclopropanierungsreaktionen und erwies sich als zuverlässige Methode für die weitere Bewertung potenzieller Reaktionssubstrate.

Schließlich umfasst das dritte Kapitel die rechnerische Untersuchung eines neuartigen, komplexen photokatalytischen Systems, das die Alkylierung von Polyolen beinhaltet, wobei CO_2-Gas als Katalysator fungiert . In diesem System wurde die homolytische Spaltung einer C-H-Bindung als ein entscheidender Prozess für die Reaktionsgeschwindigkeit identifiziert. Die rechnerische Studie wurde durchgeführt, um Einblicke in die experimentellen Beobachtungen zu gewinnen, insbesondere um die Rolle der Komponenten im Katalysatorsystem zu klären. Der mechanistische Ansatz in dieser Arbeit

ermöglichte die Identifizierung einer intramolekularen Wasserstoffbrücke als Schlüsselfaktor bei der C-H-Aktivierung, die zu einem Wasserstoffatom-Transferereignis führt.

Abstract

This doctoral thesis focuses on the investigation of metal-free C-H activation processes through a computational chemistry approach. Quantum chemical calculations were performed to study reported and novel chemical systems with the aim of developing more efficient methods to achieve the functionalization of C-H bonds. The work is divided into three main chapters, each dedicated to a different type of C-H activation process.

The first chapter investigates the rearrangement reactions within carbocation systems, in particular, hydride shifts. Carbocations are very unstable species, and such hydride shifts are generally challenging to control. The computational work in this study focused on evaluating the mechanistic feasibility of different types of hydride shifts in different cationic substrates with the goal of designing experimental systems where the reactivity can be easily predicted and controlled.

The second chapter explores cyclopropanation reactions in cationic systems. The key process in such transformations was identified as the direct formation of a non-classical carbocation species referred to in the literature as protonated cyclopropane. From such species, the C-H activation occurs through a heterolytic bond cleavage that leads to the formation of cyclopropane products. The mechanistic study of this transformation allowed the successful screening of substrates to improve the efficiency of cationic cyclopropanation reactions and proved to be a reliable method for further evaluation of potential reaction substrates.

Finally, the third chapter encompasses the computational investigation of a novel complex photocatalytic system involving the alkylation of polyols in which CO_2 gas acts as a catalyst. In this system, the homolytic cleavage of a C-H bond was identified as a crucial process for the reaction rate. The computational study was carried out to gain insights into the experimental observations, specifically to elucidate the role of the components within the catalytic system. The mechanistic approach in this work allowed the identification of an intramolecular hydrogen bond as a critical factor in the C-H activation leading to a hydrogen atom transfer event.

Acknowledgements

Moving to a different country during the pandemic to start a PhD was no easy task. It would have been a lot harder (if not impossible) without the support of everyone that helped making this wonderful experience come true. I'd like to express my thanks to everyone that helped me through the different stages of this four and a half years:

I begin by thanking my three supervisors. I'm deeply grateful to Prof. Nuno Maulide for this opportunity. It was great to have an experimental supervisor that really cares and is enthusiastic about my work, and how it can help the research group. I also thank Prof. Leticia González who received me with open arms in her group, giving me shelter and an opportunity to learn and grow. I deeply thank Dr. Boris Maryasin, who provided an extremely close supervision (literally sitting next to me) and for having my back. He was always there, ready to help and encourage me.

To Dr. Daniel Kaiser and Dr. Saad Shabaan, who helped a lot with the organization of the projects and specially as bridge of communication to a very busy supervisor. To Patricia Emberger, who was always extremely helpful with all the administrative issues.

To Dr. Markus Oppel for all the assistance with cluster related troubles and also to Denis Hoxha, for all the support and for helping me "be famous".

To Prof. Luís Veiros, who shaped my knowledge of computational chemistry and reached out to Vienna to find me an opportunity to do a PhD. To Dr. Karina Shimizu, who accepted me as a graduate researcher in my first (paid) job.

To those who also helped with corrections of this long document: Dr. Patrick Zobel, Nóra Kovacs, Dr. Pedro Sanchez Murcia, Dr. Maren Podewitz and Dr. Eduarda Gil.

To all my collaborators. It gives me great joy that with every new project, the list of names would grow. With special mention for my "best customers" Dr. Jéremy Merad, Dr. Phil Grant, Dr. Anthony Fernandes and Dr. Manuel Schupp.

To the students who passed by my hands, and had to fight me in Akedo: Jan, Yener, Hannah, Isabel, Nóra, Olekssandra and Laurin,

I'm very happy to have been a part of two huge research groups, with very different dynamics. I'm grateful to all the nice people from the Maulide and the Gonzalez groups that I met across my PhD.

There are no words that can describe how thankful I am to my parents Jaime and Madalena, who dedicated their lives to love, guide and support me. The long-distance encouragement has always been very important and videocalls have made the distance easier to bear.

I'm grateful to Paulo and Rita, who also brought to life the most beautiful niece anyone could ask for. Mariana, who somehow managed to be born on my birthday, has brought new light to my life.

I'm also grateful to my grandmother Estrudinhas, who was not able to see this stage all the way through but was always proud of me, even not knowing what I was studying.

I'd also like to thank Vanda, who always had muslitos waiting for me, and has always been there to support me and Angela.

To my friends from Portugal: Joana, Diogo, Inês, Samuel, Ismael and Tomás and my "little" cousins Diogo, Leonor, Constança and Tomás, which I'm always happy to meet and have good time with.

This amazing experience was shaped by the great people I met here and I had a great time. And it is true that the real treasure is the friends you make along the way. To my dear friends, who brightened my days in the office: Patrick and Nóra, my favorite companions for boardgames and gossip; Boris and Veronika, who have been the closest thing to family since I moved to Vienna; Dilara and Dóra, my irreplaceable coffee/tea break buddies; Rahul, who still has to keep joining me for anime conventions; Vivien, the best neighbor one can have; my doctor-schwester Brigitta, Ludwig, Gaurab, David and Claudia, Thomas (to whom I still owe a transition state), Giuseppe "José" and FuLi. To my boardgame buddies Bogdan, HaoQi, Carlos, Immo, Irmgard. To the basketball team and the swimming team, that had to pose for the "If you have big feet, you can join us" video. To everyone that joined for football.

Setting up a Whatsapp group of 50+ people and successfully organizing a weekly football match was not easy, but I had a great time playing with all of you.

Last but foremost, I express my deep gratitude to Angela, who moved from Portugal for me and has always been there to cheer me through good and not so good times. Her companionship has been invaluable over so many amazing years.

A todos os que passaram pela minha vida e me ajudaram a chegar até aqui, muito obrigado.

Abbreviations and nomenclature

List of abbreviations

*p*Ka	Acid dissociation constant at logarithmic scale
3D	Three-dimensional
ACN	Acetonitrile
Aq.	Aqueous
Ar	Aryl
atm.	Atmosphere
B86	Becke86
BOA	Born-Oppenheimer approximation
BJ	Becke-Johnson
cat.	Catalyst
CCP	Cationic cyclopropanation
DAST	Diethylaminosulfur trifluoride
DBN	1,5-diazabicyclo[4.3.0]non-5-ene
DCM	Dichloromethane
DDQ	2,3-Dichloro-5,6-dicyano-1,4-benzoquinone
DFT	Density functional theory
equiv.	Equivalents
EWG	Electron-withdrawing group
FG	Functional Group
GGA	Generalized gradient approximation
H-bond	Hydrogen bond
h	Hours
HAT	Hydrogen atom transfer
HF	Hartree-Fock
HOMO	Highest occupied molecular orbital
HS	Hydride shift
*i*Pr	Iso-propyl
LA	Lewis acid
LDA	Local density approximation
LED	Light emitting diode
LUMO	Lowest unnocupied molecular orbital
m	Meta
*m*CPBA	*Meta*-chloroperoxybenzoic *acid*
Me	*Methyl*
min	Minutes
MP2	Møller–Plesset second order perturbation
NBS	*N*-Bromosuccinimide
NCS	*N*-Chlorosuccinimide
NIS	*N*-Iodosuccinimide
NMR	Nuclear magnetic resonance
NS-	N-succinimide anion
OH	Hydroxy
OMe	Methoxy

PBE	Perdew-Burke-Ernzerhof
PC	Photocatalyst
PCM	Polarizable continuum model
PCP+	Protonated cyclopropane
PES	Potential energy surface
Ph	Phenyl
PivOH	Pivalic acid
r.t.	Room temperature
s	Second
SC-XRD	Single crystal X-ray diffraction
SET	Single electron transfer
SMD	Universal solvation model based on solute electron density
TBHP	tert-Butyl hydroperoxide
*t*Bu	Tert-butyl
TfOH	Triflic acid
TI	Thorpe-Ingold
TISE	Time-independent Schrödinger equation
TST	Transition state theory
TS	Transition state
UV-vis	Ultraviolet-visible
Zn(Cu)	Zinc-copper couple

Nomenclature for figures and schemes in sections

In this thesis, the schemes are labelled as Scheme **A**-**X** and figures as Figure **A**-**X**. For both cases, **A** corresponds to a label of the current section and **X** indicates the number of the scheme or figure in the current section. A list of the used figure and scheme labels is presented in Table 1. For example, Scheme HS-2 is the second scheme of section 3.

Table 1 - Correspondence between the labels of schemes and figures and the section where they are presented.

Section number	**A** (section label)	Label spelling
1	I	Introduction
2	TB	Theoretical background
3	HS	Hydride shift
4	CCP	Cationic cyclopropanation
5	HAT	Hydrogen atom transfer

Nomenclature for structures presented in figures and schemes

Throughout this work, the structures presented in schemes are labelled as **SX-Y** in a general form. The "S" represents that this structure is shown in a scheme, X is the number of the scheme in the current section, and Y is the label of the individual structure. All the computed structures are labelled **FX-Y**, where "F" shows that this structure is presented in a figure, "X" is the correspondent number of the figure where such structure is first presented in the current section, and "Y" is again the label of the individual structure. The number "X" is not kept from section to section.

For instance, if there is a mention of a structure **S3-1**, it is the first one presented in the third scheme of the current section. Additionally, structure **S3-1** of section 3 is not the same as structure **S3-1** of section 4.

Table of contents

1. General introduction to C-H activation

Carbon-hydrogen bonds are highly abundant in nature and are present in a vast amount of organic compounds. These bonds present low reactivity due to a high bond energy (typically 90–100 kcal/mol) and low acidity (pK_a ranging from 45 to 60).[1] Cleaving these unreactive bonds to replace the hydrogen atom with a functional group of high chemical value is a process of great synthetic interest. However, such chemical transformations require processes that weaken the covalent C-H bond, commonly referred to in the literature as C-H activation.[2] A major challenge in organic synthesis involves not only the cleavage of C-H bonds but also the introduction of useful functional groups. The sequence of processes leading to the cleavage of the C-H bond and the introduction of a functional group is referred to in the literature as C-H functionalization (Scheme I-1-A).

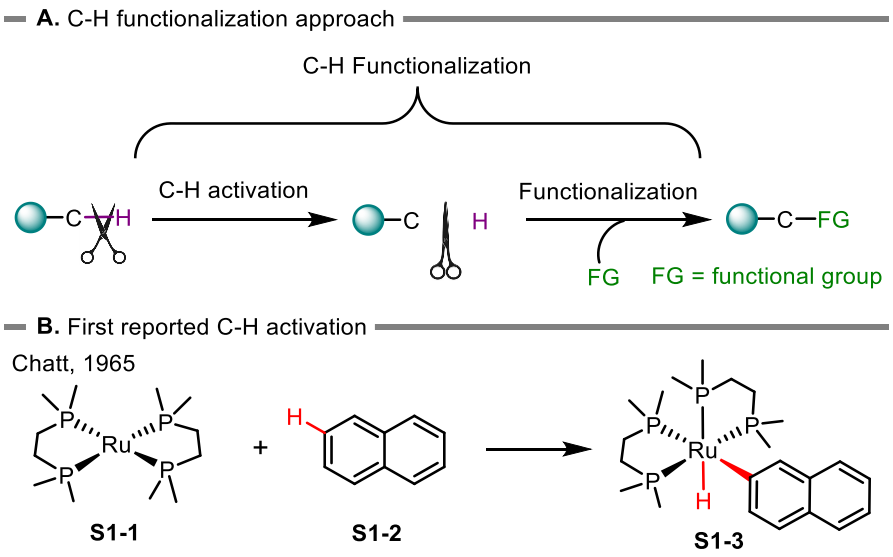

Scheme I-1 – A) Schematic representation of C-H functionalization processes; B) The first reported ruthenium-mediated C-H activation event.

The earliest published example of C-H activation was reported by Chatt and Davidson in 1965, depicting an oxidative addition of naphthalene to a ruthenium complex (**S1-1**), which results in the ruthenium (II) hydride complex **S1-3** shown in Scheme I-1-B.[3] Following this discovery, many metal-mediated C-H functionalization processes were developed. Some examples are represented in Scheme I-2 to highlight the ability of transition metal catalysts to cleave C-H bonds on both alkyl and aryl scaffolds, allowing the introduction of different functional groups to replace the hydrogen atom. Several C-H

functionalization processes were developed using palladium catalysts, alowing C-H functionalization reactions on a wide variety of scaffolds.[4,5] These include alkyl substrates such as **S2-1**, which contain C-H bonds that can be converted into carboxylic acid groups (**S2-1'**), and aryl C-H bonds that can be replaced with carbon-carbon bonds, as shown by Tremont and co-workers in the conversion of **S2-2** into **S2-2'** (Scheme I-2-A).[6,7] However, most of these methods depend on the reactivity of precious transition metals such as Pd, Ir, Rh, and Ru.[4,8]

Several advances in this field focused on combining C-H activation processes with carbon-carbon coupling reactions, allowing the connection of complex building blocks by exploiting an unreactive C-H bond. The ruthenium-catalyzed carbon-carbon coupling of **S2-3A** and **S2-3B** to yield **S2-3'** (Scheme I-2-A), as reported by Ouellet and co-workers, exemplifies this process.[9] One major downside of these approaches is reliance on second-row transition metal catalysts, which are very expensive, present low abundance on our planet, and often have high toxicity. Their industrial application is also problematic since the tolerated level of residual trace metal impurities is minimal in pharmaceutical compounds, organic electronic devices and crop-protecting agents.

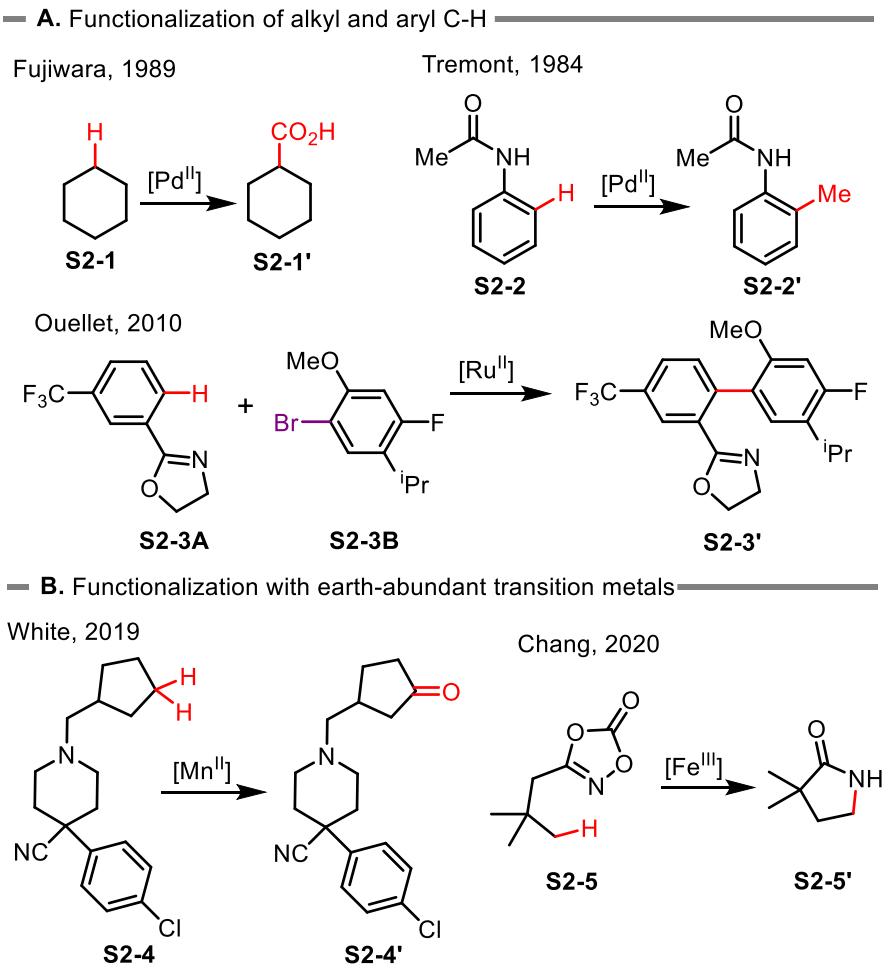

Scheme I-2 – Reported examples of metal-mediated C-H functionalization reactions: A) promoted by 4d transition metals; B) promoted by earth-abundant 3d transition metals.

In addition to the requirement of noble metals, typically harsh reaction conditions are required, such as high temperatures or the addition of strong oxidants. These conditions often limit the functional groups tolerated for the reaction substrates. Thus, metal-mediated C-H activation has not yet found widespread applications in synthesizing complex molecules and natural products. Many research groups have focused on developing C-H functionalization methods that involve mild reaction conditions to overcome these practical impediments. With this effort, earth-abundant 3d transition metal catalysts such as Sc, V, Mn, Co, Cu and Fe have experienced a strong demand for the development of this field. First-row transition metals are significantly less expensive and less toxic than second and third-row transition metals.[10] Examples of manganese and iron-catalyzed C-H functionalization are shown in Scheme I-2-B, demonstrating that these metals can also promote various C-H functionalization reactions. Such is the case of the oxidation of two cyclic alkyl C-H bonds into a ketone, converting **S2-4** into **S2-4'**, and

the C-H activation of primary alkanes, followed by intramolecular cyclization reactions, as demonstrated by Chang and co-workers with the conversion of **S2-5** into **S2-5'**.[11,12]

Although the use of earth-abundant transition metals still contributes to the advancement of sustainability in this field, their widespread application remains limited due to intrinsic issues associated with the nature of 3d transition metals. These metals present lower catalytic reactivity than their 4d and 5d counterparts and are more prone to oxidation in aerobic conditions. To overcome the lower reactivity, their use in catalysis generally requires adaptations in the reaction conditions, such as higher catalyst loadings, longer reaction times, higher reaction temperatures and, very often, the addition of sophisticated ligands which are not easily synthesized. Therefore, increasing the sustainability of C-H functionalization methods is still challenging for the organic chemistry community.

With a strong focus on tackling the issue of sustainability with metal-mediated C-H functionalization reactions, the development of metal-free C–H functionalization approaches has emerged in recent years as a green alternative.[13–15] The foundation of metal-free C-H activation lies in the process in which the C-H bond cleavage is not mediated by metal but instead induced through the manipulation of the intrinsic reactivity of the substrate. Examples of metal-free C-H activations are represented in Scheme I-3, depicting the activation of C-H bonds towards either homolytic or heterolytic cleavage.

The most common approach to metal-free C-H activation is to induce the homolytic cleavage of the C-H bond.[16] Such transformation can be achieved in the presence of free radical species, forming a carbon-centered radical. Due to their high reactivity, these radical species can be functionalized by reacting with electron-rich groups, such as olefins. One early example of such metal-free C-H functionalization was the discovery of the auto-oxidation of aldehydes, as reported by Caddick and co-workers in 2010.[17] The reaction of aldehydes with radical oxygen species leads to the homolytic cleavage of the C-H bond, forming an acyl radical **S3-1'** (Scheme I-3-A) that, upon reaction with an ethenesulfonate, forms **S3-1"**. The use of molecular oxygen to promote C-H functionalization has been developed with other substrates, such as ethers, benzylamines, and glycine derivatives, often requiring a pressurized O_2 environment. This radical-induced hydrogen atom transfer (HAT) has also been developed with

commonly used oxidants like 2,3-Dichloro-5,6-dicyano-1,4-benzoquinone (DDQ) and tert-Butyl hydroperoxide (TBHP).

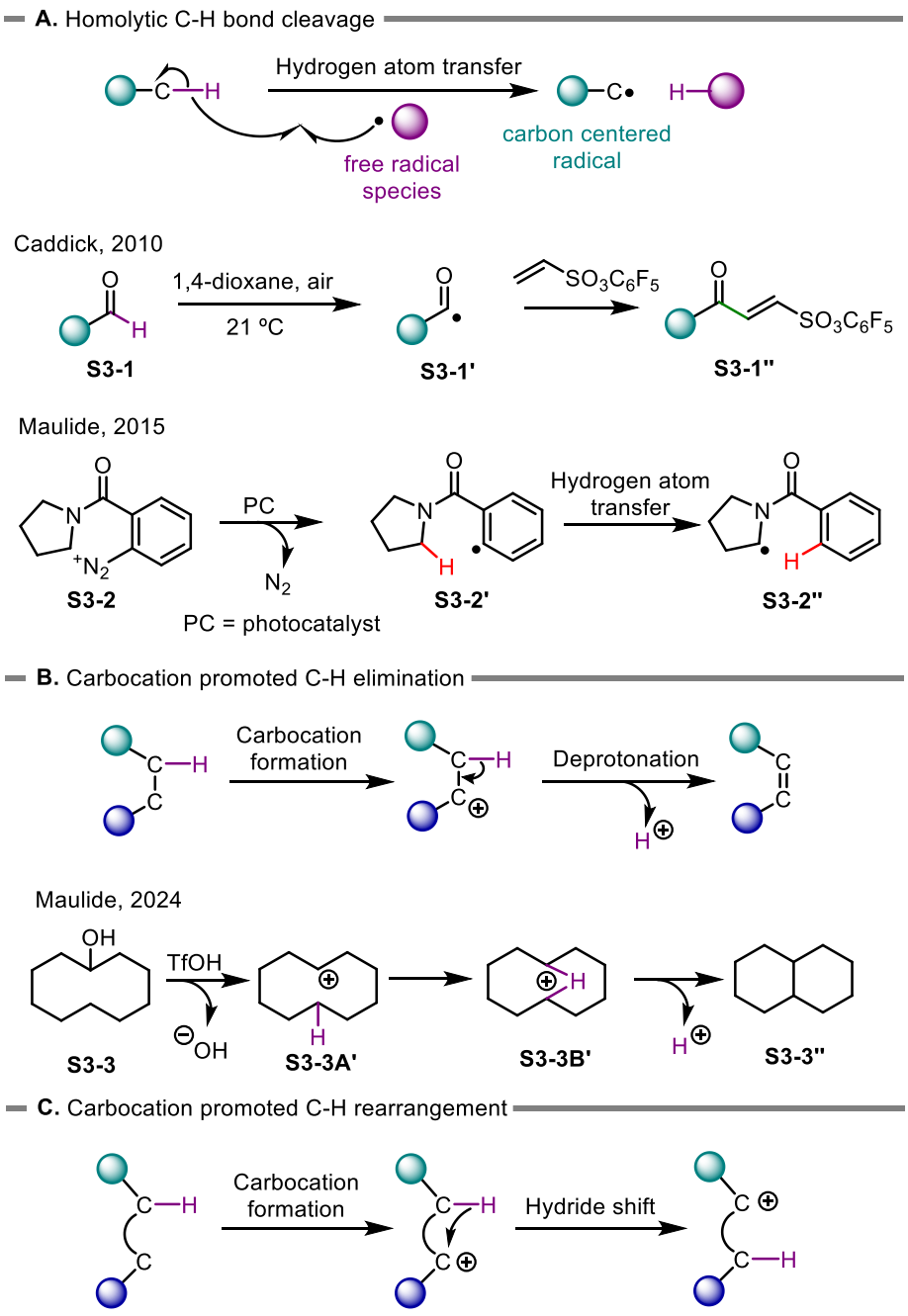

Scheme I-3 – Schematic representation of metal-free C-H activation processes: A) Radical process involving homolytic cleavage of the C-H bond and reported example; B) Cationic process leading to the heterolytic cleavage of a C-H bond through a proton transfer; C) intramolecular rearrangements of C-H bonds in carbocations (hydride shifts).

Further exploration of this reactivity led to the design of complex catalytic systems in which the radical species that performs a HAT step is generated *in situ* through electrochemistry or light-activation of photocatalysts.[18] One recent example of light-activated C-H activation was reported by the Maulide

group, in which a diazo-containing substrate **S3-2** forms an aryl radical **S3-2'** by releasing molecular nitrogen (Scheme I-3-A).[19] This radical species **S3-2'** then undergoes a HAT step in which a C-H bond is cleaved homolytically, leading to a more stabilized alkyl radical **S3-2"** that can be further functionalized in the reaction media. Although the overall process is not metal-free due to the use of a photocatalyst, it is important to note that in these reactions, the C-H activation step itself does not occur with metal mediation. This feature enables the exploration of efficient photocatalysts without requiring metal catalysts to activate C-H bonds, thereby enhancing the sustainability of the synthetic process.

Another approach to promote metal-free C-H activation is through the *in situ* generation of carbocations (Scheme I-3-B and C). These species are ions with a positively charged carbon atom. Carbocations are highly reactive species since the charged carbon atom only contains six electrons in its outer valence shell and needs two more to complete the octet. Consequently, if the positively charged carbon atom is adjacent to a C-H bond, heterolytic cleavage of this C-H bond can occur, leading to the formation of an additional carbon-carbon bond and the release of a proton, as shown in Scheme I-3-B.

One recent successful application of such a method was reported by the Maulide group with the C-H activation of cyclohexanes.[20] The abstraction of the hydroxyl group from cyclodecanol **S3-3** by reaction with trifluoroacetic acid (TFA) leads to the formation of a 10-membered ring carbocation **S3-3A'**. This intermediate forms an additional C-H bond across the ring to increase the stabilization of the carbocation, generating the bridged cationic intermediate **S3-3B'**. Such cationic species are very acidic and, therefore, able to undergo a heterolytic C-H bond cleavage. In this transformation, one proton is eliminated, and a *trans*-annular C-C bond is formed to yield the decalin product **S3-3"**.

Carbocations are very unstable species that can undergo intramolecular rearrangement processes to increase their stability. In such processes, an atom or substituent group bound to a carbon migrates to the carbon in which the cationic charge is located. These transformations are a common feature of carbocation chemistry and usually occur through the migration of a methyl group or a hydrogen atom. The latter case is referred to as hydride shift and is schematically represented in Scheme I-3-C. After the generation of a carbocation, a C-H bond can migrate to another carbon atom, resulting in an exchange between a C-H bond and a cationic charge. Hydride shifts are essentially C-H activation processes since

they cause an unreactive C-H bond to be dissociated. One challenge of controlling the selectivity of such reactions is related to the unstable nature of carbocations, which can lead to the occurrence of undesired side reactions.

Considering the significant benefits of metal-free C-H functionalization processes, which are promising but not yet well developed, quantum chemical calculations are essential to understand the key factors governing reactivity to predict more efficient new processes. It is worth noting that metal-free C-H activation processes involve the formation of highly unstable intermediates, such as radicals and carbocations, which cannot be isolated and only in rare cases can be detected experimentally. Therefore, the combination of experimental and computational studies can drive the development of this field towards new and efficient chemical transformations that exploit unreactive C-H bonds. While scarce computational work has been performed to study such metal-free C-H activation reactions, most reported examples focus on radical pathways.[21,22] Thus, further development of our knowledge on this topic through computational chemistry approaches is extremely useful to contribute to the fundamental understanding of these transformations, paving the way for future applications while also shedding light on the potential limitations of experimental methods.

This work was focused on the computational study of metal-free C-H activation processes is divided into three chapters, corresponding to sections 3, 4 and 5.

The first chapter (section 3) addresses C-H activation through hydride shifts in alkyl carbocations. Such transformations exploit intramolecular rearrangements to promote the migration of C-H bonds, allowing functionalization reactions to yield products with higher chemical value. Part of this work, focusing on a [1,5]-hydride shift step occurring in the Lewis acid-mediated coupling of alkenes and aldehydes, has recently been published in ChemPlusChem (List of publications section, entry 15).

The second chapter (section 4) focuses on the formation of cyclopropane-containing products through the control of heterolytic C-H bond cleavage steps. As the direct synthesis of cyclopropane rings is a current challenge in chemical synthesis, this work tackles cyclopropanation events through the generation of key carbocation intermediates and subsequent C-H activation steps. Most of the presented

results have been published in the Journal of American Chemistry Society in 2023 (List of publications section, entry 6).

Finally, in the third chapter (section 5), the mechanism of a C-H activation step within a ternary catalytic system is explored. The developed reaction of diols or alcohols with a terminal alkene involves a rate-limiting hydrogen atom transfer step, which is facilitated by the incorporation of CO_2 in the reaction media. The effect of this CO_2 incorporation was investigated through mechanistic studies, allowing the interpretation of the available experimental results. The presented investigation has partly been published on Angewandte Chemie in 2024 (List of publications section, entry 10)

2. Theoretical background

2.1. Quantum chemical methods

Computational chemistry is a field of study that lies in the interface of experimental and theoretical chemistry.[23] It relies on applying methods developed in theoretical chemistry to a wide range of chemical systems through the use of specialized software. The main objective of computational chemistry approaches is to understand key factors of experimental observations. Many chemical properties can be studied *in silico* to provide additional information on the system, such as the thermodynamic properties and key factors affecting the selectivity of a reaction or spectra of chemical compounds.[24] Importantly, the results obtained from computational chemistry approaches greatly assist the interpretation of chemical results and lead to the improvement of experimental conditions, guiding future experiments.[25,26]

Over the past decades, there have been astounding advances in the available computational power, allowing the use of increasingly complex theoretical methods for ever-larger chemical systems. As a result, a widely used approach of computational chemistry became the employment of quantum chemical calculations to study the mechanism of chemical reactions, namely how reagents are converted step-by-step into the observed products. This approach is called mechanistic study and has the value of shedding light on how the reaction occurs, which factors affect the reaction outcome, and what conditions favor the formation of the desired products. Additionally, many reactions involve the formation of unstable intermediates that are difficult to isolate or characterize experimentally and can only be studied computationally. Performing computational mechanistic studies can, therefore, help enhance the experimental efficiency, identify reagents that will not be active, and, more importantly, predict other reactions that have not been performed but have a high chance of being successful.

Mechanistic studies require the use of quantum chemical methods, which are based on solving the time-independent Schrödinger equation.[27]

$$\hat{H}|\Psi\rangle = E|\Psi\rangle. \quad (1)$$

In Equation 1, E is the total energy of the system, Ψ is the wavefunction and $\hat{H}$ is an operator called Hamiltonian. For a system with several nuclei and electrons, the Hamiltonian results from the kinetic and potential energy contributions of all these particles. As a first approximation, one can often treat the motion of the nuclei and the electrons independently, as done in the Born-Oppenheimer approximation (BOA). This is possible, as electrons are much smaller than the nuclei and thus move much faster and therefore the motion of the electrons can be described for a set of fixed nuclei.[28] Thus, the kinetic energy of the nuclei can be neglected, and the repulsion between nuclei becomes a constant. From this approximation, potential energy surfaces (PES) can be obtained, which describe the energy of the system in terms of the position of the nuclei. The BOA is usually justified when the electronic potential energy surfaces of different electronic states are well separated in energy which is the case for most thermally activated reactions in the ground state, such as the ones studied in this work. Still, the TISE cannot be solved analytically for systems that contain more than one electron and therefore several approximations to solve this equation have been developed over the last century. Among the simplest of these approaches is the Hartree-Fock (HF) which simplifies the electron-electron interactions by replacing them with an average field created by all other electrons.[29] This method is robustly implemented in many widely available quantum chemistry software packages. However, the lack of electron correlation resulting from the mean-field approximation causes a significant penalty in the accuracy of HF and can restrict its use in computational studies aiming to support experimental data. [30] Further development of this approach gave rise to post-HF methods, such as e.g., Møller–Plesset perturbation theory,[31] which present very high accuracy and a significant increase in the computational cost. The latter is often a limiting factor for their application in the study of large chemical systems. As a result, mechanistic studies of chemical reaction often require the use methods that can present a good compromise between accuracy and computational cost. Such is the case of density functional theory (DFT) methods, which were mostly used in the presented work.

DFT has emerged during the past decades as a powerful methodology for the simulation of chemical systems, as it can greatly surpass the accuracy of Hartree-Fock without increasing the computational cost.[32] DFT is based on the two Hohenberg-Kohn theorems.[33] The first theorem states that the ground-

state properties of a system is a functional of its ground-state electron density. The second theorem establishes that the density obeys a variational principle, which states that the ground-state energy is minimized by the ground-state electron density. Therefore, the basis of DFT is to calculate the energy and other properties from the density rather than from a wavefunction. The ground-state energy of a system can then be obtained through the following equation:

$$E[\rho] = -\sum_{X=1}^{N} \int \frac{Z_x}{r_{Xi}} \rho(r_1) dr_1 - \frac{1}{2} \sum_{i=1}^{n} \int \Psi_i^*(r_1) \nabla_i^2 \Psi_i(r_1) dr_1 + \frac{1}{2} \iint \frac{\rho(r_1)\rho(r_2)}{r_{12}} dr_1 dr_2 + E^{XC}[\rho], \quad (2)$$

In equation 2,[34] ρ is the electron density, r_1 and r_2 are spatial coordinates, n is the number of electrons of the system and N the number of nuclei. The Kohn-Sham orbitals (Ψ_i (i = 1, 2, ..., n) can be described by a finite set of basis functions (basis set).[35] Many basis sets have been developed to this date, which can be constructed from different types of functions (such as slater or gaussian functions) and their size directly affects the accuracy and the computational cost of the method. The employment of very large basis sets typically leads to accurate results at the expense of a significant increase in computational cost. It is therefore important to select a suitable basis set according to the size of the chemical system in study. As mentioned above, equation 2 yields the ground state energy of a system from its electron density. The first three terms of this equation can be interpreted as the interactions between nuclei and electrons, the kinetic energy of the electrons and the Coulombic repulsions between the electrons, respectively. The last term of equation 2, the exchange-correlation energy (E^{XC}), is unknown and represents a correction to the repulsion between electrons and the kinetic energy. The main focus in DFT method development has therefore been the design of approaches to obtain E^{XC} with good accuracy. One of the simplest is the local density approximation (LDA).[36] In this approach, E^{XC} is considered to depend only on the electron density, which typically delivers moderate results. Further development of LDA led to the generalized gradient approximation (GGA), which considers that the exchange-correlation energy also depends on the gradient of density.[37,38] The development of GGA methods has led to widely used functionals such as BLYP,[39,40] based on the numerical fitting of parameters to match data sets of measured atomization energies of organic molecules, and Perdew-Burke-Ernzerhof (PBE)[41] or Becke86 (BP86)[39,42], that were developed from basic principles derived from quantum mechanics.[32] Among the exchange functionals based on this principle are In general, GGA methods provide much

more accurate results than LDA. [43] However, these are often not enough for a qualitatively correct description of many chemical aspects of molecules, such as reaction energies. The modern development of DFT methods encompasses the design of both exchange and correlation functionals to provide more accurate energies and other molecular property values from the electron density, leading to a wide plethora of available DFT functionals have been developed for specific purposes.

Specifically for the case of computational studies of reaction mechanisms, hybrid density functionals are widely used. These functionals incorporate a portion of HF (or exact) exchange in the exchange term, often determined through semi-empirical fitting. Notable examples of hybrid density functionals are B3LYP[44] and PBE0.[41] B3LYP includes 20% of HF exchange and contains parameters determined by fitting to a data set of measured atomization energies of organic molecules. This *ad hoc* parametrization makes B3LYP very accurate for chemical systems similar to those in the parametrization set. This is not the case for PBE0, which is a nonempirical hybrid functional that includes 25% HF exchange and provides accurate results for more complex chemical systems containing, for instance, transition metals. It is then important to keep in mind that the nature of DFT functionals can often reflect on the obtained computational results, and an appropriate computational model must be selected for the chemical system in study. A particularly important consideration is that B3LYP is known to be unsuitable for obtaining accurate structures of carbocations,[45,46] and, therefore, PBE0 was used for most of this work.

Although the accuracy of hybrid GGA methods is high, they still cannot correctly describe non-covalent interactions, especially London dispersion interactions. A widely used approach to overcome this issue is the use of the D3 correction, proposed by Grimme and co-workers in 2006, in which an empirical pair-wise dispersion term is added to the DFT energy.[47] The inclusion of this empirical term in does not pose a significant increase in the computational cost and can provide more accurate results for energies. This method was further developed by introducing damping functions, such as the Becke-Jhonson damping, [48] that ensure accurate short-range behavior of the dispersion correction, reducing the double-counting effects of electron correlation at intermediate distances.

2.2. Procedure for computing energies

Applying quantum mechanical methods to study a chemical system almost always involves an initial geometry optimization. In this process, the nuclear coordinates of the system are changed iteratively, given a certain convergence criterion, until a geometry that yields the lowest energy value is achieved. The geometry optimization is based on the gradient of the energy (first derivative of energy with respect to nuclear coordinates), ensuring that the forces acting on the nuclei approach zero. The resulting geometry (nuclear coordinates of all the atoms of the chemical system in study) is an energy minimum, and the displacement of any nuclei, in any spatial coordinate increases the energy of the system, therefore destabilizing the equilibrium structure. Computing the second derivative of the energy with respect to the nuclear coordinates yields the normal vibrational modes of the system and their frequency. In order to characterize any computed structure as a minimum of energy, it is also required to verify that all the vibrational modes present positive frequencies, which determine that the current geometry is a minimum along every single vibrational mode. The computed vibrational modes can be used to determine thermodynamic properties, such as the corrections to Gibbs free energy of the system.[49,50] This correction term can be added to the electronic energy of the system to yield the Gibbs free energy of the computed structure.[51]

Very often, the resource and time costs of calculations at high levels of theory are not feasible within the available timeframe of a computational project. To overcome these limitations, one efficient approach to enhance the accuracy of computed results is to extrapolate the energy of structures, optimized using a less accurate and cheaper method, to a higher level of theory.[52,53] This approach is exemplified in Scheme TB-1-A.

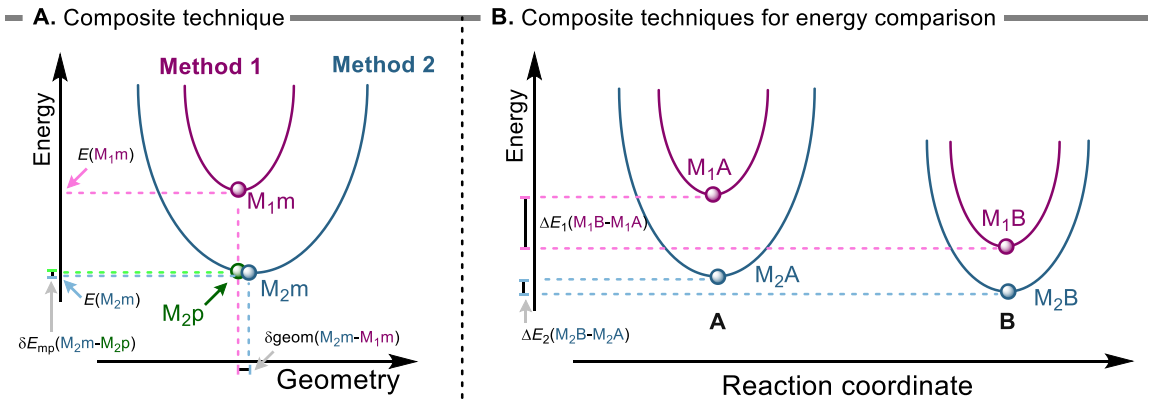

Scheme TB-1 – A) Representation of the procedure used for computing energies; B) Schematic representation of the outcome from energy comparison of different structures with this method.

Following this scheme, a minimum energy structure **M₁m** is obtained using method 1. This structure corresponds to the energy value of E(**M₁m**). If the same species is optimized using method 2, a more accurate and computationally expensive method, the minimum energy structure **M₂m** is obtained, corresponding to the energy value of E(**M₂m**). Typically, geometries are less sensitive than energies to the chosen computational method and thus, to avoid costly geometry optimization, the structure's energy obtained with method 1, **M₁m**, can be computed with method 2 using a single-point energy calculation. This results in a vertical projection of **M₁m** onto the potential energy surface of method 2, yielding an **M₂p** state, which has the same geometry as **M₁m** but with the energy E(**M₂p**). If method 1 provides accurate geometries, the difference between the geometries of **M₂p** and **M₂m**, δgeom(**M₂m-M₂p**), will be negligible. Consequently, the difference between E(**M₂p**) and the energy obtained after the full geometry optimization with method 2, E(**M₂m**), represented in Scheme TB-1-A as δE_{mp}(**M₂m-M₂p**), will also be negligible. Therefore, it is possible to approximate the structure's energy as if it were optimized with method 2 by simply performing a single-point energy calculation using method 2 on the structure optimized with method 1. This approach, commonly denoted in the literature as method 2//method 1, can significantly influence the energy profiles, as shown in Scheme TB-1-B. In this example, computing the energy difference between species **A** and **B** could lead to a large error if only the energies from method 1 are considered. In similar cases where ΔE_1(**M₁B-M₁A**) is significantly different than ΔE_2(**M₂B-M₂A**), applying the discussed procedure to compute the energies at the method 2//method 1 level of theory allows a cost-effective way to approach the value of ΔE_2(**M₂B-M₂A**), using

geometries obtained with a cheaper method 1. Throughout the current work, such an approach has been used to yield more accurate energy profiles while maintaining a reasonable computational cost.

2.3. Solvation effects

A significant challenge in modern computational chemistry is accurately accounting for solvent effects in modelled systems. In an experimental system, interactions between solute and solvent molecules, such as hydrogen bonds (H-bonds), van der Waals, and electrostatic interactions, substantially influence many of the system's properties. However, including these effects in the computational model is not trivial. Currently, implicit and explicit solvation methods are widely used to describe the solvation effects.

Implicit solvation methods involve modelling the chemical system within a solvent cavity that interacts with it through its electrostatic potential. The solvent is, therefore, represented implicitly, and only bulk solvent effects are accounted for. This approach presents a low computational cost and is, therefore, a very good choice for studying chemical systems that use aprotic solvents. The polarizable continuum model (PCM) is a widely used implicit solvation method.[54] Continuum models rely on defining a boundary between the solute and the bulk of the solvent, which is represented as a structureless polarizable medium characterized by its dielectric constant. This boundary between solute and solvent is named solvent excluding surface and is used to compute the electrostatic, and cavitation contributions of the free energy. The sum of these three energies yields the Gibbs free energy of solvation of the computed system. Continuum models have been further parametrized to increase the accuracy of the computed free energies of solvation, resulting in improved models such as the "Universal Solvation Model Based on Solute Electron Density" (SMD), developed by Truhlar and co-workers, which is widely used for the thermodynamic studies of chemical reactions.[55] A drawback of implicit solvation approaches is that the solvent molecules are not described quantum chemically, and therefore, strong and directional solvent-solute interactions are not accounted for, such as intermolecular hydrogen bonds and significant dipole-dipole interactions.

One alternative approach that aims to overcome these limitations is microsolvation. In this method, a limited number of explicitly represented solvent molecules is included in the computational model. The resulting molecular complex is then computed with an implicit solvation method.[56,57] On the one hand, a drawback of this method is related to the increased computational cost of performing quantum chemical calculations with a larger system. On the other, with this approach is possible to describe the solvent-solute interactions quantum chemically, which highly important when studying chemical systems that can establish strong interactions with the solvent. This is, for example, the case for dissociated ion pairs or species with multiple hydrogen bond donor and acceptor groups. Some possible effects of microsolvation approaches in computational results are schematically represented in Scheme TB-2. For instance, for a diol species, (Scheme TB-2-A), if the computational model incorporates the solute with an implicit solvent model, only intramolecular H-bonds can be established. However, if solvent molecules with H-bond acceptor groups (such as acetonitrile) are included in the computational model, intermolecular H-bonds between the diol and the solvent can also be formed. In general, solute-solvent interactions are weak and, therefore, present low significance if the solvent has low polarity or does not contain H-bond donor or acceptor groups. However, the microsolvation approach can become crucial for studying many dissociated ion systems. In this work, it was observed that explicit solvent molecules played an important role in the stabilization of carbocation intermediates (Scheme TB-2-B). Since carbocations are highly reactive and electronically unsaturated species, constructing a computational model containing only the carbocation and the anion often yields an unreactive neutral adduct species. Including explicit solvent molecules in the computational model allows a mimicry of the solvation effect of the dissociated species. As schematically represented in Scheme TB-2-B, an interaction of a solvent molecule with a counter-anion stabilizes the latter, and the dissociated ion system can be obtained through geometry optimization.

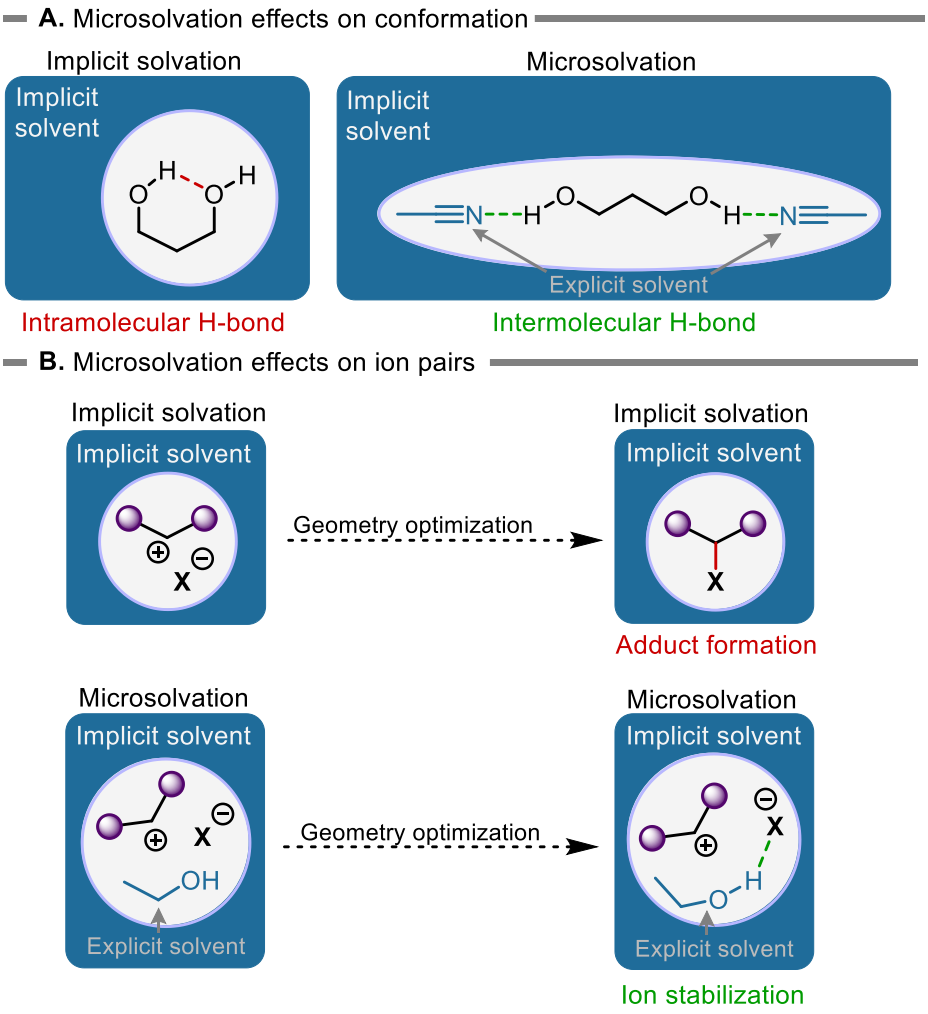

Scheme TB-2 – Schematic representation of the influence of microsolvation approaches: A) On the stability of conformations; B) On the stability of dissociated ion pairs, which can form neutral adducts without the inclusion of an explicit solvent molecule in the model.

2.4. Transition state theory

Transition state theory (TST) was developed by Eyring, Evans and Polanyi in 1935 to describe reaction rates of chemical reactions.[58] This theory considers the conversion of a reactant into a product by moving along the potential energy surface (PES). This surface represents the energy of a chemical system as a function of the atomic coordinates of the nuclei.[27] A representation of a one-dimensional PES is shown in Scheme TB-3. According to the TST, reagents, intermediates and products correspond to minima on the PES, and a chemical reaction can be described as nuclei moving from one minimum to another along the path of least energy. The transition state (TS) is the nuclear configuration that separates the reactant and product regions on the PES. It is a first-order saddle point, characterized as being a maximum along the reaction coordinate and a minimum with respect to all other coordinates.

The difference in Gibbs free energy between the transition state and the reactant ($\Delta G^{\ddagger}$) is the activation barrier of the reaction. This is the minimum energy required for the reactant to overcome the TS and be converted into the product. The Gibbs free energy difference between the product and the reactant (ΔG) provides information on the relative thermodynamic stability of these species. If the product is thermodynamically more stable than the reagent, ΔG is negative, and the reaction is spontaneous (exergonic). If, however, contrary to the example shown in Scheme TB-3, the product is less stable than the reactant, ΔG is positive, and the reaction is non-spontaneous (endergonic).

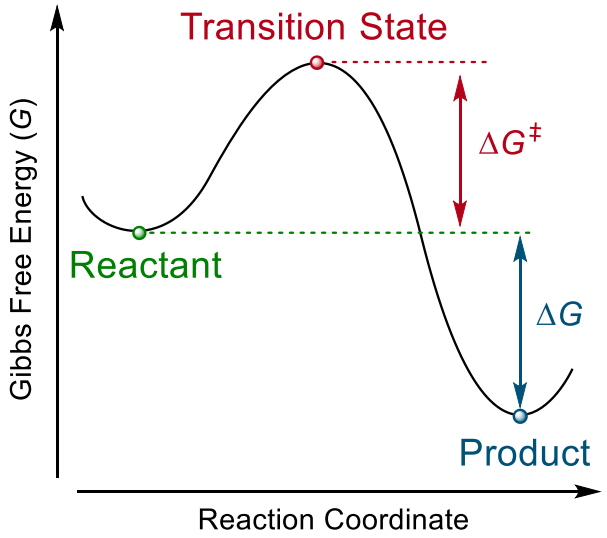

Scheme TB-3 – Representation of a potential energy curve that connects a reactant (green) to a product (blue) through a transition state structure (red).

As mentioned above, transition states are first-order saddle points and correspond to a maximum along the reaction coordinate. To locate such structures, extensive potential energy scans are performed on reactant and plausible intermediate structures. In a potential energy scan, a reaction coordinate is selected and perturbed step-by-step. For instance, when studying a bond dissociation, the distance between the connected atoms is elongated with a defined increment, typically 0.1 Å, for a defined number of steps. At each step, the incremented bond length is fixed and the geometry of the remaining molecular system is optimized. As a result of the imposed geometric displacement, the system deviates from the initial energy minimum structure and the energy of the system increases at each step. Reaching a scan step where the energy is lower than the previous step is typically an indication that the transition

state structure has been crossed, and the structure of the potential energy scan presenting the highest energy can be used as a starting point for a geometry optimization of a transition state.

The rate constant of a reaction (k_{rate}) indicates how fast a reaction occurs at a given temperature and is an important property to be considered in reaction kinetics studies. It can be determined experimentally by performing the same reaction multiple times at different temperatures and measuring how fast the reagents convert into products. It can also be determined computationally following the TST through the Eyring-Polanyi equation:

$$k_{rate} = \frac{k_B T}{h} e^{\frac{-\Delta G^{\ddagger}}{RT}}, \quad (3)$$

where k_B is the Boltzmann constant, T is the temperature, h is the Planck constant, R is the ideal gas constant, and $\Delta G^{\ddagger}$ is the activation Gibbs free energy, depicted in the energy profile of Scheme TB-3. The TST assumes that all reactant molecules passing through the TS will go on to form the product, and no re-crossings occur.[27] Therefore, the rate constant k_{rate} calculated from Equation 3 will be an upper limit to the true rate constant of the chemical reaction. Despite this approximation, the Eyring-Polanyi equation (Equation 3) is extremely useful for evaluating an energy profile. Given a temperature that matches experimental conditions, the validity of a computed mechanistic step can be verified by predicting the expected rate constant for such a reaction step using the obtained activation barrier. When studying reaction mechanisms, it is essential to consider whether the computed steps have feasible activation barriers. As a rule of thumb, barriers significantly higher than 25 kcal/mol are not compatible with a reaction that occurs at room temperature since the corresponding reaction rate is very low, in the order of 10^{-6} s^{-1}. Computed activation barriers that range from 10-15 kcal/mol are moderately low and correspond to fast reactions at room temperature. Below this interval, the barriers can be considered very low and correspond to very fast reaction steps, which present a very high rate constant, in the order of 10^{5} s^{-1}.

When analyzing an energy profile with multiple steps, it is important to determine consistently the overall activation barrier of the entire process. This barrier can then be used with the Eyring-Polanyi equation to evaluate the apparent rate of the reaction and validate the plausibility of the computed

mechanism. A good approach to identify the overall activation barrier is through the energetic span model.[59] This model was devised to compute the energetic efficiency of catalytic cycles, but it can be applied to energy profiles containing multiple steps, as schematically represented in Scheme TB-4. This example shows a reaction step sequence starting from an intermediate **A**, which is converted into **B**, which in turn is converted into **C,** which finally yields **D**. By comparing the free energy of the TSs with the preceding intermediate, it is possible to obtain $\Delta G^{\ddagger}_1$ (difference in energy between $\mathbf{TS_{AB}}$ and **A**), $\Delta G^{\ddagger}_2$ (difference in energy between $\mathbf{TS_{BC}}$ and **B**) and $\Delta G^{\ddagger}_3$ (difference in energy between $\mathbf{TS_{CD}}$ and **C**). The step that presents the highest activation barrier is the conversion of **B** into **C**. However, the apparent activation energy of the overall reaction is determined by the highest energy difference between a transition state and an intermediate that precedes it in the energy profile. In this example, the apparent activation energy of the profile is, therefore, $\Delta G^{\ddagger}_4$, obtained as the energy difference between **B** and $\mathbf{TS_{CD}}$. Although the energy profile does not directly connect these two states, the TST assumes that the system's energy is conserved. Thus, **B** must overcome a barrier of $\Delta G^{\ddagger}_4$ to reach **D** along the lowest energy path. The apparent activation energy of the profile, $\Delta G^{\ddagger}_4$, can be used in the Eyring-Polanyi equation in place of $\Delta G^{\ddagger}$ (Equation 5) to estimate the apparent rate of the overall reaction.

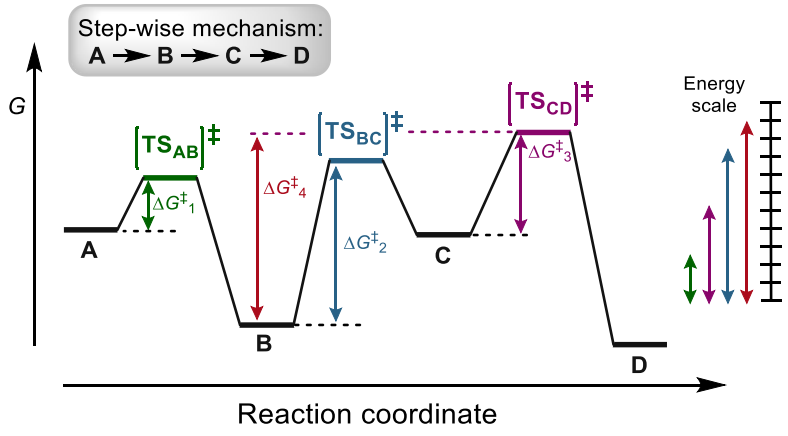

Scheme TB-4 – Schematic representation of an arbitrary energy profile of a transformation with three steps. Activation barriers can be obtained for each individual step, but the highest barrier can be computed between an intermediate and a transition state that are not directly connected.

2.5. Approach for conformational search

Rotation of single bonds and other types of internal molecular flexibility can cause the alternation between different structural isomers without breaking and reforming chemical bonds. Localization of

these isomers is crucial in computational studies, especially in mechanistic investigations since they can present significant differences in energy. In constructing an energy profile, it is important to consider that the reactants, transition states, intermediates and products present different conformations, each with its own free energy. Generally, the rotation of single bonds presents a very low barrier, and therefore, the interconversion between different conformers is faster than a chemical reaction. Different conformations of the same reagent often lead to different conformations of a transition state that yields configurationally the same product. A schematic representation of an energy profile containing different conformations of the reagent, transition state and product, as well as the overall energy profile representation, is shown in Scheme TB-5.

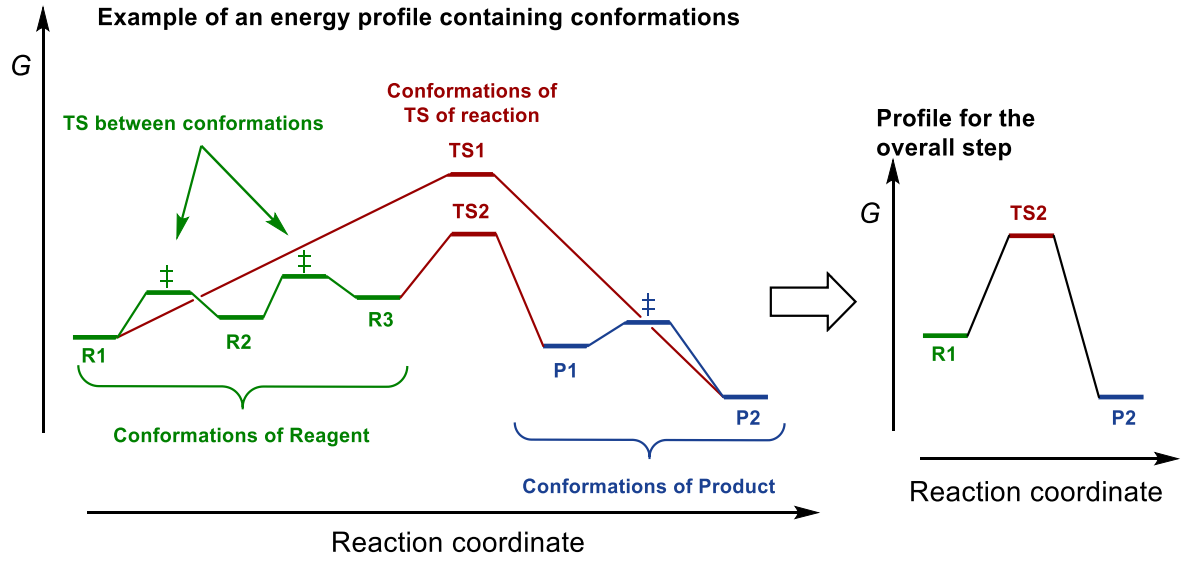

Scheme TB-5 – Representation of an arbitrary energy profile, extended to include the energy of different conformations of the reactant species (green), transition state (red) and product (blue).

In the profile on the left, the reagent is shown in green and presents three conformations (**R1**, **R2** and **R3**) that can convert into each other, very often with negligible activation barriers. The direct pathway from the most stable reagent conformer (**R1**) into the most stable conformation of the product (**P2**) passes through a less stable conformer of the transition state (**TS1**). However, in this presented example, the energy profile with the lowest activation barrier can be obtained through the sequential transformation of **R1**→**R2**→**R3**→**TS2**→**P1**→**P2**. This sequence starts from the reactant conformation **R1**, which undergoes a conformational change into **R2**, then to **R3**. At this point, **R3** can reach the transition state **TS2**, leading to the product conformation **P1**. Finally, **P1** can undergo conformational

change into **P2**. This path connects **R1** and **P2** indirectly through the most stable transition state conformation, **TS2**. In general, the activation barriers between conformers are much lower than the barrier for the studied chemical transformation. Thus, the Gibbs free energy profiles can be constructed accurately using the most stable conformer of each species, whether it is a minimum or transition state.[60] With this approach, the left energy profile of Scheme TB-5 can be converted into the profile in the right, which describes the conversion of the most stable conformation of the reagent (**R1**) into the most stable conformation of the product (**P2**) following the path of lowest energy. The resulting activation barrier is then obtained between **R1** and **TS2**. The purpose of Scheme TB-5 is to highlight the importance of identifying the most stable conformations for all minima and transition states.

An efficient approach to conformational exploration involves initially using a low-accuracy, low-cost computational method to screen numerous conformers and quickly exclude the most unstable structures. The most stable conformers can then be evaluated at a higher level of theory (e.g., DFT) to determine the most thermodynamically stable structures. In this work, the initial conformer search was conducted using the Conformer-Rotamer Ensemble Sampling Tool (CREST) software package with the completely automated partially polarizable generic force-field for geometries, frequencies, and non-covalent interactions (GFN-FF) or semiempirical tight-binding quantum chemical calculations (xTB).[61–63] This method often yields a large number of conformations that can be filtered to reduce the computational cost. Specifically for transition state structures, the conformational search is performed via a constrained optimization approach, i.e., freezing the breaking/forming bonds. This allows the reactive center of the system to be kept intact while exploring the flexibility of the rest of the system. The structures obtained from this constrained conformational search still correspond to a transition state of the studied transformation and can present favorable non-covalent interactions between side groups, which can potentially be overlooked in the initial search for the transition state structure. A schematical representation of the procedure applied in this work is shown in Scheme TB-6.

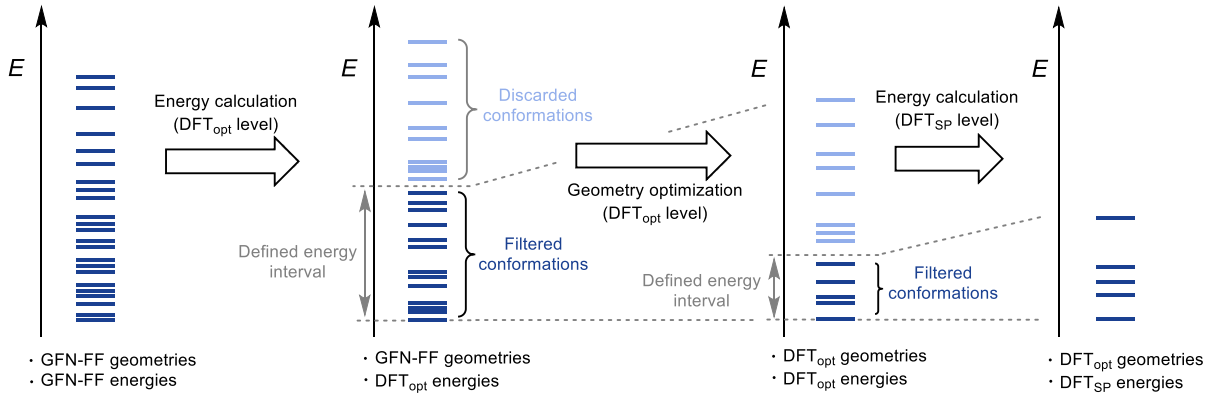

Scheme TB-6 – Representation of the procedure used for the conformation search and filtering of the obtained structures. An initial conformer search with force field methods (GFN-FF) can provide many conformations of a chemical system. Further refinement of the geometries and energies can be applied to obtain the most stable conformations. DFT_{opt} and DFT_{SP} refer to the level of theory for the geometry optimization and the final single point calculation, respectively.

The energy of the most stable conformations of each species, both minima and transition states, is computed at the DFT level of theory chosen for the geometry optimization (DFT_{opt}). This way, the structures obtained with the force field methods can be ranked by energy at the DFT level. Taking the most stable conformer as a reference, an energy interval can be defined, and all the conformations that present higher relative energy than the set interval can be excluded. The most stable structures are subjected to geometry optimization and frequency calculation (DFT_{opt}). After geometry optimization at the DFT level, the structures can then be sorted again by energy, and a final single-point calculation at a higher level of theory (DFT_{SP}) is performed for the most stable conformers. After a final sorting of the energies, the most thermodynamically stable conformer can be determined at the $DFT_{SP}//DFT_{opt}$ level of theory. In the work developed in this thesis, a 14 kcal/mol interval was considered in the filtering of conformations to be subjected to geometry optimization and an energy window of 7 kcal/mol was chosen before the energy calculations in the final step.

2.6. Computational Details

The conformational space of all molecules has been initially searched using the GFN-FF force-field approach or semiempirical xTB calculations as implemented in the software package CREST.[64] The quantum chemical calculations were performed using the Gaussian 16 rev C.01 software package.[65] The transition states were optimized with the synchronous transit-guided quasi-Newton method (STQN) developed by Schlegel and co-workers.[66] Frequency calculations were performed at the same level of

theory as applied for geometry optimization to confirm the nature of the stationary points, yielding one imaginary frequency for the transition states and none for the minima. Each transition state was further confirmed by following its vibrational mode downhill on both sides and obtaining the minima presented on the energy profile. The thermal corrections to the Gibbs free energies were combined with the single point energies calculated at the higher level of theory to yield Gibbs free energies ("G_{298}") at 298.15 K. All energies are reported in kcal · mol^{-1}. The energy profiles were constructed using each intermediate and transition state's most stable conformation (the global minimum). Free energies in solution have been corrected to a reference state of 1 mol · l^{-1} at 298.15 K through the addition of RTln(24.46) = +7.925 kJ · mol^{-1} to the gas phase (1 atm) free energies.

For the work of chapters I and II, the PBE0 functional,[41] with def2-SVP basis set,[67] including empirical correction for dispersion obtained through Grimme's DFT-D3 method with Becke and Johnson (BJ) short distance damping was used for geometries and frequencies.[48,68] Single point energy calculations were performed on the optimized geometries at the PBE0-D3(BJ)/def2-TZVP level, i.e., using the same DFT functional as for the structural and vibrational analysis but a triple-zeta valence quality basis set. Chapter III involved radical mechanisms, and, therefore, the range-corrected functional developed by Head-Gordon and co-workers, ωB97X-D, was applied.[43,69] Implicit solvent effects were considered using the SMD solvation model developed by Truhlar and co-workers, considering dichloromethane or acetonitrile as the solvent.[54,55,70]

3. Chapter I: C-H activation through hydride shifts

3.1. Rearrangements

Rearrangement reactions are a broad class of organic reactions where a substituent group moves from one atom to another within the same chemical compound. These intramolecular processes yield a structural isomer of the original compound, as shown in Scheme HS-1-A, where a migration of a functional group R to a neighboring carbon results in the conversion of **S1-1** into **S1-2**. The formation of a more stable structure is the main driving force for rearrangement reactions to occur. The first discovered case of such reactions is the pinacol rearrangement, which was reported in 1859 by Fitting (Scheme HS-1-B).[71] In this system, the reaction of the 1,2-diol **S1-3** with sulfuric acid yields the ketone **S1-6**. The mechanism of this transformation is assumed to occur through an initial abstraction of water, forming a carbocation intermediate **S1-4**. From this species, a migration of a methyl group (highlighted in green) can occur to the adjacent carbon atom, yielding the intermediate **S1-5**. Finally, a proton abstraction generates product **S1-6**. In this transformation, **S1-4** and **S1-5** are structural isomers, and their direct interconversion is a rearrangement reaction.

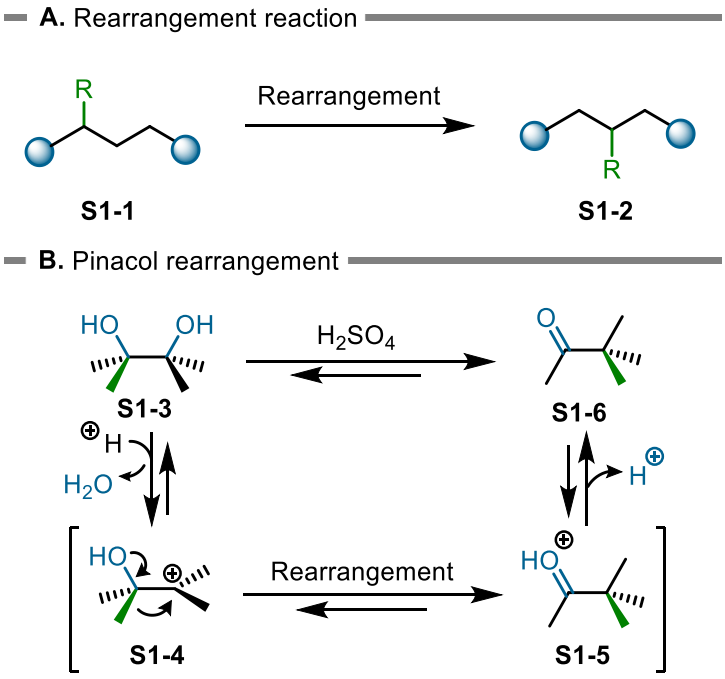

Scheme HS-1 – A) Schematic representation of a rearrangement reaction involving the migration of a substituent group R along an alkyl chain; B) Reported mechanism proposal for the reaction of pinacol with sulfuric acid, involving a rearrangement step.

Many other rearrangements have been studied (i.e., Claisen, Hofmann) since the discovery of the pinacol rearrangement and this class of transformations has found a widespread use in chemical synthesis.[72]

3.2. Hydride shifts

A rearrangement reaction involving the migration of a hydrogen atom within a carbocation is called a hydride shift. These transformations are a common feature of carbocation chemistry and are particularly important in the biological pathways by which steroids and related substances are synthesized.[73,74] An example can be found in nature in the biosynthesis of cholesterol, highlighted in Scheme HS-2. The conversion of the carbocation intermediate **S2-1** into **S2-2** occurs with the migration of a hydrogen atom to the adjacent carbon, C_b. This transformation also results in the migration of the cationic charge from C_b to C_a.

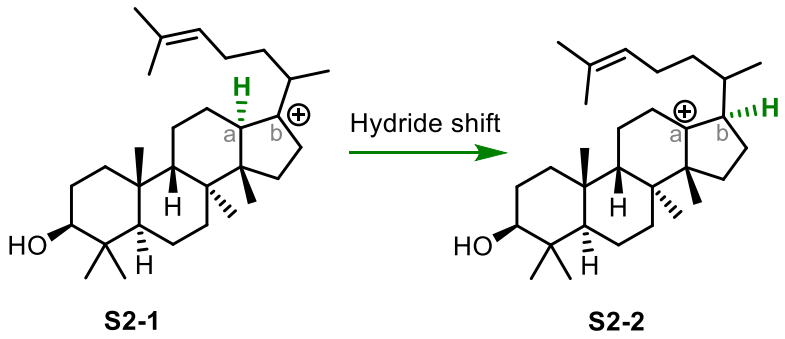

Scheme HS-2 – Mechanistic representation of the hydride shift step in the cholesterol biosynthesis.

In most cases, the main driving force for the occurrence of hydride shifts is of thermodynamic nature, with the formation of a more stable carbocation. Generally, more substituted carbocations are more stable (Scheme HS-3-A). Thus, primary carbocations are less stable than secondary, which in turn are less stable than tertiary carbocations. In addition to the degree of substitution, other factors affect the stability of carbocations. These include resonance effects, which increase the overall stability of the carbocation, and induction effects of the substituents. Electron-donating groups are able to increase the electronegativity of the carbon at which the cationic charge is located, which in turn increases the stability of the carbocation. In systems containing alkyl carbocations, the occurrence of hydride shifts will tend towards the formation of tertiary carbocations as these are more stable intermediates. The migration of charge along an alkyl chain can be envisioned through four possible transformation types

(Scheme HS-3-B). In a [1,2]-hydride shift, the hydrogen atom shifts from the carbon adjacent to the carbocation through a 3-membered ring transition state. In systems containing longer alkyl chains, other types of hydride shifts could occur through transition state structures presenting 4-, 5-, and 6-membered rings. These correspond to [1,3]-, [1,4]- and [1,5]-hydride shifts, respectively, where a concerted step would be responsible for the relocation of the cationic charge to a remote carbon on the alkyl chain and can therefore be considered long-range shifts. Carbocations are highly reactive species where charge relocation processes occur very quickly in reaction conditions. Thus, experimental evidence of a charge relocation process can only be obtained through the chemical characterization of reaction products and their comparison to the reactants. However, if a charge relocation occurs to a remote carbon, it is not possible to set mechanistic insights on which combination of hydride shift types has occurred. To the best of our knowledge, there is no reported experimental study about the kinetic competition between hydride shift types presented in Scheme HS-3-B. Therefore, the resort to computational chemistry is required to shed light on the most kinetically favored types of hydride shifts in alkyl carbocationic systems.

It has been shown that short-range migrations of the hydrogen atom, corresponding to [1,2]-hydride shifts, are the most observed and reported types of hydride shifts.[74] [1,5]-hydride shifts are also kinetically facilitated due to the formation of 6-membered ring transition state structures.[75] The same principle could be considered for [1,4]-hydride shifts, which involve a 5-membered ring transition state and, therefore, should also be kinetically allowed. While most reported examples of charge relocation events correspond to the occurrence of [1,2]- and [1,5]-hydride shifts, we believe that a comparative study of the kinetic competition between different types of hydride shifts can provide a significant benefit for planning metal-free C-H activation reactions. In summary, the mechanistic study of hydride shift reactions involving charge relocation can pinpoint which carbocation intermediates are formed in the reaction media. As benefit, these computational studies can help guiding the overall reaction process towards better selectivities. Framed in these ideas, the main goal of this work is to investigate and identify the possibility of favoring long-range ([1,3]- ,[1,4]- and [1,5]-) hydride shifts steps in alkyl carbocationic systems for the synthesis of new compounds *via* metal-free C-H activation processes.

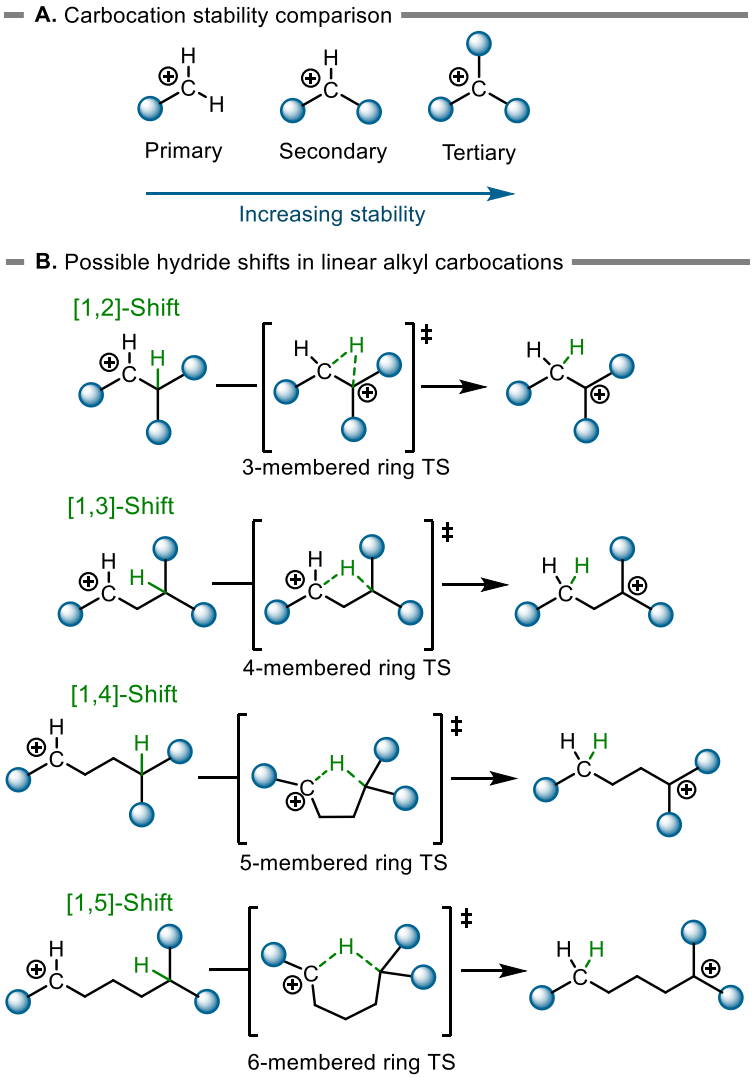

Scheme HS-3 – A) Representation of the increasing stability of carbocations with a higher degree of substitution; B) Mechanistic representation of possible hydride shift steps occurring in linear alkyl carbocations.

3.3. Investigation of [1,3]-hydride shifts

In a recent publication of the Maulide group (Scheme HS-4-A), it was observed that a leaving group abstraction from an oxazolidinone derivative, **S4-1**, results in the formation of a secondary carbocation in the α-position to a carbonyl group (intermediate **S4-2**).[76,77] The proximity between the positively charged carbon and the carbonyl group of the oxazolidinone moiety in intermediate **S4-2** gives rise to an intramolecular stabilization of the carbocation. This stabilization step forms of the oxocarbenium intermediate **S4-3**, which can be further functionalized in reaction media. Oxocarbeniums are stable carbocation intermediates that contain a sp^2-hybridized carbon connected to an oxygen substituent,

allowing the positive charge to be stabilized by resonance between the carbon and the oxygen atoms. In this system, the carbon in β- position to the carbonyl is part of a phenyl ring and, therefore, not bound to any hydrogen atom. As a result, hydride shift steps are not possible, and the cationic charge is "trapped" in the α-position to the carbonyl in **S4-2** until the 5-membered oxocarbenium ring is formed.

Inspired by this observation, we conceptualized a system in which starting from a carbocation in α-position to a carbonyl group (intermediate **S4-2')**, a [1,3]-hydride shift would lead to the formation of a carbocation in the γ-position (intermediate **S4-4)**, as shown in Scheme HS-4. Hypothetically, this transformation would allow a subsequent intramolecular stabilization towards a 5-membered oxocarbenium intermediate **S4-5**, which could finally be converted into γ-hydroxyketones products (**S4-6**) that have added value for their application in fine chemistry and pharmaceutical industry.[78]

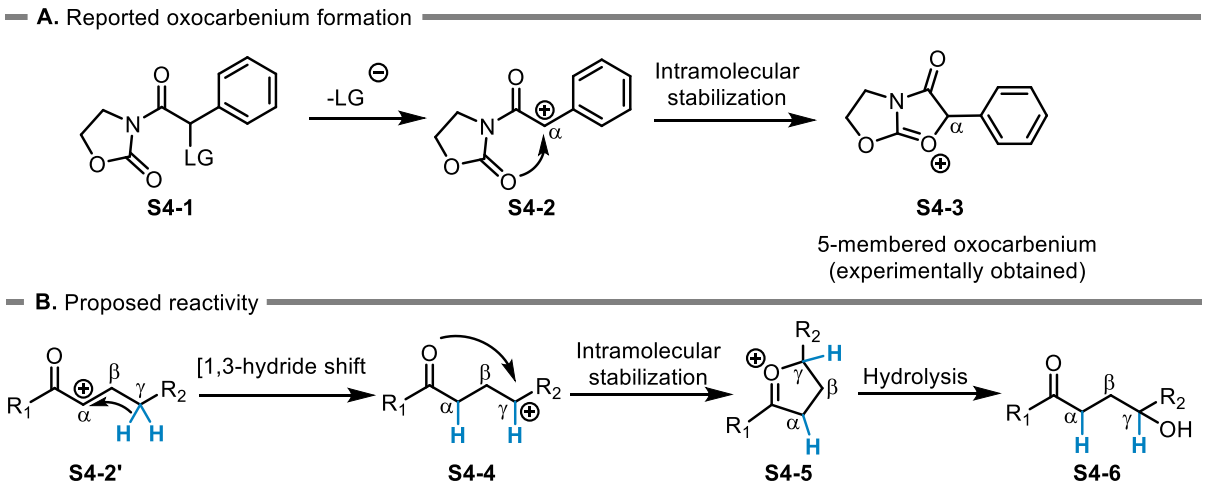

Scheme HS-4 – A) Reported reaction involving the formation of a carbocation species that becomes highly stabilized through the formation of an oxocarbenium intermediate; B) Mechanistic proposal for a [1,3]-hydride shift step which would lead to the formation of an oxocarbenium intermediate with analogous structure.

The proposed [1,3]-hydride shift was studied computationally at the PBE0-D3(BJ),SMD(DCM)/def2-TZVP//PBE0-D3(BJ),SMD(DCM)/def2-SVP level of theory. The chosen model substrate **S5-1** is shown in Scheme HS-5. It includes two methyl groups in the β-position to the carbonyl with the objective of forcing the carbons in the α- and γ-positions to be closer, adding the Thorpe-Ingold effect to the chain. The generation of these type of cationic intermediates in experimental conditions can involve the abstraction of a leaving group, as shown in Scheme HS-4-A. However, it is known that the abstraction of a leaving group (i.e. bromide) is only possible from a

substrate containing a substituent in the α-position to the carbonyl.[79] Thus, a methyl group was introduced in the α-position to the carbonyl to assist in the stabilization of the α-carbocation **S5-1**.

Finally, with a quaternary carbon in the β-position, the occurrence of a [1,2]-hydride shift step is not possible. It would then be expected that a [1,3]-hydride shift yields a primary carbocation intermediate **S5-2** that can quickly evolve to the oxocarbenium intermediate **S5-3**.

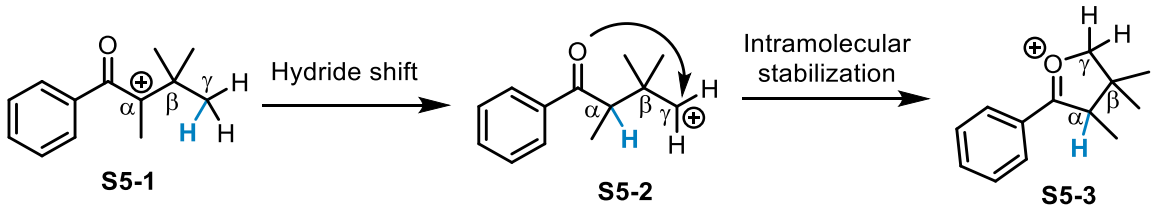

Scheme HS-5 – Envisioned mechanism for the designed computational model.

Throughout several attempts to obtain an energy profile for the envisioned [1,3]-hydride shift, only one pathway was found leading to a 5-membered oxocarbenium intermediate (Figure HS-1). This computed step (**F1-A→F1-B**) presents a small activation barrier ($\Delta G^{\ddagger}$(**F1-A→F1-B**) = 14.6 kcal/mol), which would allow the reaction to occur at low temperatures. Surprisingly, this hydride shift is concerted with a [1,2]-sigmatropic rearrangement that causes an inversion in the order of the carbons in the alkyl chain. During this step, the Cα-Cβ bond is cleaved, and a new Cα-Cγ bond is formed. As a result of this transformation, the cationic charge is relocated to a tertiary carbocation, as represented in the transient structure **F1-B'**. However, this structure is not accessible as an energy minimum and, throughout the geometry optimization, evolves into a highly stable oxocarbenium intermediate **F1-B**. The step **F1-A→F1-B** is indeed intriguing because since the carbon in the β-position to the carbonyl in **F1-A** has methyl substituents, the chain order inversion ultimately results in the extension of the longest linear alkyl chain (from 3 carbons in **F1-A** to 4 carbons in **F1-B**). To address the kinetic and thermodynamic viability of this step, a competitive [1,2]-methyl shift was computed, step **F1-A→F1-C**, revealing a lower activation barrier ($\Delta G^{\ddagger}$(**F1-A→ F1-C**) = 8.1 kcal/mol). The carbocation intermediate formed with this step, **F1-C**, is 2.3 kcal/mol less stable than **F1-A**, strongly indicating that this methyl shift would be a highly reversible process, allowing the proposed [1-3]-hydride shift to occur, forming **F1-B** irreversibly.

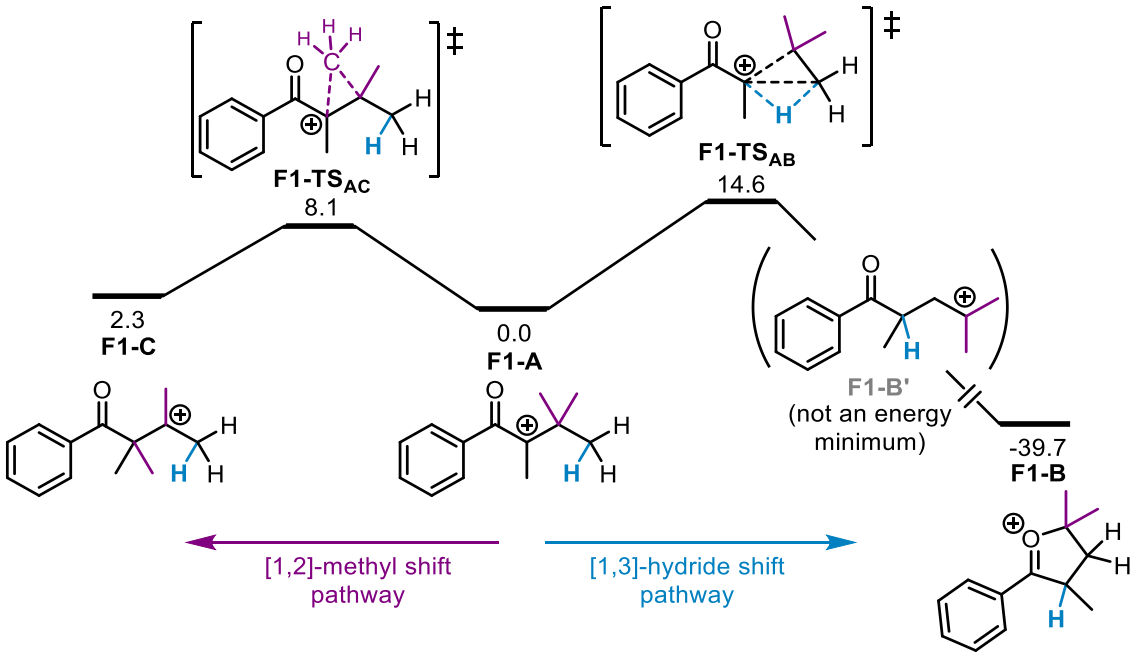

*Figure HS-1 – Computed Gibbs free energy profile containing two possible competing pathways for a carbocation rearrangement step. The reactant complex **F1-A** serves as a reference (0.0 kcal/mol), and the explicitly included solvent molecule (DCM) was omitted from the scheme for clarity.*

The optimized structures of **F1-A**, **F1-TS$_{AB}$** and **F1-B** are shown in Figure HS-2. In the cationic intermediate **F1-A**, an interaction between the oxygen of the carbonyl and Cα is established. **F1-A** can then be interpreted as a 3-membered oxocarbenium species. It is worth mentioning that the structure **F1-C** (Figure HS-1) is a tertiary carbocation, and yet it is 2.3 kcal/mol less stable than **F1-A** (which is also a tertiary carbocation). Although the carbonyl group is typically an electron-withdrawing group, the interaction between the oxygen and the carbocation provides a significant increase in the stabilization of the cationic charge. Visual inspection of the 3D structures of intermediates **F1-A** and **F1-B** provides structural details of the degree of stabilization of the oxocarbenium (Figure HS-2). In **F1-A**, the O-Cα interaction presents a length of 1.63 Å, forming a strained 3-membered ring. In addition to this constrained stabilization, the C$_1$-Cα bond presents a length of 1.43 Å, which is much closer to the typical length of C-C double bonds (1.32 Å).[80] Contrarily, in the highly stable 5-membered oxocarbenium intermediate **F1-C**, the O-Cβ interaction presents a length of 1.50 Å (0.13 Å shorter than the O-Cα interaction in **F1-A**) and a Cβ-Cγ bond length of 1.53 Å, which is in the range of single C-C bonds (1.54 Å in alkanes). In the transition state structure **F1-TS$_{AB}$**, the four nuclei participating in the transformation (H, Cα, Cβ and Cγ) are in the same plane. The Cγ-H bond is being cleaved at a length of 1.72 Å, which

is significantly longer than the distance at which the Cα-H bond is being formed (1.13 Å), which suggests that this structure corresponds to a late transition state. The length of Cα-Cβ (bond being cleaved) is very similar to the Cα-Cγ bond length (bond being formed). Curiously, with a Cβ-Cγ bond length of 1.41 Å, this transition state contains the structure of a protonated cyclopropane, which is a carbocationic species that will be further discussed in the next chapter of this dissertation.

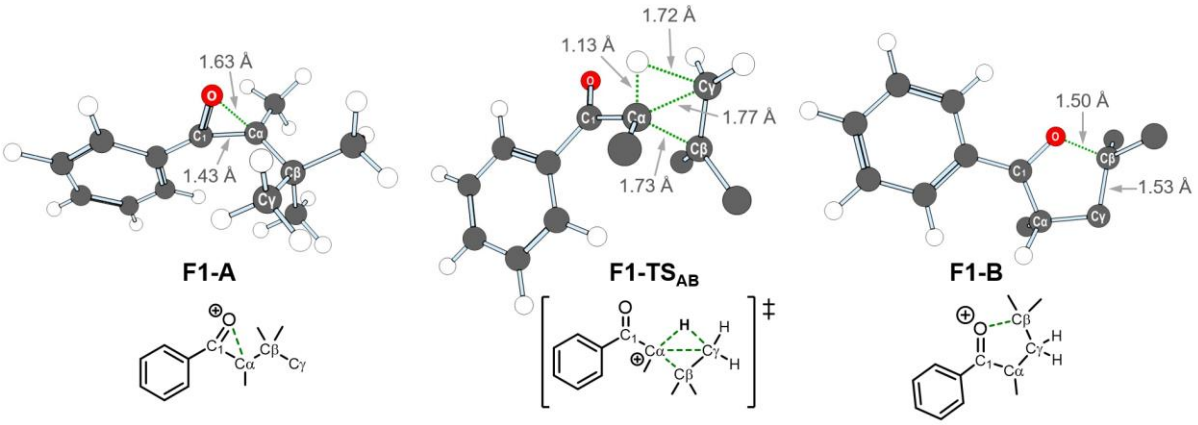

Figure HS-2 – 3D representation of computed structures with the length of selected bonds.

As shown above in Scheme HS-5, with the formation of a 5-membered oxocarbenium intermediate, a hydrolysis step would lead to a hydroxyketone product. Following the hydride shift, which was hypothesized prior to computational studies, the generation of the cationic species **S6-1** (Scheme HS-6) would generate intermediate **S6-2** that would be converted into the β-substituted γ-hydroxyketone **S6-3**. However, the computationally obtained energy profile predicts the occurrence of a chain order inversion leading to **S6-2'**, which would instead yield the γ-substituted γ-hydroxyketone product **S6-3'** after hydrolysis.

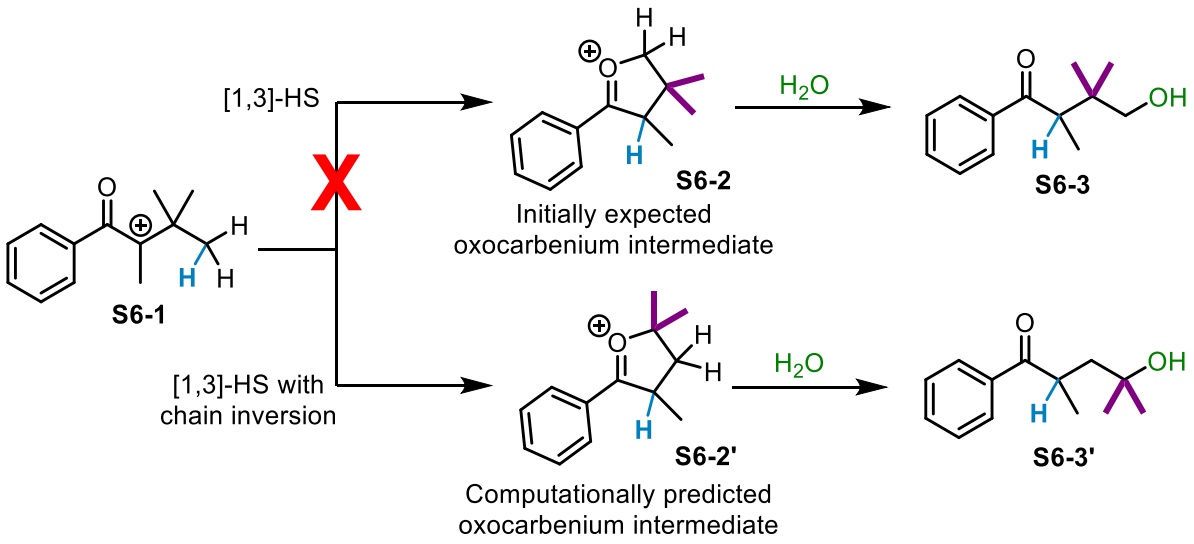

Scheme HS-6 – Mechanistic proposal following the obtained [1,3]-hydride shift transition state, together with the initially devised mechanism for the 5-membered oxocarbenium intermediate.

This transformation was studied further by replacing the methyl group in the α-position with a tert-butyl group and the *para*-position of the aromatic ring with electron-donating (methyl and methoxy) and electron-withdrawing groups (fluoro and trifluoromethyl). The energy profiles for the combination of these functional groups were computed with the aim of understanding "if" and "how" the thermodynamic and kinetic properties of this step are affected by the bulkiness of the substituent at the α-position and by the electronics of the aromatic group. The obtained Gibbs activation free energies ($\Delta G^{\ddagger}$, in blue) and Gibbs free energies of formation (ΔG, in purple) of the 5-membered oxocarbenium intermediate are displayed in Figure HS-3.

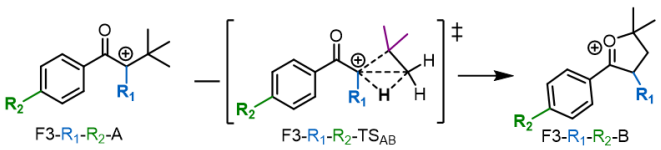

	$\Delta G^{\ddagger}$ (kcal/mol)					ΔG (kcal/mol)				
	R_2					R_2				
	H	CH_3	F	CF_3	OCH_3	H	CH_3	F	CF_3	OCH_3
Me	17	18	17	15	21	-34	-33	-34	-35	-32
tBu	22	24	23	20	26	-37	-36	-37	-37	-35

Figure HS-3 – Effect of different substituent groups in the computed activation energies and thermodynamic stability of product formation for the studied [1,3]-hydride shift.

At first glance, it is clear that none of the studied substituent modifications has a significant impact on the thermodynamics favorability of the reaction, which is highly exergonic in all cases ($\Delta G \leq$ -32 kcal/mol). However, these modifications do affect the kinetic feasibility of the reaction. The introduction of a *t*Bu group imposes additional symmetry elements in the substrates. As a result, the [1,3]-hydride shift could occur from both homotopic *t*Bu fragments. Additionally, with the *t*Bu group, both the carbons in the β-position to the carbonyl are quaternary and would not allow any [1,2]-hydride shift event from the initial substrate (**F3-tBu-R_2-A**). Despite these factors in favor of the proposed [1,3]-hydride shift, the increase in bulkiness conferred by the *t*Bu group poses a dominant kinetic impediment for the reaction to occur. As discussed above, the studied step involves a complex rearrangement ([1,3]-hydride shift concerted with a [1,2]-sigmatropic rearrangement), which requires a significant distortion of the substrate structure until the exquisite transition state structure is achieved. Taking this into account, a bulky group like *t*Bu may reduce the flexibility of the system and increase the activation barrier of the transformation.

Interestingly, electron-withdrawing groups lower the activation barrier of the reaction, while electron-donating groups increase it. Considering the [1,2]-sigmatropic rearrangement event that occurs during this transformation, the same carbon atom is involved in one C-C bond cleavage and one C-C bond formation. Therefore, it is sensible to expect that any electron-withdrawing or donating behaviour of these groups would, on the one hand, favour the C-C bond cleavage, and on the other, disfavour the C-C bond formation of this concerted step. Therefore, the kinetic effect imposed by the studied groups can be understood by the stabilization/destabilization of the carbocation reactants (**F3-R_1-R_2-A** in Figure HS-3). As mentioned before, the interaction of the carbonyl with the carbocation forms a 3-membered oxocarbenium species, allowing the stabilization of the reactant. The more electron-withdrawing the aromatic group is, the weaker the oxocarbenium stabilization and, therefore, the less stable is the reactant. Since this interaction is not present in the transition state, the transition state energies should not be significantly affected by the aromatic group. This assumption leads us to believe that the kinetic feasibility of this reaction can be improved with the use of substrates that generate less stable carbocation reactants. It is important to be aware that less stable carbocationic species are more difficult to be

generated *in situ*, and more reactive, possibly leading to an increase in side reactions (such as methyl shifts). Therefore, the feasibility of this hypothesis needed to be tested experimentally.

At an initial stage, the reaction of 2-bromo-2-methyl-1-phenylbutan-1-one with silver hexafluoroantimonate was performed in dichloromethane at 25 °C. After 10 minutes, the reaction was quenched with an aqueous solution of sodium carbonate, and the mixture was separated with column chromatography, from which the identified products were characterized by ^{1}H NMR (Scheme HS-7). The reagent **S7-1** was chosen for its instant availability in the laboratory's inventory. However, it was still kept in mind that the lack of methyl substituents at the β-carbon to the carbonyl would allow undesired elimination pathways. The experimental work, conducted alongside the computational investigations, was performed collaboratively within the Maulide group. The experimental details, including full characterization of the obtained products, are reported elsewhere.[81]

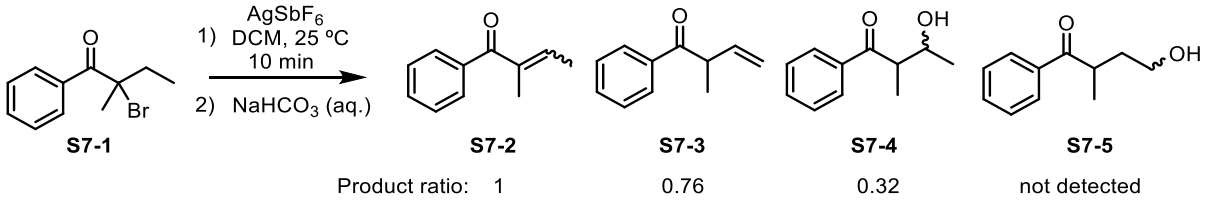

Scheme HS-7 – Experimental outcome of the reaction attempted to verify the proposed [1,3]-hydride shift mechanism.

From the three major identified products (**S7-2**, **S7-3**, **S7-4**), none of them was the expected product of the predicted [1,3]-hydride shift, **S7-5**. The expected mechanism for the formation of each product is described in Scheme HS-8. The silver antimonate reagent promotes a bromide abstraction from **S7-1**, forming the ionic pair [**S7-A**] [SbF_6]. Since SbF_6^- is a non-nucleophilic and non-basic counter anion, it is feasible to consider free cationic species in the reaction media without the formation of adducts with SbF_6^-. The cationic species **S7-A** is prone to β-elimination, promoted by residual moisture or during the basic quenching, forming the observed product **S7-2**. If **S7-A** undergoes a [1,2]-hydride shift, the positive charge migrates to the β-position, generating the 4-membered oxocarbenium intermediate **S7-B** through a CO---C^+ interaction. This intermediate is also prone to intramolecular elimination reactions. An α-elimination leads to the observed product **S7-2**, while a γ-elimination yields the terminal alkene **S7-3**. The higher experimental yield for the formation of **S7-2** is then explained by the convergent

elimination pathways, which can occur with (from **S7-A**) or without (from **S7-B**) a [1,2]-shift. Additionally, it was observed that intermediate **S7-B** can be hydroxylated to form a β-hydroxyketone, **S7-4**.

The expected product **S7-5**, which would be formed from **S7-A** through a [1,3]-hydride shift or a consecutive sequence of two [1,2]-hydride shifts followed by hydroxylation, was unfortunately not observed experimentally. This result raises concerns regarding the kinetic feasibility of the computationally proposed reaction (Scheme HS-6). Firstly, the formation of **S7-B** strongly suggests that a [1,3]-hydride shift is not kinetically competitive to a [1,2]-hydride shift. Furthermore, despite the very high thermodynamic stability of the proposed 5-membered oxocarbenium intermediate (**F1-B** in Figure HS-1), it was not detected in reaction media, and the charge migration was stopped at the β-carbon to the carbonyl, forming only a 4-membered oxocarbenium intermediate, **S7-B**. Lastly, the high reactivity of carbocationic species is highlighted by the accentuated formation of the elimination products **S7-2** and **S7-3**. This reactivity can potentially be controlled with the use of a more substituted reactant in which a β-elimination would not be possible directly after the first carbocation is generated.

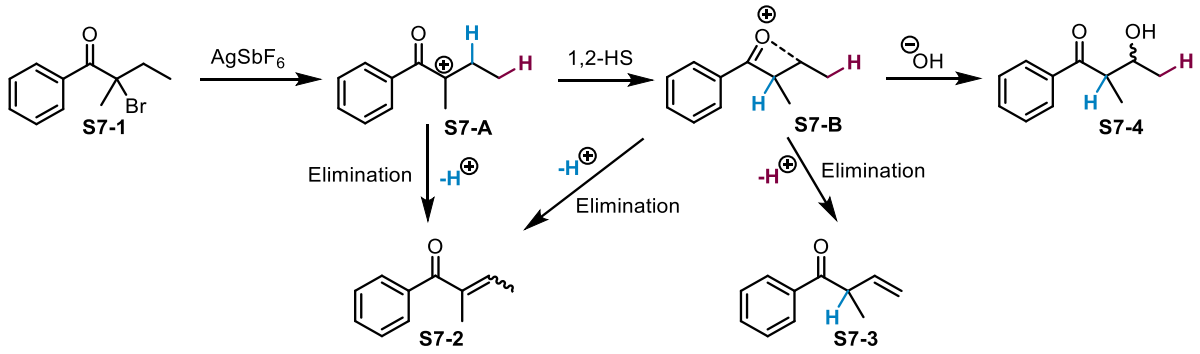

Scheme HS-8 – The proposed mechanism for the formation of the identified products from the reaction performed to verify the computed transformation.

The reaction of an α-bromo ketone with silver hexafluoroantimonate was attempted again, this time with 2-bromo-2,3,3-trimethyl-1-phenylbutan-1-one as substrate (Scheme HS-9). The silver-mediated bromide abstraction would generate the cationic intermediate **S9-1**. As discussed above (Scheme HS-6), the computed mechanism for a [1,3]-hydride shift would result in a chain order inversion that could be observed experimentally with this experiment. It was observed that the computationally predicted product **S9-4** was not formed. Instead, only the β-elimination product **S9-5** was detected. Nevertheless,

this result agrees with the computed energy profile (Figure HS-1). The computational results suggested, on the one hand, that from **S9-2** (**F1-A** in Figure HS-1), a methyl shift would be a highly reversible endergonic process, as confirmed experimentally. On the other hand, the 14.6 kcal/mol activation barrier for the predicted [1,3]-hydride shift is still significantly high, and this step is not competitive with intermolecular elimination processes in the reactional conditions.

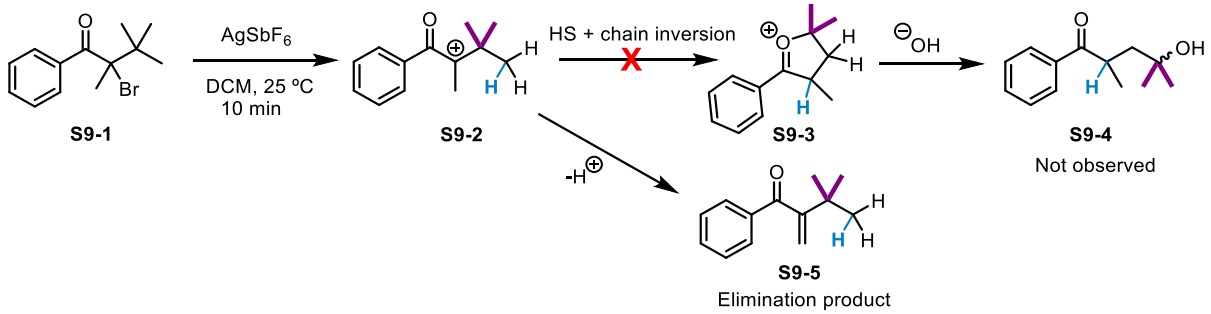

Scheme HS-9 – Attempted reaction with a substrate containing additional methyl groups to favour the computed [1,3]-hydride shift step. The expected hydroxylated product was not observed experimentally, and only elimination products were obtained instead.

One way to avoid the direct β-elimination step leading to products such as **S9-5** could consist in the use of 2-bromo-2-(tert-butyl)-3,3-dimethyl-1-phenylbutan-1-one as substrate. This substrate would differ from **S9-1** by having two *t*Bu groups in the α-position to the carbonyl. With both carbons in the β-position being tertiary, the intermolecular elimination would not be possible without the occurrence of a [1,2]-methyl shift or a [1,3]-hydride shift. However, due to challenging synthesis of this reagent, the system was not studied further. It is also important to consider that with the two bulky tert-butyl groups, the silver-mediated bromide abstraction step could be significantly hindered. Additionally, further imposition of functional group limitations in the reaction substrate would lead to an even narrower reaction scope, decreasing the utility of the studied reaction.

3.4. Investigation of [1,4]-hydride shifts

The obtained results reveal the difficulty to control cationic charge migration along linear alkyl chains. The fact that the desired 5-membered oxocarbenium intermediate is not formed under the reaction conditions, despite its very high thermodynamic stability, points to a kinetic control of these reactions. However, the chemical environment of the carbocation in experimental conditions is also extremely important. As can be observed in Scheme HS-7 and Scheme HS-9, the formation of alkene products

highlights the high acidity of the formed carbocation intermediates, which are prone to intermolecular proton transfers. Overall, the following set of considerations should be taken into account when studying these types of alkyl carbocations:

- The carbocation intermediates are always prone to intermolecular elimination.
- [1,2]-hydride shifts are highly feasible kinetically.
- [1,2]-methyl shifts might be reversible and are not expected to be competitive to [1,2]-hydride shifts.

As represented in Scheme HS-10, unsubstituted linear alkyl carbocations are highly prone to intermolecular elimination reactions since the hydrogens in α-position to the cationic charge are very acidic and can easily come into contact with basic species in the reaction media. While this effect could be mitigated with the introduction of ramifications on the alkyl chain, it would decrease the amount of hydrogen atoms that would be available to undergo hydride shift reactions. Additionally, a branched alkyl chain possesses a high degree of conformational flexibility, which could again favour intermolecular proton transfer rather than intramolecular hydride shifts. We, therefore, decided to investigate cyclic systems, which would allow the formation of alkyl carbocations with high conformational rigidity, forcing the carbon atoms that are not connected through a chemical bond to lie close to each other. Such conformational constraint could favour hydride shift steps, resulting in the migration of the positive charge along the cyclic alkyl chain. Additionally, the spatial arrangement of the cyclic systems provides steric protection to the acidic protons. If such an effect can reduce the possible contacts between the acidic protons and basic species in the reaction media, the intermolecular elimination events would be disfavored, contributing to the decrease in the formation of undesired alkene products.

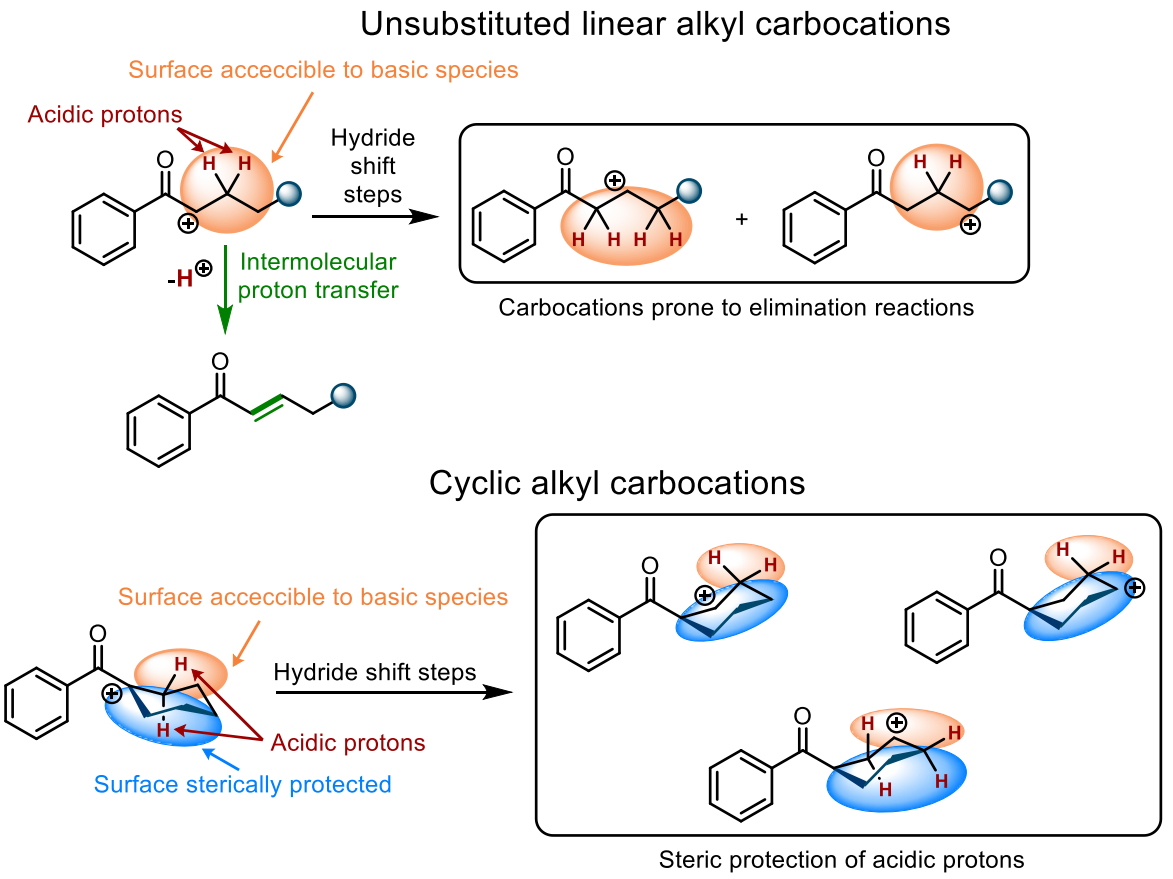

Scheme HS-10 – Representation of the skeletal effects of carbocations in the protection against elimination reactions leading to alkene products.

To verify this hypothesis, the reaction of (1-bromo-4-(tert-butyl)cyclohexyl)(phenyl)methanone, **S11-1**, with silver hexafluoro antimonate was performed in the same conditions as before (Scheme HS-11). The product of this reaction, which was isolated and characterized by ^{1}H NMR and single-crystal X-ray diffraction (SC-XRD) analysis, is an ion pair consisting of hexafluoro antimonate and the 6-membered oxocarbenium carbocation **S11-4**. The mechanistic sequence of this reaction starts with the formation of the carbocation intermediate **S11-2** through a silver-mediated bromide abstraction. The experimental observation of **S11-4** reveals the occurrence of a charge relocation from the α- to the δ-position to the carbonyl. This process requires an initial formation of the intermediate **S11-3**, followed by intramolecular stabilization, yielding the 6-membered oxocarbenium species **S11-4**. As expected, with this cyclic scaffold, the undesired elimination reactions were avoided, as no cycloalkene products were detected.

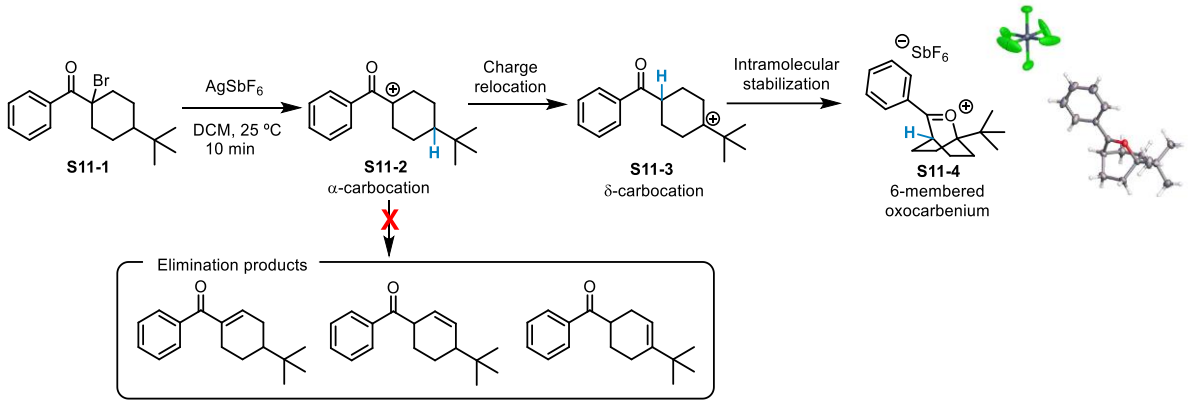

Scheme HS-11 – Mechanistic representation of an experimentally observed charge delocalization process leading to the formation of an oxocarbenium product characterized by SC-XRD.

It is worth noting that with the presence of a tert-butyl substituent in the δ-position to the carbonyl, both the intermediates **S11-2** and **S11-3** are tertiary carbocations (while carbocations at the β- and γ-positions would be secondary and thus, less stable). Taking this into consideration, we decided to computationally investigate the mechanism of the formation of a 6-membered oxocarbenium product. In this study, the tert-butyl group was replaced by a hydrogen atom for computational expediency. As a result of this simplified approach, the charge migration along the cyclic alkyl chain would lead to a secondary carbocation at the δ-position to the carbonyl, whereas in intermediate **S11-3**, the carbocation at the δ-position is tertiary due to the tert-butyl group. A total of three mechanistic energy pathways were obtained for the formation of the 6-membered oxocarbenium: the first consisting of a direct [1,4]-hydride shift (Figure HS-1-A), the second consisting of a [1,3]-hydride shift followed by a [1,2]-hydride shift (Figure HS-1-B), and finally the third which comprises a sequence of three consecutive [1,2]-hydride shifts (Figure HS-1-C). The inclusion of the counter anion, SbF_6^-, in the computational model would significantly increase the computational cost and conformational space, and so this study was performed considering the cation and an explicit solvent molecule (dichloromethane), given the non-acidic and non-coordinating nature of the SbF_6^- anion.

The overall formation of the 6-membered oxocarbenium intermediate **F4-D**, which is independent of which hydride shift pathway is considered (Figure HS-4-A, B or C), is highly exergonic (ΔG(**F4-A**→ **F4-D**) = -28.0 kcal/mol). The high thermodynamic stability of this species strongly suggests that this oxocarbenium could potentially be stable in the reaction media, in similarity to the tert-substituted

species **S11-4** (Scheme HS-11). In structure **F4-A**, the carbocation in the α-position presents a slight stabilization by the interaction with the oxygen from the carbonyl, resembling a 3-membered oxocarbenium moiety, similar to the already discussed structure of Figure HS-4-A. This interaction forces all the hydride shift steps to "open" the C-O interaction before the charge can be relocated to the next carbon. It is important to note that this stabilization of the cation charge through the O-C bond formation also comes at a price, which is a forced boat conformation of the 6-membered alkaloid ring. It is widely known that chair conformations are typically more favored than boat and twist-boat.[82] Still, the formation of a boat-like conformation in structure **F4-D** is compensated by the high stability of the oxocarbenium species.

The direct [1,4]-hydride shift that leads to **F4-D** (Figure HS-4-A) presents a very high activation barrier ($\Delta G^{\ddagger}$(**F4-A→F4-D'**) = 27.9 kcal/mol). While in **F4-A** the alkyl ring presents a chair-like conformation, in the transition state **F4-TS$_{AD}$**, the alkyl ring presents a boat-like conformation. As a result, this step requires a large geometric distortion of **F4-A** until the transition state structure is achieved. In **F4-A**, the carbons Cα and Cδ are 2.88 Å apart from each other and need to be pushed together until the distance of 2.14 Å in **F4-TS$_{AD}$** (shown in Figure HS-5). Due to this geometric constraint, a free carbocation intermediate **F4-D'** is formed that quickly yields the 6-membered oxocarbenium product **F4-D** through an intramolecular stabilization process. Although this pathway would lead to the 6-membered oxocarbenium product in a single step, the kinetic impediment of this step discards the viability of [1,4]-hydride shifts in these cyclic systems.

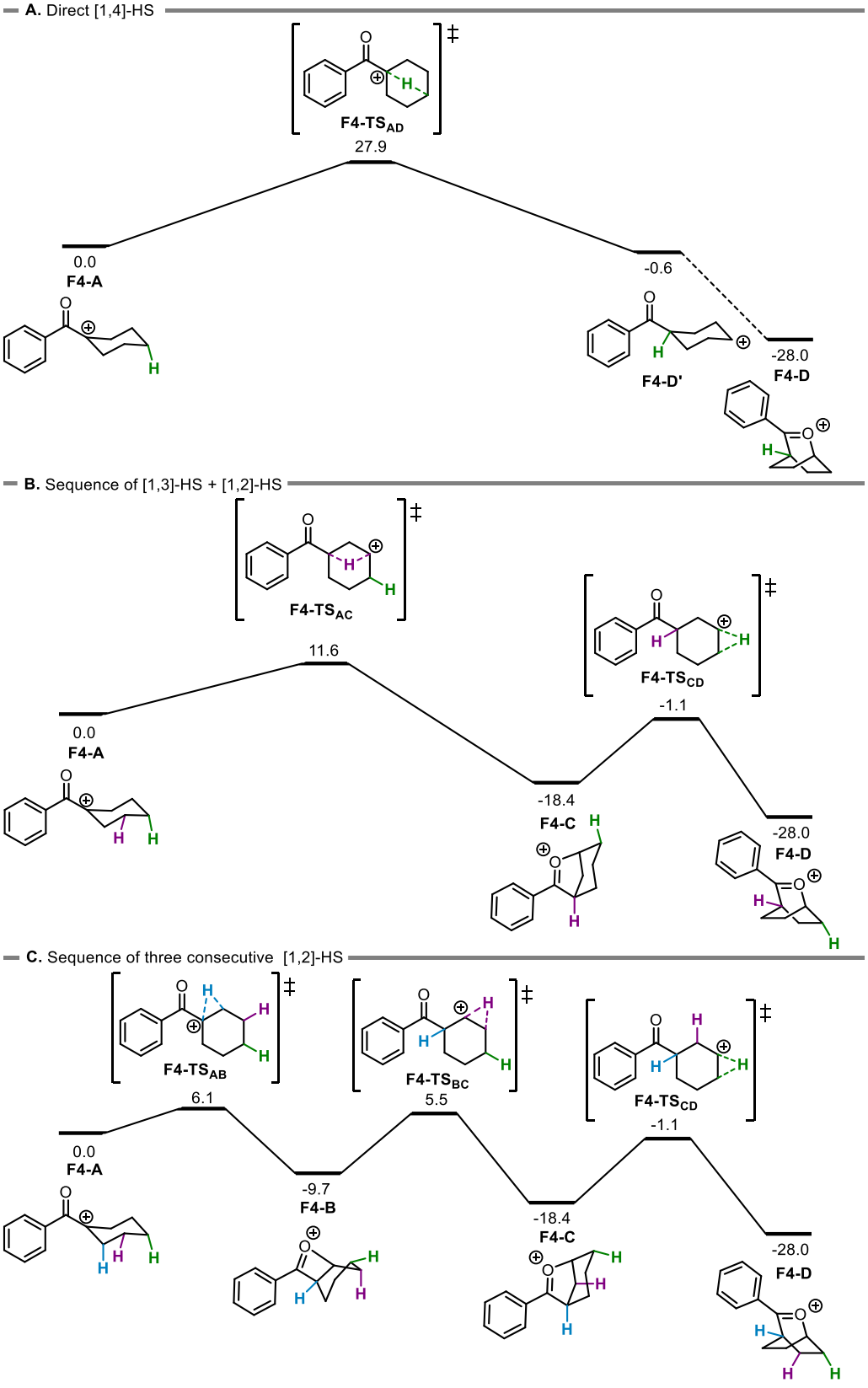

*Figure HS-4 – Computed Gibbs free energy profile for hydride shift processes leading to the formation of a 6-membered ring oxocarbenium: A) Direct [1,4]-shift; B) [1,3]-shift followed by a [1,2]-shift; C) Sequence of three [1,2]-shifts. The reactant complex **F4-A** serves as a reference (0.0 kcal/mol), and the included explicit solvent molecule (DCM) was omitted from the scheme for clarity.*

As an alternative to the direct pathway, an initial [1,3]-hydride shift (Figure HS-4-B) presents a significantly lower activation barrier ($\Delta G^{\ddagger}$(**F4-A→F4-C**) = 11.6 kcal/mol). Similarly to the [1,4]-hydride shift step (**F4-A→F4-D**), a large geometric perturbation of **F4-A** is required for the transition state structure to be achieved in step **F4-A→F4-C**, as the carbons Cα and Cγ lie 2.52 Å apart in **F4-A** and 1.80 Å apart in **F4-TS$_{AC}$**. This exergonic step results in the formation of a 5-membered oxocarbenium intermediate **F4-C** (ΔG(**F4-A→F4-C**) = -18.4 kcal/mol). A final [1,2]-hydride shift, resulting from the "opening" of the oxocarbenium C-O interaction in **F4-C**, allows the cationic charge to migrate to the δ-position to the carbonyl, yielding **F4-D** with a moderate activation barrier ($\Delta G^{\ddagger}$(**F4-C→F4-D**) = 17.3 kcal/mol). From this [1,2]-hydride shift, the product **F4-D** is obtained directly, unlike in the previously discussed pathway (Figure HS-4-A). The high thermodynamic favorability of this step (ΔG(**F4-C→F4-D**) = -9.6 kcal/mol) is related to the transformation of a 5,6-bridged bicyclic ring system in **F4-C** to a 6,6-bridged bicyclic ring in **F4-D**, which shows a slightly stronger C-O interaction ($D_{C\delta\text{-}O}$ = 1.47 Å in **F4-D** while $D_{C\delta\text{-}O}$ = 1.49 Å in **F4-C**).

Finally, the sequential pathway of [1,2]-hydride shifts (Figure HS-4-C) starts with step **F4-A→F4-B**, presenting a very small activation barrier ($\Delta G^{\ddagger}$(**F4-A→F4-B**) = 6.1 kcal/mol) and leading to a 4-membered oxocarbenium intermediate **F4-B**. Step **F4-A→F4-B** is exergonic (ΔG(**F4-A→F4-B**) = -9.7 kcal/mol), even though a secondary carbocation is formed at the β-position in **F4-B** (while **F4-A** presented a tertiary carbocation at the α-position). The high thermodynamic stability of intermediate **F4-B** comes mainly from a stronger Cβ-O interaction, with a length of 1.50 Å in **F4-B**, while in **F4-A**, the Cα-O interaction has a length of 2.17 Å. The second [1,2]-hydride shift, step **F4-B→F4-C**, presents a higher activation barrier than the previous step ($\Delta G^{\ddagger}$(**F4-B→F4-C**) = 15.2 kcal/mol). Once more, the hydride shift needs to open the oxocarbenium ring. Step **F4-B→F4-C** is also more exergonic than the previous step, as the formation of a highly stable 5-membered oxocarbenium intermediate, **F4-C**, is achieved (ΔG(**F4-B→F4-C**) = -8.7 kcal/mol). The last step of the [1,2]-hydride shift sequence, is shared with the previous pathway (**F4-A→F4-C→F4-D**, presented in Figure HS-4-B).

For the profiles of Figure HS-4-B and Figure HS-4-C, the last [1,2]-hydride shift, presenting a barrier of 17.3 kcal/mol, defines the apparent activation energy of both profiles, which is consistent with the

experimental conditions (reaction time of 10 minutes at 25 °C). It is also worth noting that the kinetic feasibility of these steps is highly dependent on the thermodynamic stability of the formed oxocarbenium intermediates. These have to undergo an opening of the C-O interaction to allow the hydride shift steps to occur. To better understand the kinetic favorability of [1,2]-hydride shifts, the 3D structure of the transition state structures of the [1,4]-, [1,3]- and the first [1,2]-hydride shifts are presented in Figure HS-5 (**F4-TS$_{AD}$**, **F4-TS$_{AC}$** and **F4-TS$_{AB}$**, respectively).

The transition state for the [1,4]-hydride shift, **F4-TS$_{AD}$**, presents a bicyclic 5-membered ring structure, in which the H-Cα bond is being formed at a longer distance than the H-Cδ bond is being cleaved ($D_{H\text{-}C\alpha}$ = 1.42 Å while $D_{H\text{-}C\delta}$ = 1.27 Å), which suggests this structure to be an early transition state. As mentioned before, this hydride shift step forces the alkyl chain to adopt a boat-like conformation. Resembling this structure, in **F4-TS$_{AC}$** the H-Cα bond is also being formed at a longer distance than the H-Cγ bond is being cleaved ($D_{H\text{-}C\alpha}$ = 1.80 Å while $D_{H\text{-}C\gamma}$ = 1.17 Å). These results could point to an early transition state, in which a smaller degree of geometric distortion of the reactant is required for the transition state structure to be achieved, which typically indicates a kinetically facilitated process. However, this structure presents a distorted 4-membered ring (formed by H, Cα, Cβ and Cγ) with a high contraction of the Cα-Cβ-Cγ angle (72 °)that contributes to the lower thermodynamic stability of **F4-TS$_{AC}$** when compared to **F4-TS$_{AB}$**. In the latter, the H-Cα bond is formed at a distance 0.13 Å shorter than the H-Cβ bond is being cleaved ($D_{H\text{-}C\alpha}$ = 1.27 Å while $D_{H\text{-}C\beta}$ = 1.40 Å), pointing to a late transition state. Nonetheless, the lack of significant constraints in the chair-like conformation of the alkyl ring contributes to the overall stabilization of this structure and the kinetic favorability of [1,2]-hydride shifts.

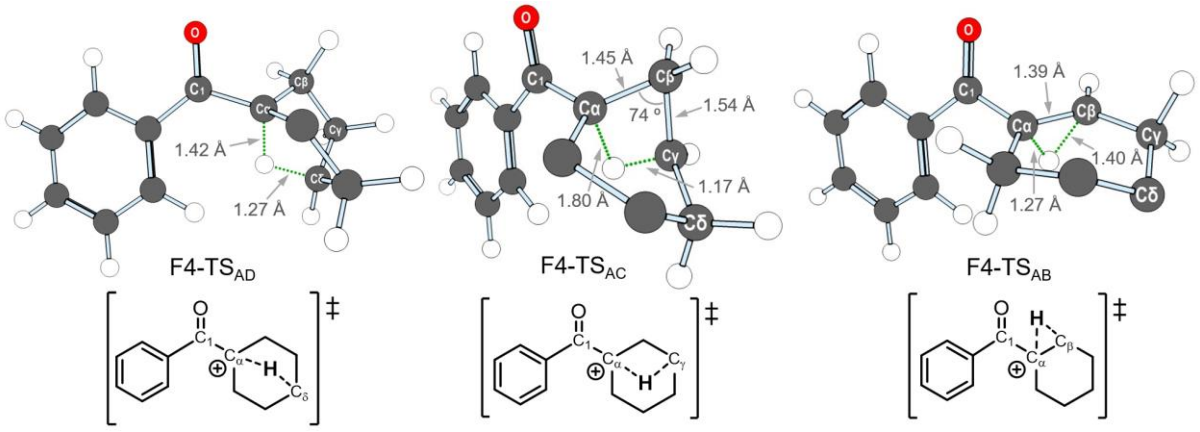

Figure HS-5 – 3D representation of the computed hydride shift transition state structures with the length of selected bonds.

At this stage, it was decided to verify the ability of the chosen computational model to reproduce experimentally obtained data. To this end, key bond distances and bond angles were selected as a means to compare the geometry of **F4-D**, which contains a hydrogen atom at the δ-position to the carbonyl, with the SC-XRD crystal structure of **S11-4**, which contains a *t*Bu group in the δ-position (Scheme HS-11). For direct comparison purposes, the geometry of **S11-4** was also optimized with the same level of theory (**F4-D$_{tBu}$**), as presented in Figure HS-6. Most of the distances for the computed structures present a deviation smaller then 0.01 Å from the experimentally obtained structure of **S11-4**. The only exception is the O-Cδ bond, corresponding to the oxocarbenium interaction where the computed structures present slightly shorter distances. Given that the computational results are performed with a microsolvation approach (implicit solvation model and the inclusion of an explicit solvent molecule), it is possible that this small deviation is derived from directional solvent interactions that are not present in the crystal structure where the O-Cδ bond becomes elongated. Thus, the comparison of these structural parameters supports the use of the chosen computational model for the study of carbocationic systems.

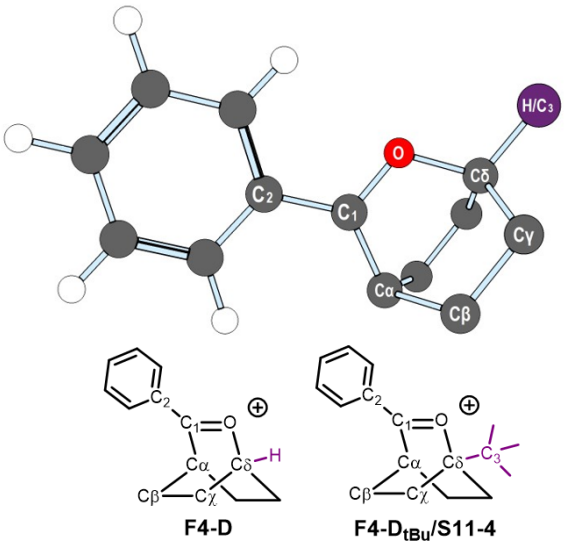

Distances (Å)	F4-D	F4-D_{tBu}	S11-4
C_1-C_2	1.438	1.441	1.439
C_1-Cα	1.477	1.475	1.481
Cα-Cβ	1.548	1.543	1.547
Cβ-Cγ	1.535	1.535	1.542
Cγ-Cδ	1.520	1.531	1.533
Cδ-C3	Cδ-H bond	1.549	1.549
C_1-O	1.284	1.279	1.290
Cδ-O	1.468	1.484	1.516
Angles (°)	**F4-D**	**F4-D_{tBu}**	**S9-4**
C_1-O-Cδ	115.2	117.1	115.5
C_2-C_1-O	117.5	117.4	116.9

Figure HS-6 – Representation of selected distances (Å) and angles (°) of the optimized structure of the 6-membered oxocarbenium intermediate.

Overall, the results obtained for this cyclic system show that the thermodynamic product should be obtained experimentally. However, it is necessary to deactivate the feasibility of side reactions, especially intermolecular elimination. This goal can therefore be achieved by using substrates in which the elimination products would not be thermodynamically favored (i.e., cycloalkane groups that would rather form oxocarbenium intermediates than cycloalkenes).

3.5. Investigation of [1,5]-hydride shifts

The mechanistic investigations performed in this work have revealed the kinetic unfeasibility of the [1,3]- and [1,4]-hydride shifts in the studied systems. We decided to investigate the mechanistic viability of hydride shifts with a longer range to occur in cationic systems. To this end, we have focused on a reported work from the Maulide lab in 2019, in which a [1,5]-hydride shift step was suggested to occur in the context of a reductive coupling reaction of chiral alkenes and aldehydes without further computational investigation.[83,84] Part of the work presented in this section has been recently published.[85]

Carbon-carbon coupling approaches combining aldehydes and alkenes, which are widely available compounds, have recently emerged as new alternatives to classical carbonyl addition approaches. While previous works in the field focused on the synthesis of branched coupling products, the recently reported

work of Maulide and co-workers, as shown in Scheme HS-12-A, focuses on the use of a cationic process to allow the synthesis of linear C-C coupling products. These compounds are common structural motifs in a diverse range of biologically active natural products.[86–88]

The reported reaction requires a Lewis catalyst, iron(III) chloride, that is expected to activate the aldehyde, allowing the nucleophilic attack of the alcohol to the carbonyl to generate the oxocarbenium intermediate **S12-2**. These species are prone to a cyclisation step, yielding the tertiary carbocation **S12-3**, which can be followed by a [1,5]-hydride shift leading to the 8-membered oxocarbenium intermediate **S12-4**. A final hydrolysis step would then be responsible for the ring opening of this intermediate to yield the observed linear coupling products. Experimentally, it was also observed that this reaction exhibited very high enantioselectivity, with the exclusive formation of (*R*,*R*)-configured products when using an (*S*)-configured alkene.

It was also observed that the same reaction with an alkene containing an additional carbon in the alkyl chain, **S12-1A'**, did not yield the equivalent product, **S12-5'**. This result is especially interesting because the expected mechanism would involve a similar [1,5]-hydride shift. However, it would occur from a 9-membered oxocarbenium intermediate, while the reported reaction is expected to involve an 8-membered oxocarbenium, **S12-3**. Therefore, we performed the mechanistic study of the reaction of methyl aldehyde with **S12-1A** and with **S12-1A'** to understand the origin of the experimentally observed enantioselectivity and if the key for a successful reaction is the [1,5]-hydride shift.

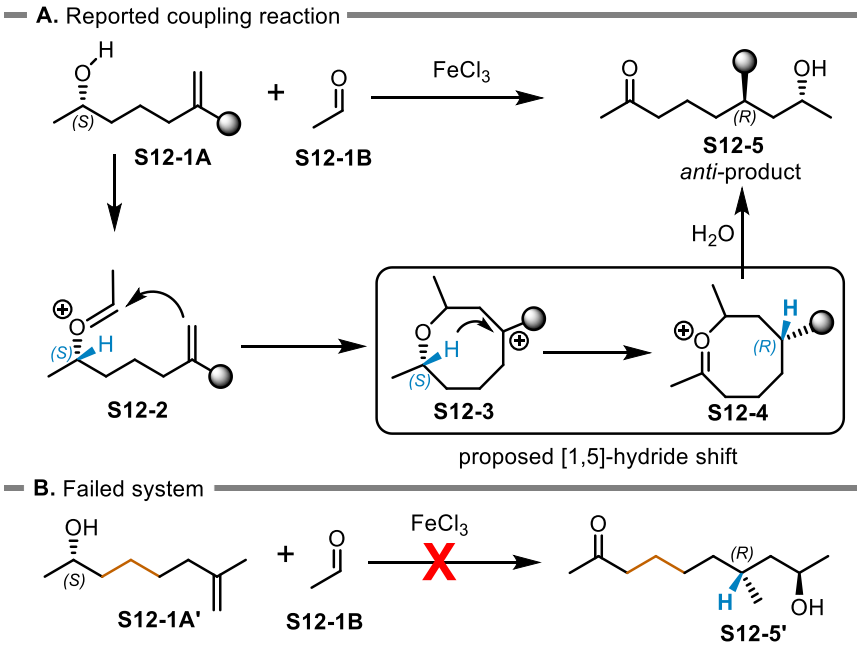

Scheme HS-12 – A) Proposed mechanism for Lewis acid-catalyzed coupling of alkenes and aldehydes involving a potential [1,5]-hydride shift; B) Attempted reaction of an alkene containing and additional carbon in the chain which did not yield the expected coupling product.

The reaction profile for the formation of the cyclic oxocarbenium intermediate equivalent to **S10-4** (Scheme HS-3) was computed at the B3LYP-D3(BJ),SMD(DCM)/def2-TZVP//B3LYP-D3(BJ),SMD(DCM)/def2-SVP level of theory, with BF_3 as a Lewis acid replacement for the experimentally used $FeCl_3$ for computational expediency. An explicit solvent molecule (dichloromethane) was included to assist in the stabilization of the charged species Figure HS-7). The reactant complex **F7-A**, which is composed of the (*S*)-enantiomer of the chiral alkene **S10-1A** (Scheme HS-12-A) and an adduct of formaldehyde with BF_3 (the Lews acid catalyst).

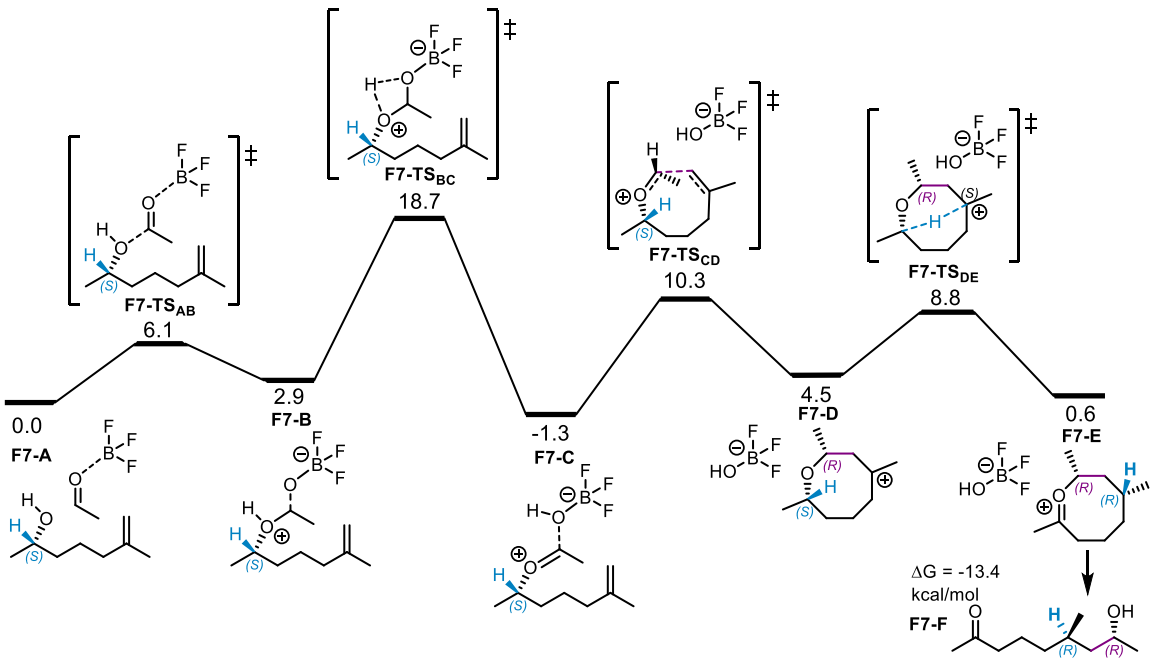

*Figure HS-7 – Computed Gibbs free energy profile for the coupling of an aldehyde with an alkene. The reactant complex **F7-A** serves as a reference (0.0 kcal/mol) and the included explicit solvent molecule (DCM) was omitted from the scheme for clarity.*

From the reactant complex **F7-A**, the activated aldehyde is subject to a nucleophilic attack by the alcohol group of the chiral alkene, forming intermediate **F7-B**. This step is slightly endergonic (ΔG(**F7-A→F7-B**) = 2.9 kcal/mol) but also presents a very low activation barrier ($\Delta G^{\ddagger}$(**F7-A→F7-B**) = 6.1 kcal/mol), resulting in a fast and reversible step. The transient formation of intermediate **F7-B** allows an exergonic proton transfer event to occur (ΔG(**F7-B→F7-C**) = -4.2 kcal/mol), yielding intermediate **F7-C**, which is an adduct of an oxocarbenium with BF_3OH^-. This proton transfer step occurs through a 4-membered ring transition state and presents a relatively high activation barrier ($\Delta G^{\ddagger}$(**F7-B→F7-C**) = 15.8 kcal/mol). The next step is a cyclization, which occurs through a C-C bond formation with the terminal alkene (step **F7-C→F7-D**). During this process, the O-C bond between the oxocarbenium and the Lewis acid adduct is cleaved, releasing BF_3OH^- and a new C-C bond is formed to yield an 8-membered tertiary carbocation intermediate **F7-D** with a low kinetic barrier ($\Delta G^{\ddagger}$(**F7-C→F7-D**) = 11.6 kcal/mol). Notably, a new chiral center is formed in this step, represented in Figure HS-7 in purple. Finally, **F7-D** can undergo a transannular [1,5]-hydride shift that forms the 8-membered oxocarbenium intermediate **F7-E**. This hydride shift is responsible for a chirality transfer event, as the (*S*)-configured carbon bound to oxygen loses its tetrahedral geometry and the tertiary carbocation

becomes an (*R*)-configured tertiary carbon. Although the formation of **F7-D** is endergonic (ΔG(**F7-C→F7-D**) = 5.8 kcal/mol), the following [1,5]-hydride shift is kinetically favored to reverting the cyclization step, leading to the formation of **F7-C** from **F7-D** ($\Delta G^{\ddagger}$(**F7-D→F7-E**) = 4.3 kcal/mol while $\Delta G^{\ddagger}$(**F7-D→F7-C**) = 5.8 kcal/mol). A hydrolysis step forms the experimentally observed linear coupling product upon quenching the reaction with water. A proposed mechanism for this process is shown in Scheme HS-13, starting with a nucleophilic attack of an OH^- group to the oxocarbenium **S13-A** that yields the hemiacetal intermediate **S13-B**. This step can be followed by a proton transfer that opens the ring and forms the linear coupling product **S13-C**. Therefore, the incorporation of the OH^- fragment, together with the regeneration of the Lewis acid catalyst, BF_3 to yield the product complex **F7-F** is an exergonic process (ΔG(**F7-E→F7-F**) = -13.4 kcal/mol).

According to the energetic span model, an apparent activation barrier of 18.7 kcal/mol can be estimated for this process, defined by the free energy difference between **F7-A** (rate-determining intermediate) and **F7-TS$_{BC}$** (rate-determining transition state). This barrier is consistent with the reaction conditions and is not affected by either the cyclization or the [1,5]-hydride shift steps.

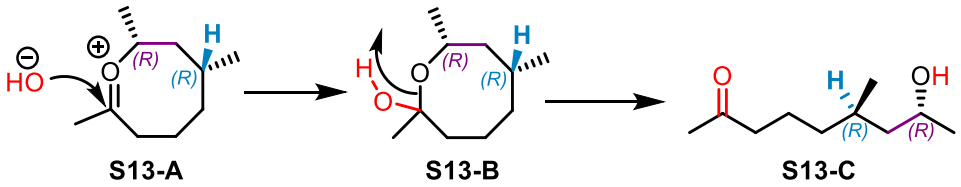

Scheme HS-13 – The proposed mechanism for the hydrolysis step leading to a linear product.

It was mentioned before that the cyclization step presented in Figure HS-7 (step **F7-C→F7-D**) generates a new (*R*)-configured chiral center in the system and, thus, can be enantioselective. To verify our hypothesis, we searched for the transition state of a cyclization into the (*S*)-configured intermediate **F7-TS$_{CD'}$**. A 3D representation of the geometry of the most stable conformation of these competing transition states is shown in Figure HS-8. The cyclization transition state leading towards an (*S*)-configuration of C_1 (**F7-TS$_{CD'}$**) is 4.6 kcal/mol less stable than **F7-TS$_{CD}$**, which is depicted in the mechanistic pathway of Figure HS-7. The lower stability of **F7-TS$_{CD'}$** is reflected in the distance at which the C_1-C_2 bond is formed (1.99 Å), which is 0.19 Å shorter than the C_1-C_2 distance in **F7-TS$_{CD}$** (2.17 Å). Therefore, the structure of **F7-TS$_{CD'}$** is only achieved with a higher distortion of **F7-C**, with

these carbons being pushed closer together, which is an indication of a late transition state. It is worth noting that the most favorable conformations of both these transition states present the methyl substituent of the carbon C_1 in the equatorial position. However, whereas the methyl substituent of the carbon C(*S*) occupies the equatorial position in **F7-TS$_{CD}$**, in **F7-TS$_{CD}$'** this methyl group is forced into an axial position. The proximity (and therefore the repulsion) between the methyl group and the alkene group (C_2), increases the trans-annular strain of the ring structure. As an outcome, the transition state structure is destabilized, increasing the kinetic barrier of the cyclization. The resulting kinetic preference towards **F7-TS$_{CD}$** is then responsible for a complete enantioselectivity of the cyclization step.

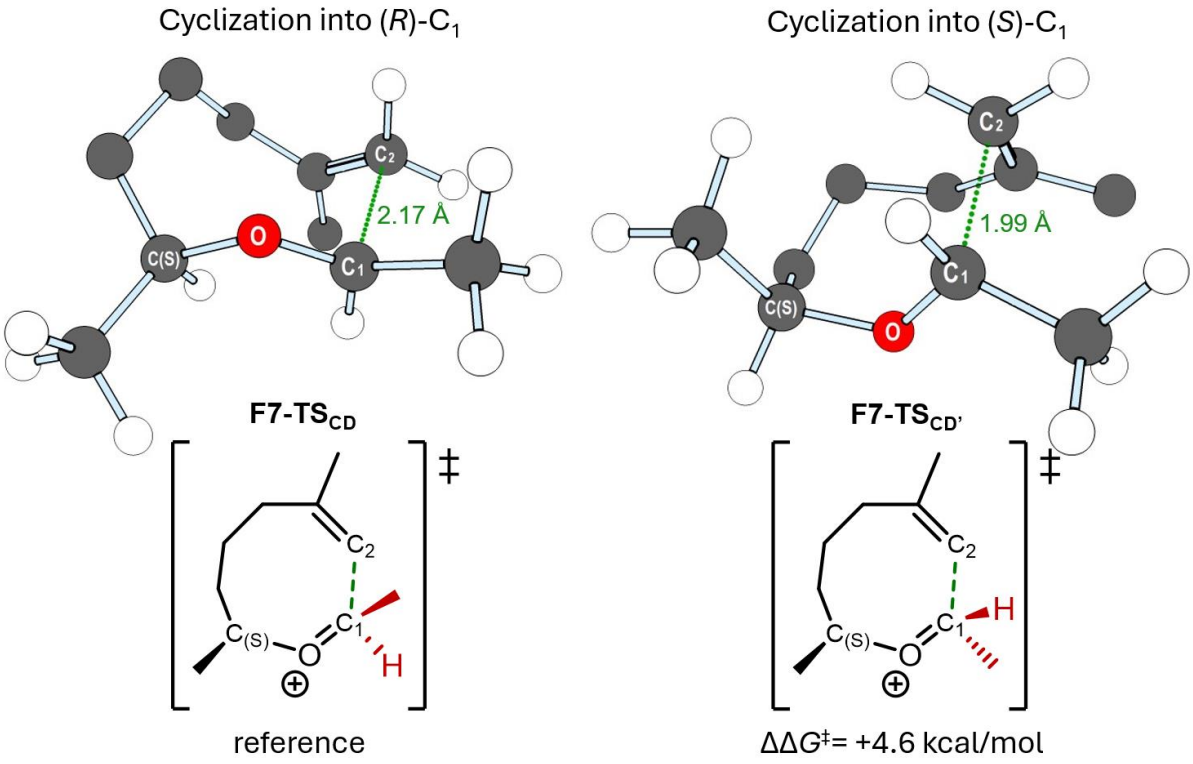

Figure HS-8 – 3D representation of the computed cyclization transition state structures and thermodynamic stability comparison, along with the highlighted length at which the C-C bond is formed.

The 3D structure of the transition state of the [1,5]-hydride shift discussed in the energy profile of Figure HS-7 (**F7-TS$_{DE}$**) is shown in Figure HS-9. Importantly, this step is responsible for a chirality transfer from the (*S*)-configured carbon C(*S*) to C_3, which becomes (*R*)-configured after the formation of the C_3-H bond. This hydride shift leads to a bridged bicyclic transition state structure with a C(*S*)-H bond cleavage at shorter length (1.13 Å) than the forming C_3-H bond (1.92 Å), corresponding to an early transition state. As an alternative to this step, the hydrogen could migrate to the opposite face of the

carbocation which would result in a *(S)*-configured center (**F7-TS$_{DE'}$**). However, unlike **F7-TS$_{DE}$**, **F7-TS$_{DE'}$** is a late transition state in which the C(*S*)-H bond needs to be stretched until 1.24 Å and the C_3-H is formed only when these nuclei are 1.15 Å apart. Furthermore, this hydride shift is achieved with a significant contraction of the 8-membered ring until a bridged bicyclic ring structure is obtained, presenting a C(S)-H-C_3 angle of 169° (while 123° in **F7-TS$_{DE}$**). As a result, **F7-TS$_{DE'}$** presents a very high instability when compared to **F7-TS$_{DE}$** (36.7 kcal/mol less stable) and is kinetically prohibited. This supports our proposed enantioselective pathway for the formation of the linear coupling product **F7-F**.

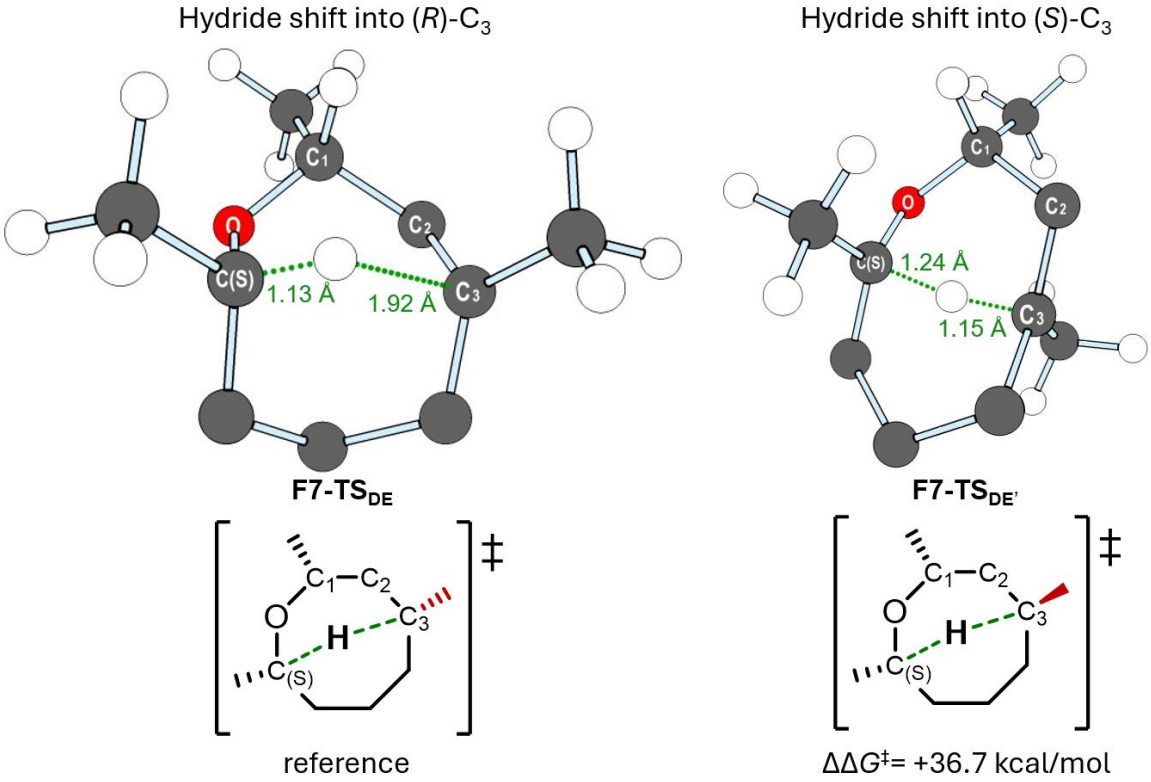

Figure HS-9 – 3D representation of the computed [1,5]-hydride shift transition state structures and thermodynamic stability comparison, along with the highlighted length at which the C(S)-H bond is cleaved and the C_3-H bond is formed.

Although our computational results support that a [1,5]-hydride shift should be kinetically feasible for large ring systems, the reaction of an alkene with an additional carbon in the alkyl chain did not yield the expected linear coupling product experimentally. It is then important to understand which step is responsible for the unfeasibility of this reaction, whose obtained mechanistic pathway is presented in Figure HS-10 in orange, together with the equivalent steps belonging to the mechanism of Figure HS-7 in black.

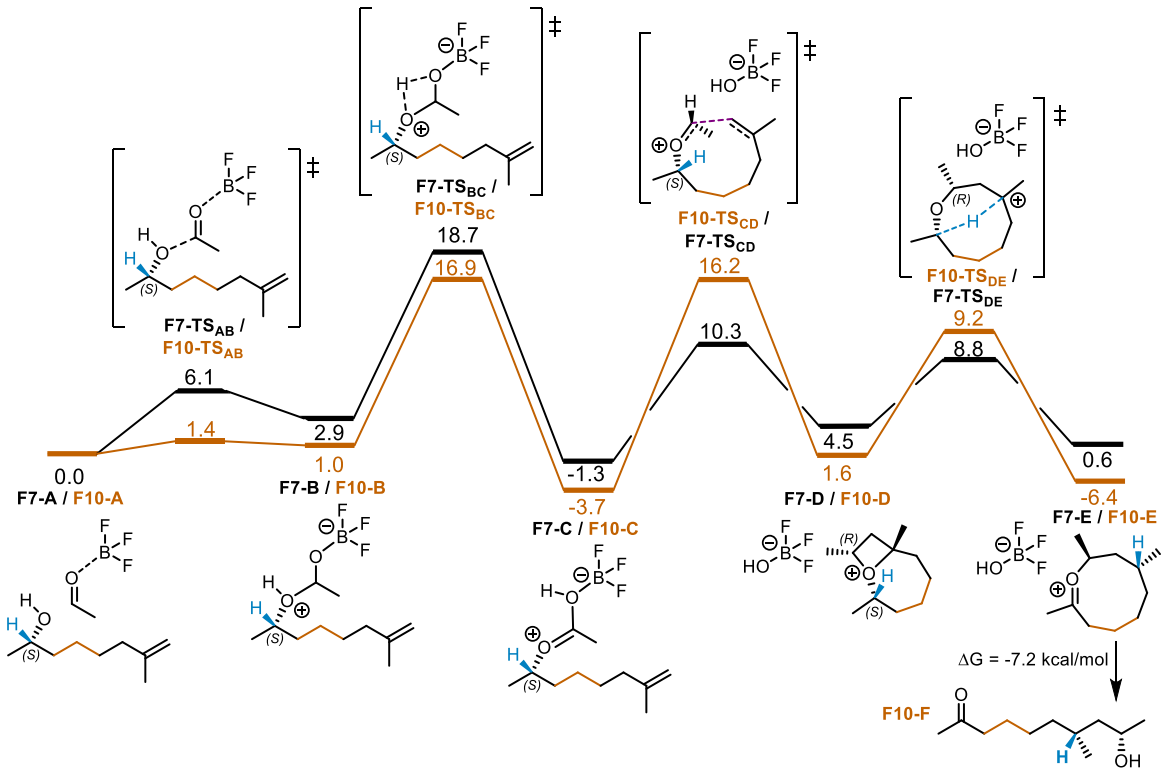

*Figure HS-10 – Computed Gibbs free energy profile for the coupling reaction of an alkene with a longer chain (orange), overlayed with the previously obtained profile (black). The reactant complexes **F7-A** and **F10-A** serve as a reference (0.0 kcal/mol) for each profile, and the explicitly included solvent molecule (DCM) was omitted from the scheme for clarity.*

The obtained mechanistic profile for the reaction of formaldehyde and an alkene with an additional methylene in the chain presents the same elemental steps as the previously discussed mechanism (Figure HS-7). However, significant differences can be observed in the relative stability of the reaction intermediates and transition states. The profile of the extended alkyl chain (in orange) presents a lower activation barrier for the first two steps (**F10-A→F10-B** and **F10-B→F10-C**), resulting in an overall activation barrier of 16.9 kcal/mol (obtained between **F10-A** and **F10-TS$_{BC}$**). These involve the nucleophilic attack of the alcohol to the activated aldehyde and a subsequential proton transfer to form the oxocarbenium intermediate **F10-C**. The longer alkyl chain likely results in a lower steric repulsion between the terminal alkene and the activated aldehyde fragment, allowing higher stability of these structures when compared to the profile in black (one less carbon in the alkyl chain). From **F10-C**, the cyclization into a 9-membered ring is the rate-determining step, presenting the highest barrier of the profile ($\Delta G^{\ddagger}$(**F10-C→F10-D**) = 19.9 kcal/mol). The formation of **F10-D** is endergonic (ΔG(**F10-C→F10-D**) = 5.3 kcal/mol) and this intermediate contains a 4-membered oxocarbenium ring in its

structure, formed through a C-O interaction that contributes to the stabilization of the cationic charge. This interaction is not observed in **F7-D** and results from the higher flexibility of the 9-membered ring of **F10-D**. The following [1,5]-hydride shift step presents a higher activation barrier than the equivalent step in the black profile ($\Delta G^{\ddagger}$(**F10-D→F10-E**) = 7.6 kcal/mol, while $\Delta G^{\ddagger}$(**F7-D→F7-E**) = 4.3 kcal/mol), which can be understood by the need to open the C-O interaction in the oxocarbenium intermediate **F10-D**. The formation of the 9-membered oxocarbenium intermediate **F10-E** is exergonic (ΔG(**F7-D→F7-E**) = -8.0 kcal/mol) and the thermodynamic stability of this structure is likely related to the low steric repulsion of the substituent groups of the flexible ring.

These results show that the extension of the alkyl chain in the alkene reagent leads to more flexible intermediates, allowing the intramolecular stabilization of the cationic charge. As a result (with more stable intermediates), the activation barrier for both cyclization and [1,5]-hydride shift steps are increased. With the imposition of this kinetic impediment, the pathway towards the formation of the expected linear alkene products becomes less competitive with alternative side reactions, such as intermolecular proton transfers that can lead to a significant number of unidentified products. Therefore, we can conclude that the feasibility of [1,5]-hydride shift in ring structures is highly dependent on the low stability of the preceding intermediate structures.

3.6. Frontier orbital analysis

The term hydride shift presupposes the intervention of a hydride (hydrogen anion) in the reaction step. However, the computational study of the kinetic and thermodynamic properties of these processes allows their comprehension as a charge migration coupled with a proton transfer (Figure HS-11). Starting from species **F11-1**, a carbocation with a sp^2 hybridization has an empty p orbital at carbon C_s. The vicinal carbon C_t has a filled bonding orbital (lower in energy). With a sufficient approximation of the hydrogen to C_s, a structure like **F11-2** can be achieved, where the destabilization of the C_t-H bonding orbital can be compensated by the stabilization of the empty p orbital of C_s. As a result, a new bonding orbital is formed between C_t and the hydrogen, while C_s is left with an empty p orbital. The relaxation of the geometry of **F11-2** yields the carbocation intermediate **F11-3**. We can consider hydride shifts as

processes composed of three elementary steps: geometry destabilization, electronic configuration redistribution and geometry relaxation, where:

- Each hydride shift occurs in a single mechanistic step
- The energy profiles will not involve free hydride species
- The carbocation and the CH groups need to be close to each other

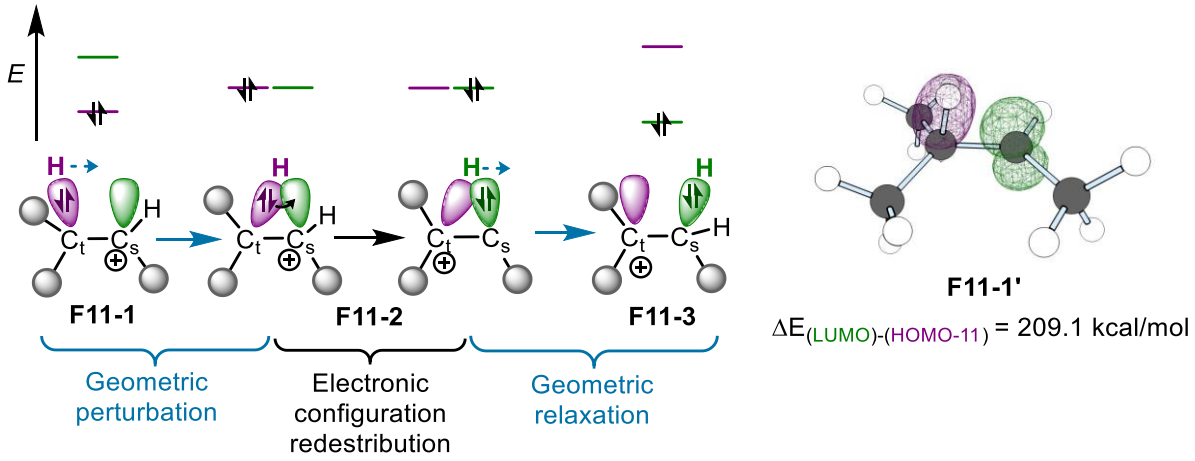

Figure HS-11 – Schematic representation of the stepwise sequence involving a [1,2]-hydride shift and computed frontier orbital energy gap for a model system.

In addition to these considerations, the analysis of the energy gap between the empty orbital of the carbocation and the filled orbital responsible for the C-H bond could potentially be of interest when studying hydride shifts. Taking a simple carbocation as a model, the Kohn-Sham orbitals of a structure equivalent to **F11-1** with methyl substituents, **F11-1'**, were computed. The energy gap between the C_t-H bonding orbital (HOMO-11) and the empty *p* orbital of C_s (LUMO) have a difference in energy of 209.1 kcal/mol. It is worth noting that the activation barriers for the hydride shift steps presented in this work are extremely small when compared to the energy gap of these orbitals. Therefore, frontier orbital analysis of carbocations is not recommended for studying carbocationic species due to large discrepancies in the energy scale in relation to thermodynamic studies.[89]

3.7. Conclusions and outlook

This study has proposed computationally feasible mechanisms for four types of hydride shift as means to achieve C-H functionalization reactions and thoroughly investigated their occurrence across different carbocation frameworks. Our findings indicate that the [1,2]-hydride shift is the kinetically most favorable process compared to [1,3]- and [1,4]-shifts, particularly in linear or six-membered ring

systems. However, in certain cases, such as in larger rings (10- and 11-membered), a long-range [1,5]-hydride shift can become competitive. Specifically, we identified that this shift is prominent in ring-mediated coupling reactions between alkenes and aldehydes.

Our calculations suggest that ring-mediated reactions facilitate long-range hydride shifts. There is a critical ring size beyond which (>11 carbon atoms) side elimination processes become more likely due to the conformational flexibility of the intermediates involved. Thus, we conclude that linear hydride shifts are confined to [1,2]-hydride shift sequences, which can influence the stereoselectivity of the reaction.

In silico analysis reveals the highly transient nature of carbocation intermediates, contributing to the difficulty in controlling these reactions and an increased likelihood of side-product formation. This aligns with the experimental observation, where products expected from a predicted [1,3]-hydride shift mechanism were overshadowed by side reaction products. Future computational and experimental studies on long-range hydride shifts should focus on suppressing these side elimination reactions to improve the yield and selectivity of the desired products.

4. Chapter II: C-H activation in cationic cyclopropanation reactions

The following results have been partially published in a peer-review journal.[90] This chapter focuses on the computational study conducted to understand the mechanistic insights an observed cyclopropanation reaction and predict further modifications to extend its applicability.

4.1. Cyclopropane rings

Cyclopropanes are three-membered rings formed by the connection of three alkyl carbons. These rings present high strain due to the forced 60° angle between the three carbons, while a linear alkyl chain presents C-C-C angles of 109°. Although this structural constraint poses a significant challenge to the synthesis of these compounds, the cyclopropane moiety is a structural feature present in several natural products and pharmaceutical compounds used in modern treatments.[91,92] Some examples are shown in Scheme CCP-1, which include synthetic drugs containing a cyclopropane moiety attached to an alkyl chain (Scheme CCP-1-A) and natural products (Scheme CCP-1-B).

In the design of drugs that interact with proteins and enzymes, one key factor to consider is the entropic component associated with protein-drug interactions. A drug in solution can adopt numerous possible conformations due to intra- and inter-molecular interactions with the solvent. However, cavities in enzymes to which the drug binds are tolerant to a reduced conformational space of the drug. Thus, the binding event reduces the entropy. To increase the affinity of a drug to the enzyme, one common approach is to reduce the entropic penalty of the binding by developing more rigid molecules that present a smaller amount of conformations in solution. A possible way to increase the rigidity of a molecular scaffold is the introduction of a cyclopropane ring in alkyl chains. This modification imposes a higher conformational constraint to the alkyl chain than an alternative gem-dimethyl functionalization. Cyclopropanation has been applied to drugs such as Montelukast, used in the treatment of chronic asthma, Lumacaftor, which can be applied in combination with other drugs to treat symptoms of cystic fibrosis, and Factor Xa Inhibitor, a blood thinning agent. In natural products, cyclopropane rings can exist as part of multi-cycle scaffolds, as is the case of Peyssonnoside A (sugar adduct) and

Pentalenolactone P, or even as the central scaffold unit, as is the case of Chrysanthemyl pyrophosphate which contains a tetra-substituted cyclopropane ring at its core.[93]

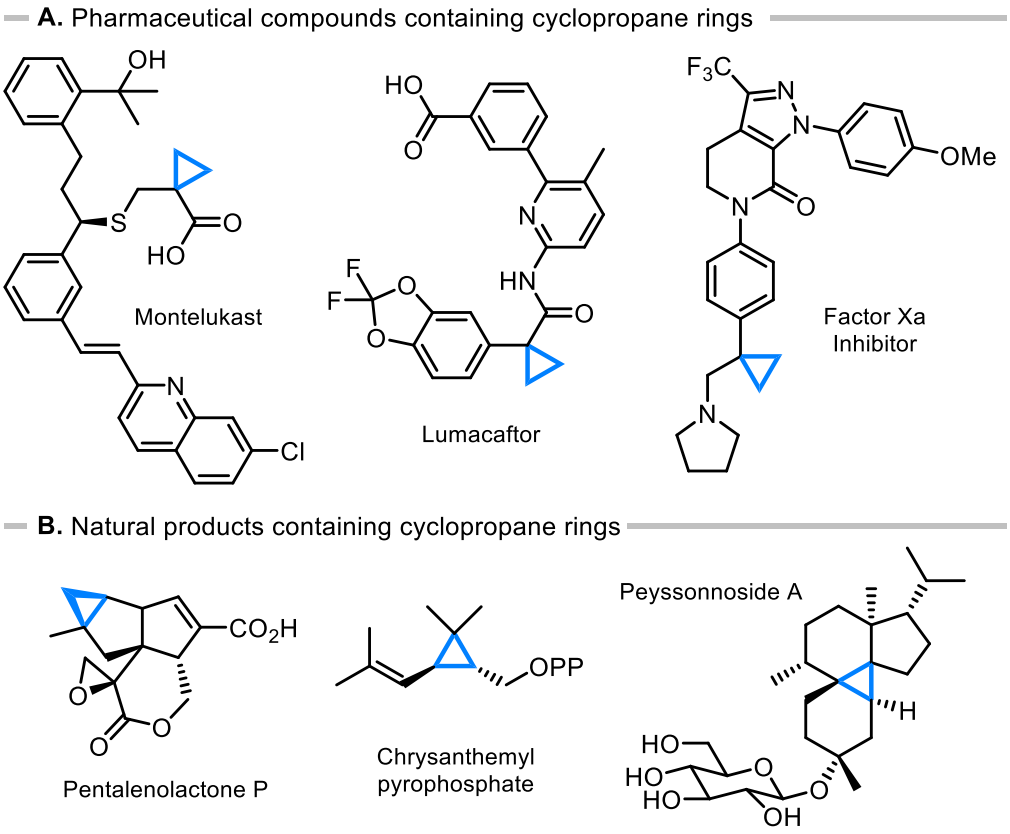

Scheme CCP-1 – Compounds containing cyclopropane rings: A) Pharmaceutical compounds; B) Natural products.

A widely used method to generate cyclopropane rings was reported by Simmons and Smith in 1958.[94] This approach achieves cyclopropanation through the cycloaddition of methylene and an olefin by treatment of diiodomethane with zinc−copper couple Zn(Cu). The synthetic utility of this method derives from a wide scope of tolerated olefin substrates stereospecificity of the overall transformation. The development of this reaction focused mainly on the use of different methylene sources to avoid the use of Zn(Cu), which requires a challenging preparation. The protocol reported by Furukawa and co-workers (Scheme CCP-2-A) involves the formation of the carbenoid species **S2-1** from the reaction of diiodomethane with $ZnEt_2$.[95] The zinc-mediated cycloaddition of the methyl group to the alkene **S2-2** results in the stereoselective formation of a cyclopropane ring in product **S3-3**, where the stereochemical information of the olefin is maintained. The Simmons-Smith reaction is not able to promote

cyclopropanation with unsubstituted olefins, and therefore, other synthetic methods were developed. This is the case of the free carbenoid pathway reported by Doering and Hoffmann (Scheme CCP-2-B).[96] In this approach, the treatment of chloroform, **S2-4**, with a mixture of KO*t*Bu in *t*BuOH is believed to lead to the formation of the deprotonated chloroform intermediate **S2-5**, which can add to the olefin **S2-2** to yield the chlorinated cyclopropane product **S2-3'**. This reaction is very exergonic and requires cooling to -78 ºC, which limits its applicability in an experimental setting. More recent methods are still dependent on transition metal catalysts, as is the case of the nickel-promoted cyclopropanation reaction reported by Jarvo and co-workers (Scheme CCP-2-C).[97] This transformation exploits the scaffold of the substrate **S2-7**, where the abstraction of leaving groups allows a cyclopropanation event leading to the experimentally observed product **S2-8**.

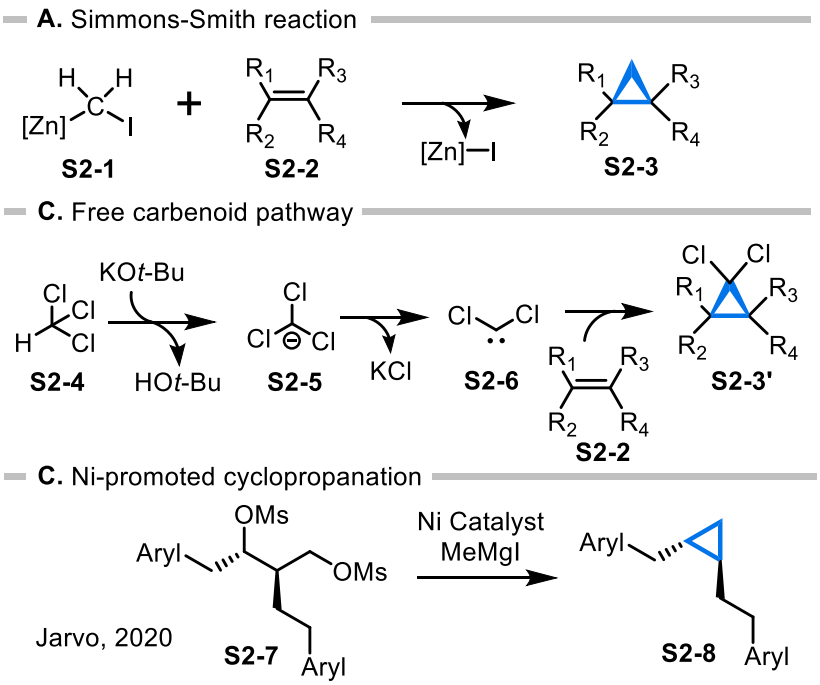

Scheme CCP-2 – Reported experimental approaches to achieve cyclopropanation.

The search for cyclopropanation methods that avoid the use of transition metals is an ongoing process that has recently turned toward the study of natural synthetic pathways. These have revealed the formation of cyclopropane-containing compounds through metal-free transformations that promote an efficient C–H activation. One key enzymatic process responsible for the formation of these compounds is a cationic cyclopropanation. Generally, these reactions start with the formation of a carbocation in a

controlled enzymatic medium with the abstraction of a leaving group (Scheme CCP-3). The carbocation **S3-1** can be stabilized by an interaction with a neighboring C–H group to form the non-classical carbocation intermediate **S3-2**, known in the literature as a protonated cyclopropane (PCP+). This species is highly acidic and, through deprotonation, yields the cyclopropane **S3-3** as product. The existence of protonated cyclopropane intermediates was initially proposed by Collins in 1968.[98] However, due to their high instability, such intermediates have never been isolated to this date. As a result, PCP+ structures have only been studied computationally, with the first report from Houk and co-workers in 1997, who described the nonclassical carbocation as "a trans-alkene that is bridged symmetrically by an alkyl cation" (Scheme CCP-3-B).[99] In the reported structure, computed at the MP2/6-311G* level of theory, the three carbons of the cyclopropane are in the same plane as the hydrogen atom H_a. C_1 and C_2 present a distance of 1.39 Å, which is close to a carbon-carbon double bond, while the C_1-C_3 and C_2-C_3 distances are longer than the typical length of 1.54 Å of a single bond (1.84 Å and 1.86 Å respectively).

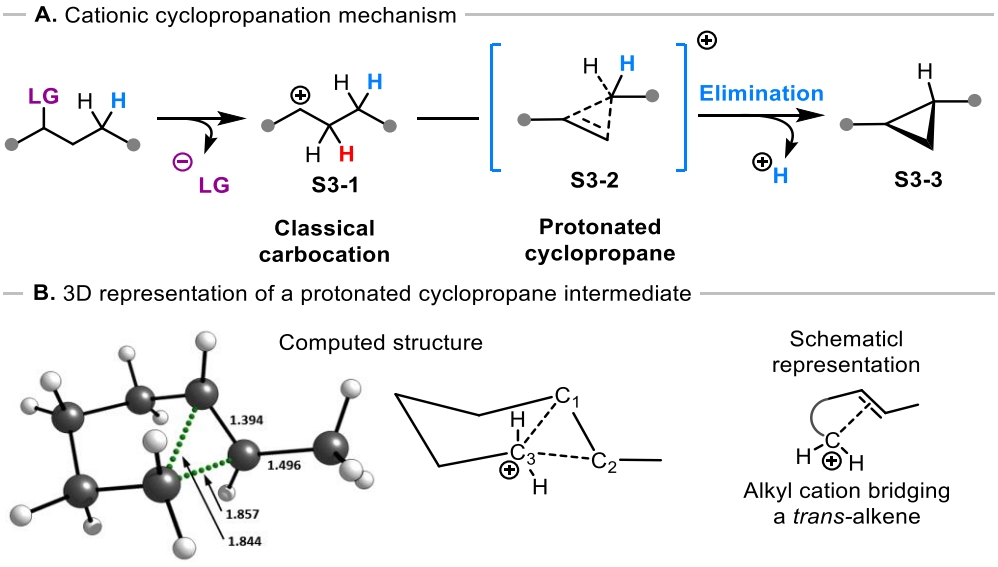

Scheme CCP-3 – A) Representation of a proposed mechanism for a cationic cyclopropanation reaction; B) 3D representation of a reported protonated cyclopropane structure computed by Houk and co-workers with selected bond distances in Å.

Nature has evolved with the design of highly efficient enzymatic processes. They present high substrate specificity, which is a beneficial attribute in the biological medium. However, the usefulness of enzymatic transformation is highly dependent on our ability to apply it to different molecules. Therefore,

one major challenge in converting an enzymatic process into an organic chemistry reaction lies in overcoming the substrate specificity of the enzyme to allow a chemical transformation with high substrate tolerance. While computational chemistry approaches can be very beneficial to the development of chemical reactions, there are very few reported works of computational studies associated with cationic cyclopropanation. Several works have been focused on understanding the properties of hypothetical models, for instance, the theoretical study of PCP+ formation from $C_6H_{13}^+$ reported by East and co-workers or on studying experimentally observed reactivity.[99,100] However, the use of computational chemistry to predict experimental conditions that allow cationic cyclopropanation processes to occur has not been reported prior to this work.

4.2. Cationic cyclopropanation in organic chemistry

While in an enzymatic medium, any unstable intermediate is protected within the cavity of the enzyme, in organic synthesis approaches, the intermediates are solvated and can interact with other solvated species, possibly leading to undesired side reactions. In particular, carbocations are known to be highly unstable species that can quickly undergo elimination reaction to form olefins. Therefore, the conversion of enzymatic cationic cyclopropanation to organic synthesis faces a major challenge, which is controlling the generated carbocation reactivity. As shown in Scheme CCP-4, after the *in situ* generation of the carbocation **S4-1**, the pathway comprising the formation of the desired protonated cyclopropane intermediate, followed by deprotonation, is in competition with β-elimination reactions that lead to undesired olefin products, such as **S4-2**.

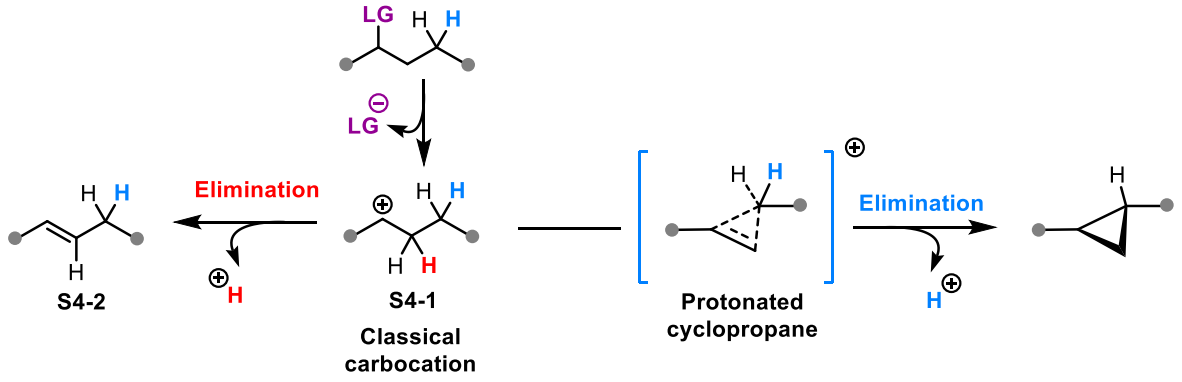

Scheme CCP-4 – Representation of the proposed mechanism for cationic cyclopropanation and the competing elimination reaction that leads to undesired alkene products.

Until now, some synthetic attempts have successfully transferred the reactivity of enzymatic cationic cyclopropanation to organic synthesis. In 1996, Lerner and co-workers synthesized the bicyclic compound **S5-2**, containing a cyclopropane ring, by subjecting the alkene **S5-1** to the enzyme IgG TM1-87D7.[101] Although this reaction still requires a biocatalyst, the transformation of a linear substrate into a bicyclic product is fascinating. It showcases the possibility for a carbocation generated at the γ-position to a double bond to yield a cyclopropane moiety. In 2007, Tantillo and co-workers computationally studied the formation of a protonated cyclopropane intermediate with a norbornyl scaffold (Scheme CCP-5-B).[100] Similarly to the structure reported by Houk and co-workers, C1 and C2 lie 1.40 Å apart, which is close to a carbon-carbon double bond, while the C1–C3 and C2–C3 bonds are elongated (both with a length of 1.89 Å). The same norbornyl framework was also explored by Maulide and co-workers, who reported a cyclopropanation reaction (Scheme CCP-5-A).[102] This reaction accepts amides and silyl enol ethers as substrates but was only successful with norbornyl scaffolds.

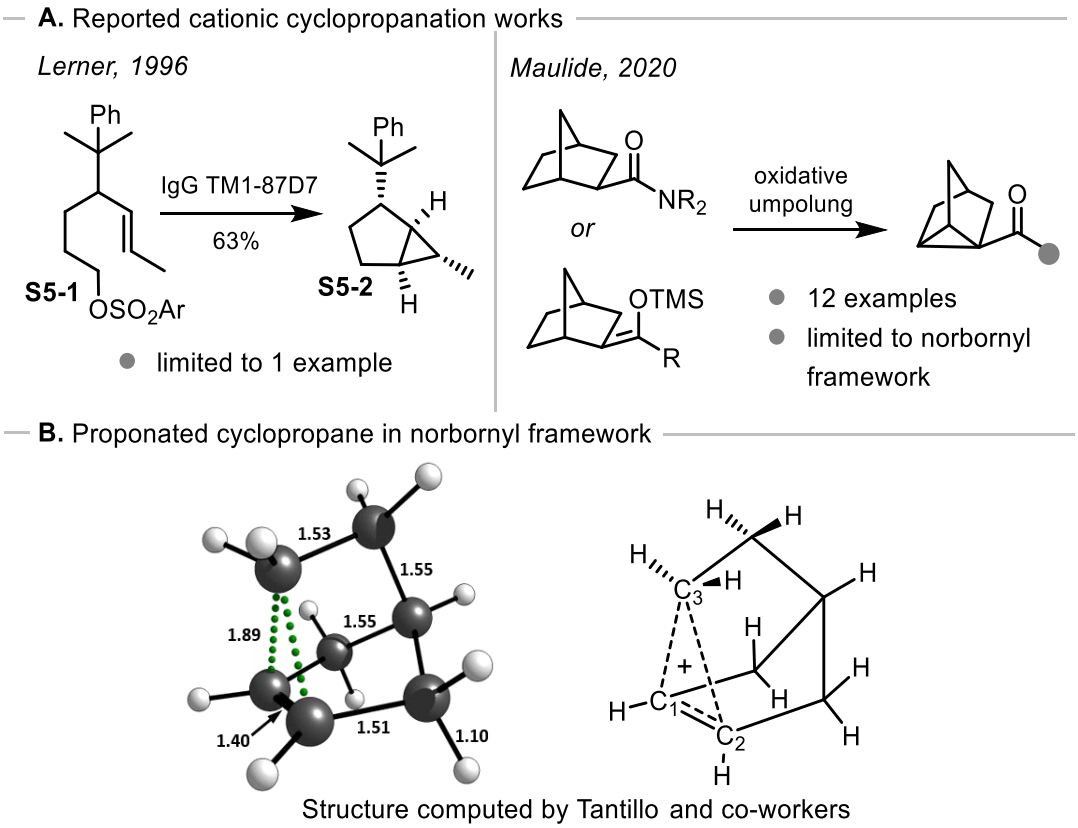

Scheme CCP-5 - A) Reported reactions exploiting a cationic cyclopropanation step; B) 3D representation of a reported protonated cyclopropane structure computed by Tantillo and co-workers with selected bond distances in Å.

The transformation reported by Maulide and co-workers (Scheme CCP-5-A) is especially interesting since the protonated cyclopropane structure in the norbornyl scaffold could potentially yield bicyclic alkene side-products(Figure CCP-1). Considering the formation of a bicyclic carbocation species (**F1-1**) through the abstraction of a leaving group, a protonated cyclopropane intermediate **F1-2** can be obtained through intramolecular stabilization. From this intermediate, the abstraction of an edge proton of the protonated cyclopropane moiety (H_a) leads to the cyclopropane product **F1-A**, while the abstraction of H_b leads to a bicyclic alkene product **F1-B**. Although the formation of **F1-B** was not observed experimentally, **F1-A** presents a highly strained 3-membered alkane ring, which could thermodynamically disfavor the cyclopropanation event. Therefore, as a preliminary investigation, the thermodynamic feasibility of the cyclopropanation event was investigated at the PBE0-D3(BJ),SMD(DCM)/def2-TZVP//PBE0-D3(BJ),SMD(DCM)/def2-SVP level of theory. The Gibbs free energies of **F1-A** and **F1-B** were computed, revealing that the formation of a cyclopropane ring is indeed thermodynamically favorable by 6.2 kcal/mol. This result shows that cyclopropane products can be obtained as thermodynamic products of cationic reactions.

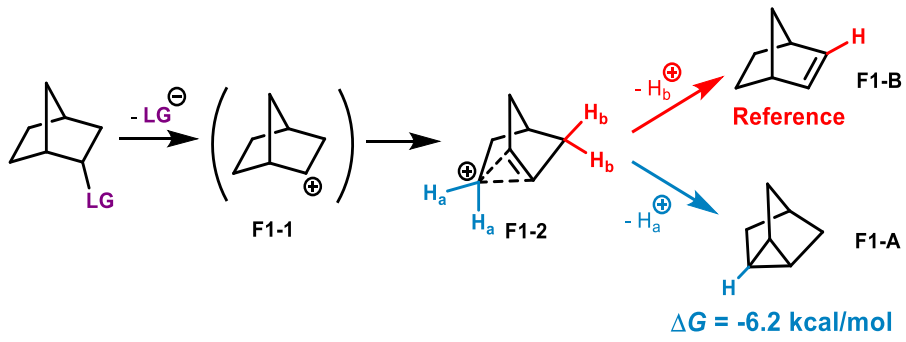

Figure CCP-1 – Representation of the divergent pathway from a PCP+ species in a norbornyl scaffold that can lead towards an alkene of a cyclopropane ring and thermodynamic stability comparison of the two possible products.

Another example of cationic cyclopropanation was reported by Farina and co-workers, who revealed that the reaction of a 7-*epi* Taxol derivative with diethylaminosulfur trifluoride (DAST), a fluorinating agent, did not result in fluorination of the Taxol scaffold.[103] Instead, a cyclopropanation reaction was observed (Scheme CCP-6-A). The proposed mechanism involves a putative protonated cyclopropane intermediate that is formed after the abstraction of a hydroxyl group and follows the cationic cyclopropanation mechanism discussed earlier (Scheme CCP-4). It is not clear to this day which factors

affect the selectivity of this reaction towards the cyclopropane-containing product. However, in similarity to the reported systems discussed in Scheme CCP-5-A, the cyclopropane ring is generated as part of a bicyclic motif. The same is observed in the synthesis of pentanolactone P, reported by Williard and co-workers, in which the abstraction of a hydroxyl group forms a bicyclic motif containing a cyclopropane (Scheme CCP-6-B).[104,105] These results strongly indicate that the control of cationic cyclopropanation reactions can highly benefit from the rigid structural features of the substrates. Therefore, the presented work was focused on investigating the formation of bicyclic systems containing cyclopropane motifs.

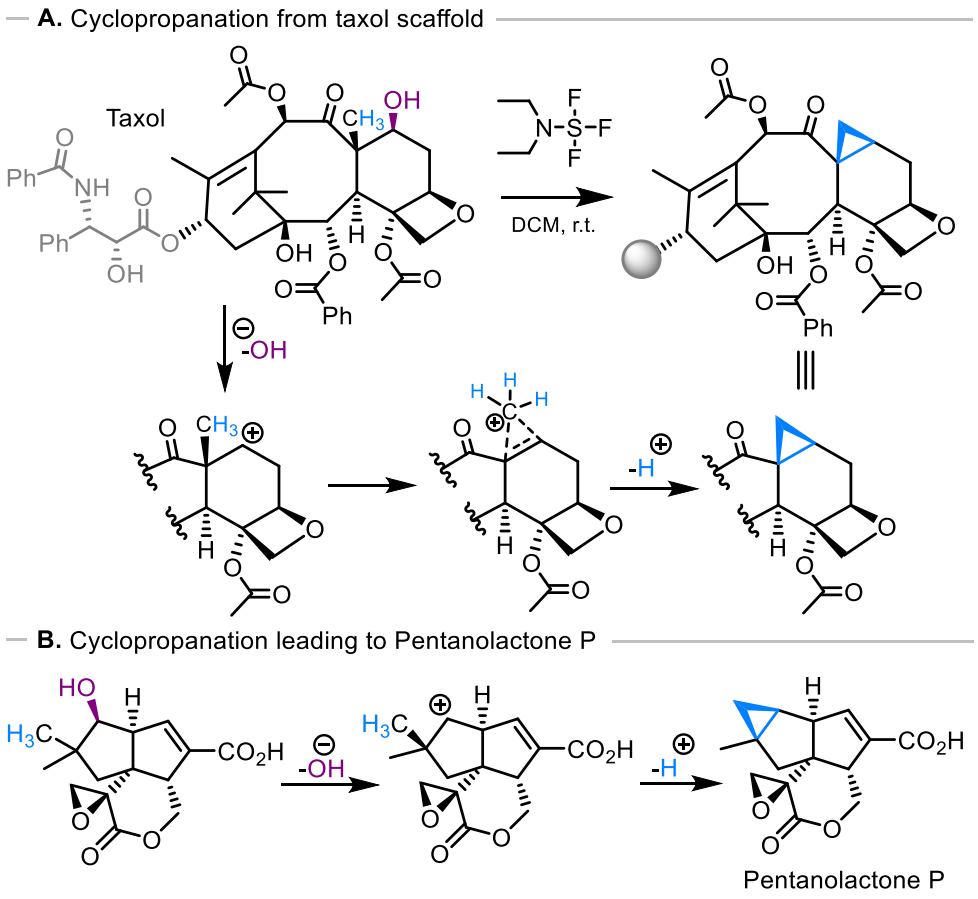

Scheme CCP-6 – Representation of the cationic cyclopropanation mechanism in: A) the reaction of Taxol with DAST; B) the formation of Pentanolactone P.

4.3. Cationic cyclopropanation from cyclodecadienes

In recent work of the Maulide group, an attempt to develop a retrosynthesis method to obtain 6,8-cycloeudesmanes revealed that the reaction of cyclodecadiene with *N*-Bromosuccinimide (NBS) yields the desired structural scaffold. 6,8-cycloeudesmanes are secondary metabolites that can be extracted

from marine seaweed and contain a multi-cycle structure, including a cyclopropane ring.[106] This discovery sparked interest in its application to other molecular scaffolds since it allows not only a cyclopropanation event but also the synthesis of complex ring structures. Such cyclopropanation reaction is expected to occur through an initial electrophilic addition of bromonium to the most substituted and, therefore, more electron-rich double bond of the cyclohexadiene. This bromonium addition generates a secondary carbocation in intermediate **S7-1** that can be attacked by the second double bond of the system, forming a trans-annular C–C bond. The resulting intermediate, **S7-2**, is again a secondary carbocation that can undergo intramolecular stabilization to yield the protonated cyclopropane intermediate **S7-3**. At this stage, any species that can act as a base, such as the N-succinimide anion, is able to abstract a proton from the protonated cyclopropane moiety to form the experimentally observed 6,8-cycloeudesmane.

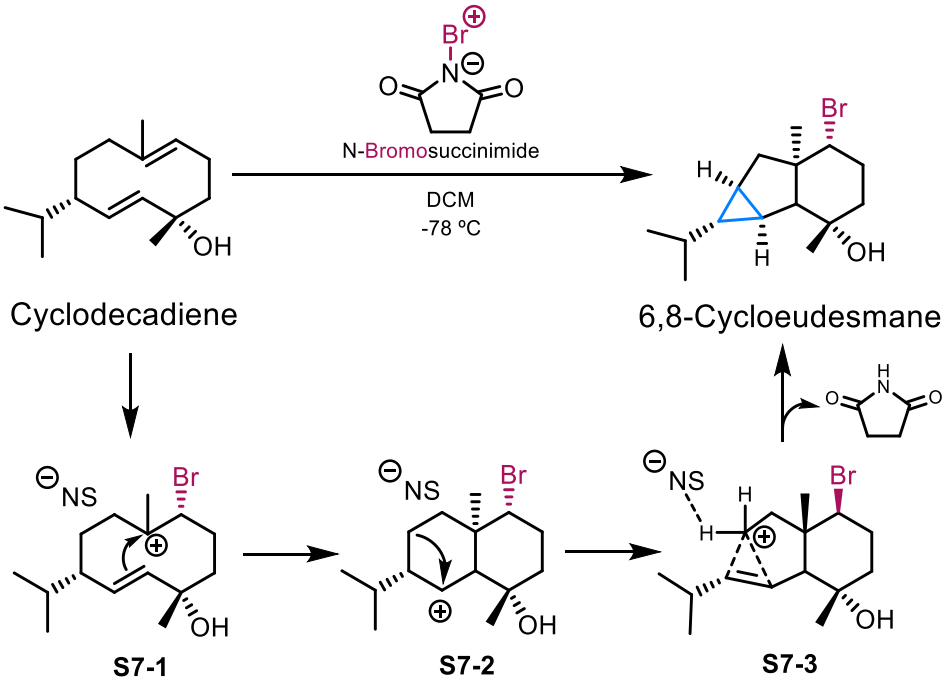

Scheme CCP-7 – Observed cyclopropanation reaction leading to the formation of 6,8-cycloeudesmane, along with the initially proposed mechanism for the transformation.

The cationic cyclopropanation reaction was further investigated through the modification of experimental conditions. To this effort, chloronium and iodonium were also tested as viable halonium sources with the use of *N*-Chlorosuccinimide (NCS) and *N*-Iodosuccinimide (NIS), respectively (Scheme CCP-8-A). The reaction of the decadiene **S8-1** with NBS gave the cyclopropane-containing

product in 36% yield, which is a similar result to the reaction of **S8-1** with NCS (also 36% yield for the formation of the 6,8-cycloeudesmane product). However, when the reaction was attempted with NIS, the desired product was not observed.

The role of the hydroxyl group in the mechanism of the transformation was also investigated by methylation of the hydroxyl group of the substrate **S8-1** to yield substrate **S8-2**. The reactions of **S8-2** with NCS, NBS and NIS were then attempted, providing similar results to those with **S8-1**. A slight decrease in the obtained yield of the cyclopropane product was observed for the reactions with NCS and NBS with **S8-2**, resulting in yields of 34% and 32%, respectively, while a yield of 36% was obtained with **S8-1** when using either NBS or NCS. The reaction with NIS again did not yield the expected cyclopropane product. These results suggest that the hydroxyl group does not play a role in the mechanism of the reaction.

The cyclopropanation reaction with NBS was also attempted using two substrates with a modified structure (Scheme CCP-8-B). The first, **S8-3**, is a cyclodecadiene with a single methyl substituent at position 2, which differs from **S8-1** by not having an isopropyl group at position 5 and no substituents at position 8. The second modified substrate, **S8-4**, still has the isopropyl group at position 5 but is not cyclic. This diene has a cyclohexyl substituent at position 7 (*E*-configured double bond). Both attempts with these structural modifications failed to yield a product containing a cyclopropane ring.

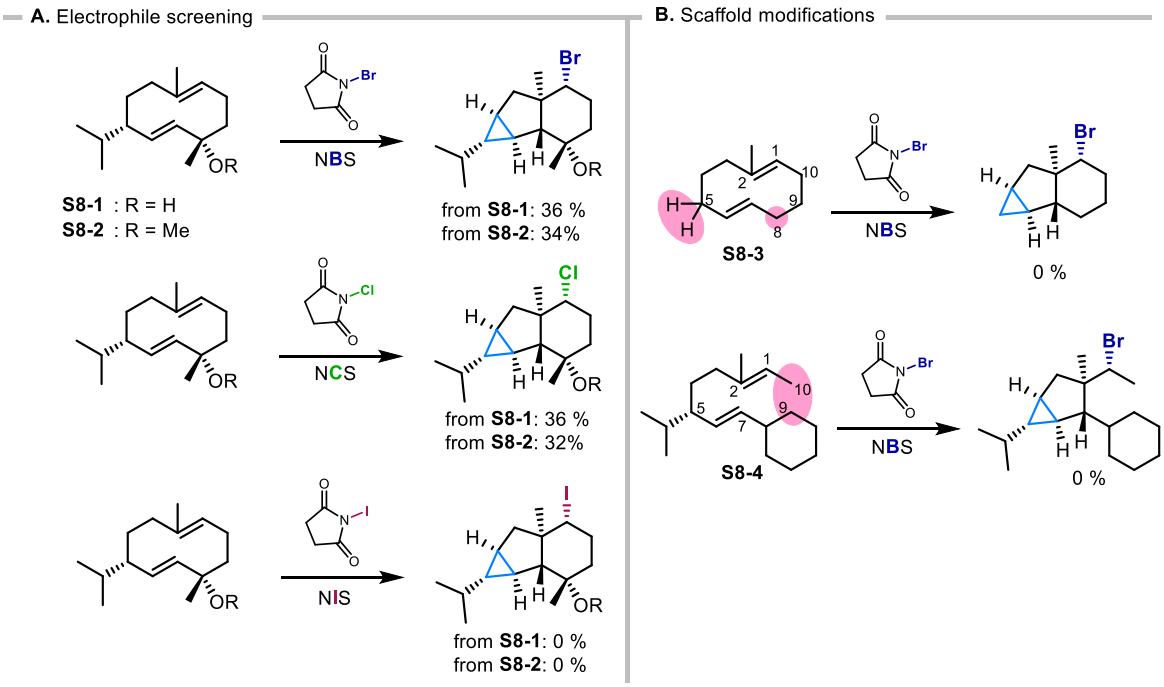

Scheme CCP-8 – Layout of the experimentally attempted reactions: A) with different electrophiles; B) with modifications on the cyclodecadiene scaffold.

To understand the key factors affecting the success of this reaction, a mechanistic study was conducted at the PBE0-D3(BJ)/def2-TZVP,SMD(DCM)//PBE0-D3(BJ)/def2-SVP,SMD(DCM) level of theory. An additional goal of this computational study was to investigate if a protonated cyclopropane intermediate could play a role in this cationic cyclopropanation. The reaction of **S8-1** with NBS was initially studied, as it corresponds to a transformation that yields an experimentally obtained cyclopropane product. The chosen computational model included an explicit solvent molecule. Thus, solvation effects are treated by combining explicit (microsolvation) and implicit (SMD) solvation approaches.

The geometry optimization of **S8-1** already provides insight regarding the feasibility of the studied cyclopropanation reaction. The structure of this decadiene is shown in Figure CCP-2 and presents a double chair conformation in which the two carbon-carbon double bonds are aligned along the horizontal plane, as can be observed in the side-view angle of this species' 3D structure. With these double bonds in close proximity to each other, the two carbon atoms that will form a *trans*-annular carbon-carbon bond upon reaction with NBS lie at a distance of 3.22 Å. Therefore, an electrophilic addition of bromonium, promoted by NBS, results in this C–C bond formation. This proximity appears to be extremely important and is not structurally enforced if the diene is not cyclic, as is the case of **S8-4**

(Scheme CCP-8), which does not lead to a cyclopropane product when a reaction is attempted with NBS.

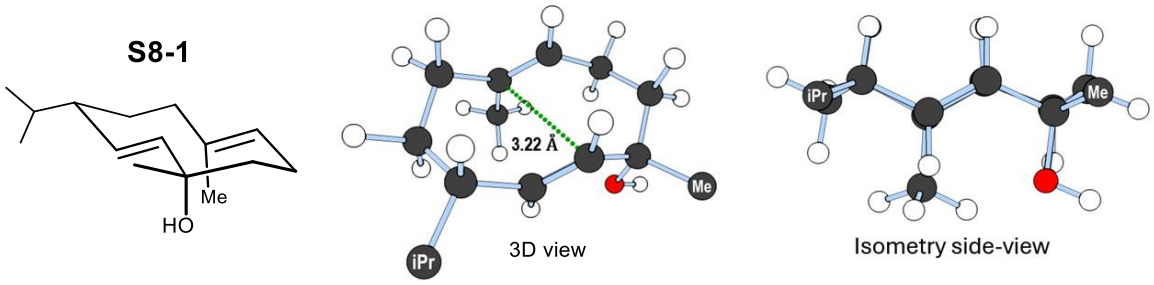

Figure CCP-2 – 3D representation of the cyclodecadiene substrate, highlighting the "double chair" conformation of the ring, which results in the proximity of the two carbon atoms that form a trans-annular C-C bond.

Following a pathway for the initial Br–C bond formation, a potential free energy profile was obtained for the cationic cyclopropanation of **S8-1** (Figure CCP-3-A). The first step of this transformation is a concerted cleavage of the N–Br bond and the formation of one Br–C and two C–C bonds, to yield the intermediate **F3-B**, a protonated cyclopropane. This step presents a moderate activation barrier ($\Delta G^{\ddagger}$(**F3-A→F3-B**) = 14.6 kcal/mol) and is exergonic (ΔG(**F3-A→F3-B**) = -2.1 kcal/mol), highlighting the thermodynamic viability of intramolecular stabilization of carbocationic moieties, leading to non-classical carbocation structures, such as the protonated cyclopropane. From **F3-B**, a proton transfer event to the succinimide anion presents a nearly inexistent activation barrier ($\Delta G^{\ddagger}$(**F3-B→F3-C**) = 0.1 kcal/mol) and yields the experimentally observed 6,8-cycloeudesmane product, whose formation is highly exergonic and therefore irreversible (ΔG(**F3-B→F3-C**) = -40.7 kcal/mol). This very facile step shows that the protonated cyclopropane intermediate is very acidic, similarly to other carbocation species. The optimized (PBE0-D3(BJ)/def2-SVP) 3D structure of this intermediate is presented in Figure CCP-3B, with the counter anion and the explicit solvent molecule hidden to ease the visualization. In this species, the carbon atoms C_A, C_B and C_C, along with the hydrogen atom H_D, are all co-planar, with the carbons C_A and C_B lying at a distance of 1.40 Å, which is close to a carbon-carbon double bond. The C_A–C_C and C_B–C_C bonds present an elongated length (1.68 Å and 1.80 Å, respectively) and the C_C-H bond has a length of 1.01 Å, which is typical for a C–H bond (average of 1.03 Å).[80] These geometric features are consistent with the corner-protonated structure reported by Houk and co-workers in 1997 for a protonated cyclopropane at the MP2/6-311G* level of theory.

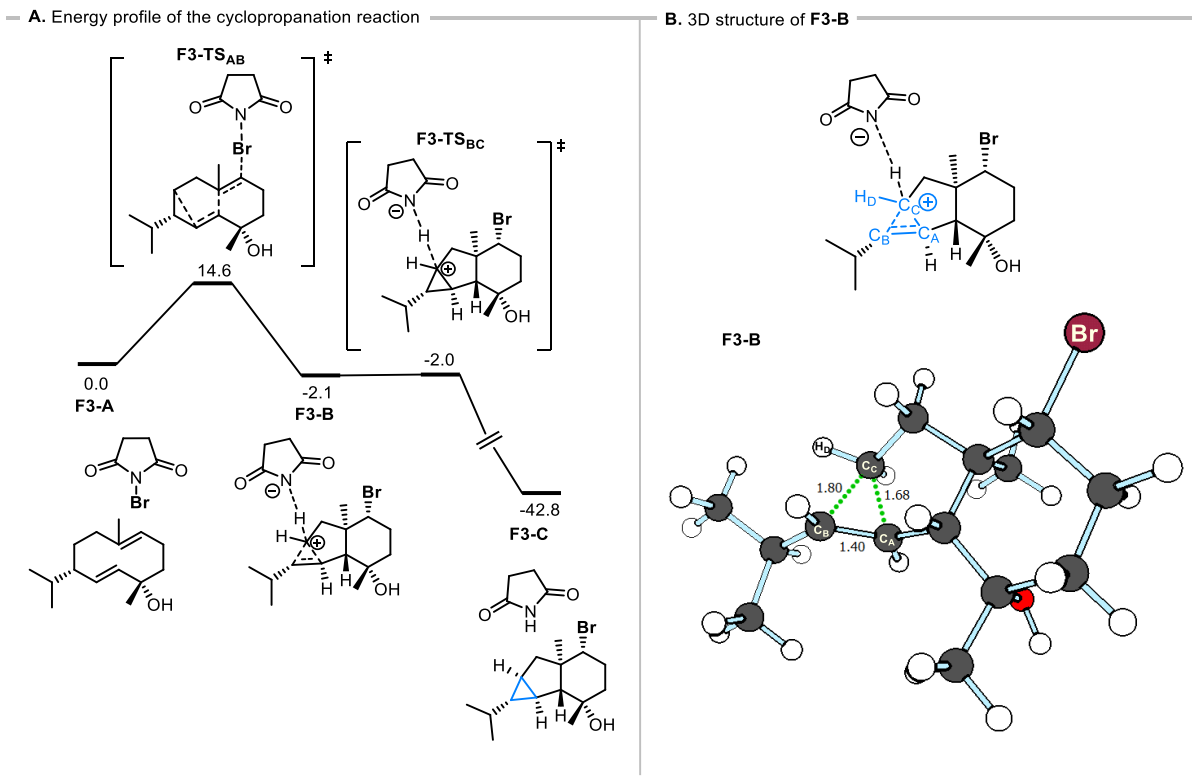

*Figure CCP-3 – A) Computed Gibbs free energy profile for the cationic cyclopropanation reaction. The reactant complex **F3-A** serves as a reference (0.0 kcal/mol), and the explicitly included solvent molecule (DCM) was omitted from the scheme for clarity; B) 3D representation of the protonated cyclopropane intermediate with selected bond distances in Å.*

The results obtained thus far highlight the necessity to form a protonated cyclopropane intermediate, from which a deprotonation event is an extremely facile and irreversible step that yields the desired cyclopropane. It is then highly unlikely that this spontaneous deprotonation can be controlled in the reaction medium. Therefore, to study the reaction path leading to cyclopropane products, it is only required to study the mechanism of the formation of the highly acidic protonated cyclopropane intermediate. Using this approach, the reaction profiles for the experimentally attempted reactions shown in Scheme CCP-8-A, leading to the corresponding protonated cyclopropane intermediate, were investigated.

Figure CCP-4 presents the Gibbs free energy profile for the reaction of **S8-1** with NBS (Figure CCP-4-A) and NCS (Figure CCP-4-B), as well as the reaction of **S8-2** with NBS (Figure CCP-4-C). The profile shown in Figure CCP-4-A is included in Figure CCP-3-A (step **F3-A→F3-B**) and describes a fully concerted step for the formation of the protonated cyclopropane intermediate. An equivalent step is obtained for the reaction with NCS (chloronium source), which leads to a chlorinated product instead.

The step **F4-A1→F4-B1** is slightly more exergonic than the reaction with NBS (ΔG(**F4-A1→F4-B1**) = -8.1 kcal/mol while ΔG(**F3-A→F3-B**) = -2.3 kcal/mol). However, the activation barriers for these processes are nearly identical ($\Delta\Delta G^{\ddagger}$(**F3-TS$_{AB}$ - F4-TS$_{AB1}$**) = 0.6 kcal/mol). A similar transition state structure is obtained for the reaction of the methylated substrate with NBS (step **F4-A2→F4-B2**). This step is also fully concerted with the direct formation of a protonated cyclopropane intermediate, **F4-B2**. Although the conversion of a hydroxyl group to a methyl ether results in a slightly endergonic step (ΔG(**F4-A2→F4-B2**) = 0.4 kcal/mol), the activation barrier is still very close to the two transformations ($\Delta G^{\ddagger}$(**F4-A2→F4-B2**) = 14.4 kcal/mol).

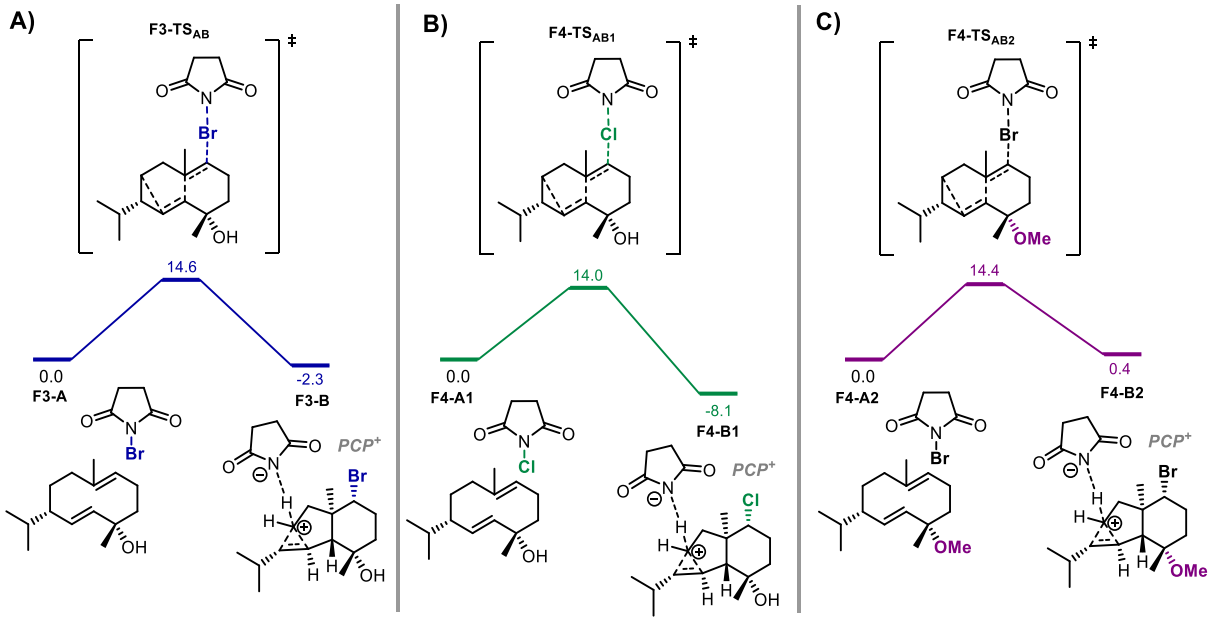

*Figure CCP-4 - Computed Gibbs free energy profile for the formation of the PCP+ intermediate: A) With NBS as electrophile; B) With NCS as electrophile; C) With NBS as an electrophile and a substrate containing methoxy group instead of hydroxy. The reactant complexes **F3-A**, **F4-A1** and **F4-A2** serve as a reference (0.0 kcal/mol) for each profile, and the explicitly included solvent molecule (DCM) was omitted from the scheme for clarity.*

It is worth noting that these three reactions yielded the desired cyclopropane product, and all three involve a concerted step for the formation of the protonated cyclopropane intermediate. The same was not observed when studying the mechanism for the reaction of **S8-1** with NIS and **S8-3** with NBS, which were experimentally unsuccessful. The obtained energy profiles for these two reactions, leading to the formation of the corresponding PCP+ intermediate, are presented in Figure CCP-5-A and Figure CCP-5-B, respectively.

The reaction of **S8-1** with NIS starts with the iodination of the most electrophilic double bond of **S8-1**. In this step, the I–C bond is formed while the I-N bond cleaves, leading to a tertiary carbocation intermediate **F5-B1**. The formation of this species is endergonic (ΔG(**F5-A1→F5-B1**) = 13.3 kcal/mol), and the thermodynamic instability of this species, even though it is a tertiary carbocation, might be the result of the steric clash of the methyl group and the large iodine atom. From this species, the reverse reaction leading back to the reactant complex **F5-A1** presents a smaller barrier than the formation of the *trans*-annular C–C bond that yields intermediate **F5-C1** ($\Delta G^{\ddagger}$(**F5-B1→F5-A1**) = 4.3 kcal/mol while $\Delta G^{\ddagger}$(**F5-B1→F5-C1**) = 6.7 kcal/mol). The former step is exergonic (ΔG(**F5-B1→F5-C1**) = -7.6 kcal/mol) and is followed by a last C–C bond formation that yields the protonated cyclopropane intermediate **F5-D1**. This last step presents a lower barrier than the reverse reaction back to intermediate **F5-B1** ($\Delta\Delta G^{\ddagger}$(**F5-TS$_{CD1}$ – F5-TS$_{BC1}$**) = -1.9 kcal/mol) and should therefore proceed towards the formation of the cyclopropane product. Although the overall formation of the PCP+ intermediate **F5-D1** is thermodynamically unfavorable (ΔG(**F5-A1→F5-D1**) = 11.8 kcal/mol), it is expected that a deprotonation event from the PCP+ structure will be highly exergonic. Additionally, it will occur with a very low activation barrier, in similarity to step **F3-B→F3-C** (Figure CCP-3-A).

For the reaction of **S8-3** with NBS, an initial step with the bromination of the double bond was observed, concerted with the formation of the *trans*-annular C–C bond (Figure CCP-5-B). This first step presents an activation barrier close to the one obtained for the first step of the reaction of **S8-1** with NBS ($\Delta G^{\ddagger}$(**F5-A2→F5-C2**) = 15.0 kcal/mol while $\Delta G^{\ddagger}$(**F3-A→F3-B**) = 14.6 kcal/mol (Figure CCP-3-A). The formation of the secondary carbocation intermediate **F5-C2** is slightly endergonic ($\Delta G^{\ddagger}$(**F5-A2→F5-C2**) = 2.4 kcal/mol). The stabilization of this intermediate is likely due to the decrease in the Thorpe-Ingold effect from the removal of the isopropyl group, giving more flexibility to the system. The final step is a facile stabilization of the cationic charge, which yields the PCP+ intermediate **F5-D2** ($\Delta G^{\ddagger}$(**F5-C2→F5-D2**) = 6.3 kcal/mol). The overall formation of this intermediate is slightly endergonic (ΔG(**F5-A2→F5-D2**) = 3.2 kcal/mol), which shows that additional flexibility of the cyclodecene ring resulting from the removal of one hydroxy and two methyl groups does not seem to benefit the cationic cyclopropanation reaction. Curiously, both these reactions present a stepwise mechanism for the

formation of PCP+ intermediate and failed to yield the cyclopropane product experimentally. This is in contrast to the profiles presented in Figure CCP-4: a single step for the formation of the PCP+ intermediate matching a successful cationic cyclopropanation reaction.

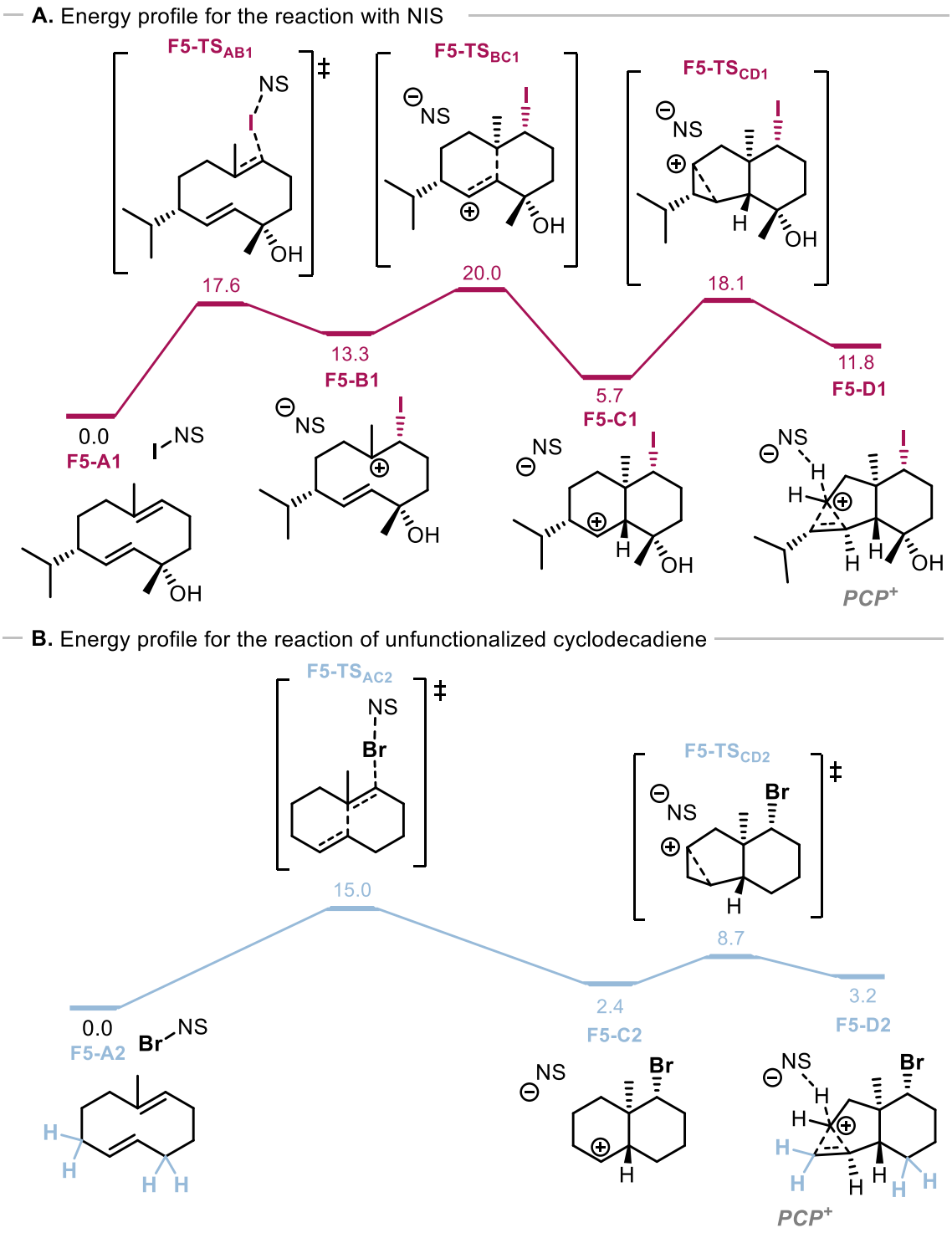

Figure CCP-5 – Computed Gibbs free energy profile for the formation of the PCP+ intermediate: A) With NIS as electrophile; B) With NBS as an electrophile and a cyclodecadiene substrate devoid of substituent groups The

*reactant complexes **F5-A1** and **F5-A2** serve as a reference (0.0 kcal/mol) for each profile and the explicitly included solvent molecule (DCM) was omitted from the scheme for clarity.*

At this point, it becomes clear that different substrates and halonium sources can affect the overall mechanism of the reaction, which can be broken down into elementary steps (Scheme CCP-9). In total, the formation of the cyclopropane product involves the halogenation of the double bond, the formation of a *trans*-annular C–C bond, the intramolecular stabilization leading to the formation of the PCP+ intermediate, and finally, a deprotonation of the PCP+. The obtained results show, on the one hand, that the PCP+ is crucial for the cyclopropanation reaction and, on the other, that its formation needs to occur in a single step for the cationic cyclopropanation reaction to be successful experimentally. It can also be envisioned that a stepwise mechanism results in the transient formation of highly unstable carbocationic species that can undergo hydride shifts and elimination reactions, leading to many undesired olefine side products. It is also worth considering that the formation of carbocation intermediates allows the occurrence of hydride shifts, which lead to charge relocation, ultimately increasing the amount of possible alkene products. Therefore, if the first three steps are concerted, the probability of deprotonation from a PCP+ increases, and a cyclopropane product can be obtained.

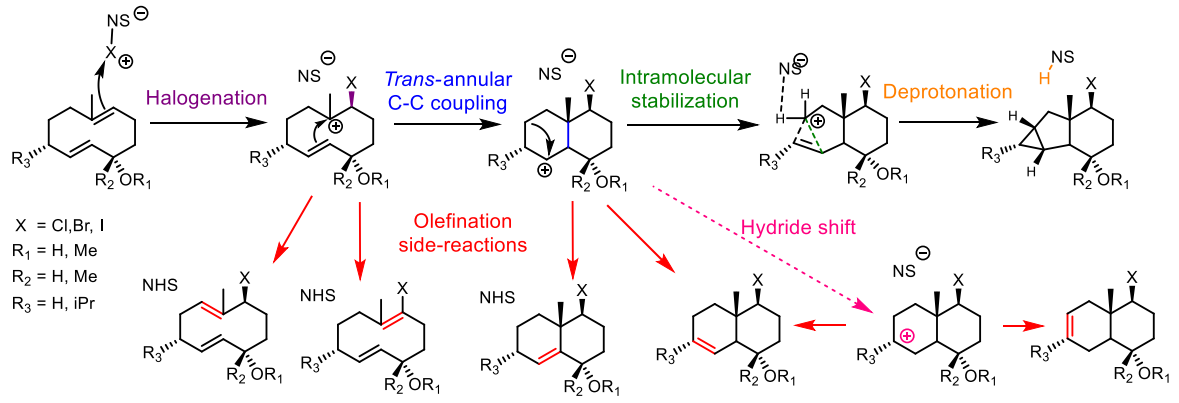

Scheme CCP-9 – Schematic representation of the elementary steps involved in the formation of the cyclopropane ring and the competing elimination pathways that would lead to undesired alkene byproduct.

Considering the importance of a concerted step for the formation of the PCP+ intermediate, this transformation was studied computationally by substituting functional groups in position 8 of **S8-1**, bearing initially Me and OH groups. The geometry of the obtained transition states was evaluated, and selected distances are presented in Figure CCP-6-A. These distances correspond to three bonds that are formed: the *trans*-annular C–C bond (D_1, in purple), the C–Br bond (D_3, in green) and the C–C bond

that is established to generate the protonated cyclopropane moiety (D_4, in yellow). Additionally, the distance at which the N–Br bond is cleaved is represented (D_2, in blue). This N–Br bond needs to be elongated until it cleaves to reach the transition state structure. Thus, earlier transition states present smaller values for D_2 and are consequently associated with a kinetically favored process. The opposite is expected for the bonds that are being formed. Since a more facile reaction step is achieved with a smaller distortion of the structure of the reactant complex, longer values for D_1, D_3 and D_4 correspond to an earlier transition state.

For this approach, both hydrogen and methyl were considered as functional groups in the equatorial position, R_{eq}. For the axial position, R_{ax}, hydrogen, hydroxy, phenyl, methoxy and methyl were chosen as substituents.

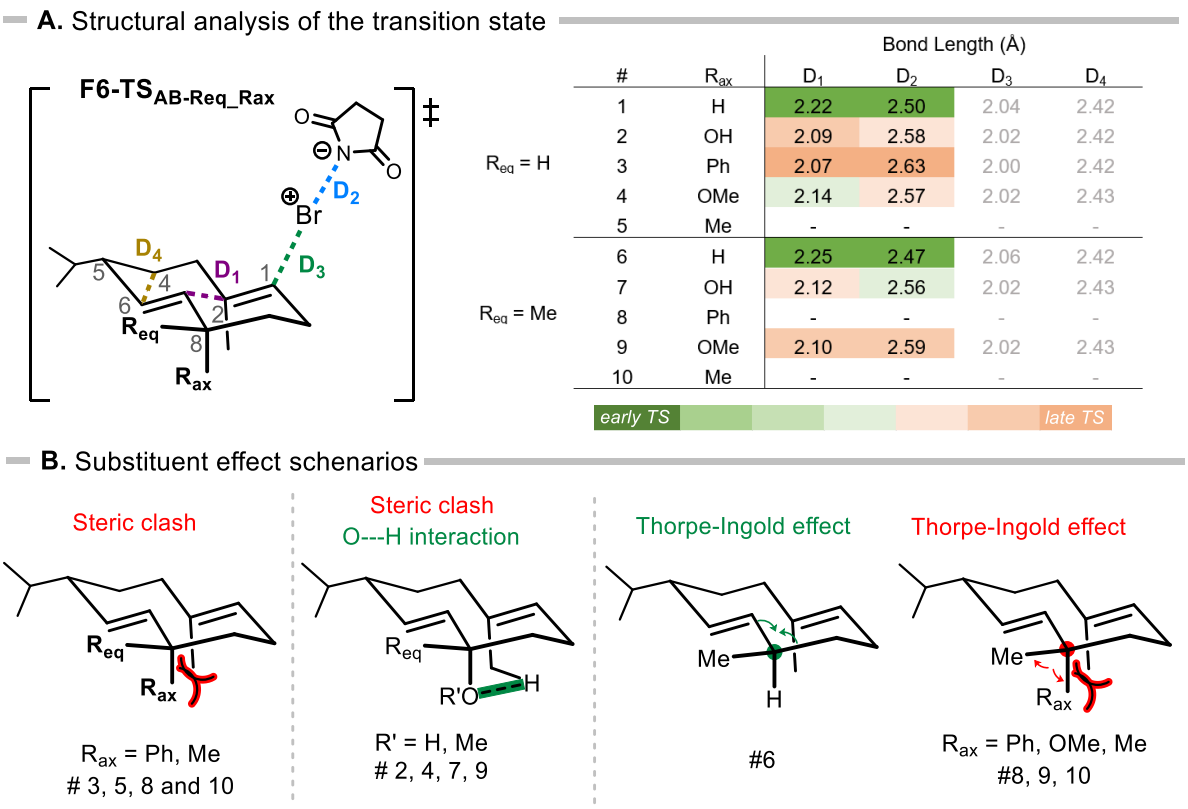

Figure CCP-6 – A) Selected geometric parameters of the concerted transition state structures leading to the formation of the protonated cyclopropane with different computed cyclic diene substrates; B) Schematic representation of the key factors affecting the favourability of the transformation.

Several attempts were made to obtain a concerted transition state for the reaction with a methyl group in the axial position (entries 5 and 10 of the table in Figure CCP-6-A), but all were unsuccessful and no

energy profile was obtained. For entry 8, corresponding to a methyl substituent in the equatorial position and a phenyl in the axial position, a non-concerted energy profile was obtained, which is then expected to result in an unsuccessful transformation experimentally.

For the remainder of entries, the obtained results show minimal variation in D_3 (interval of 2.02 to 2.06 Å) and D_4 (interval of 2.42 to 2.43 Å) with respect to the studied substituent group changes. A notable difference can, however, be observed for distances D_1 and D_2. The worst candidate is the substrate containing hydrogen and phenyl groups (entry 3), presenting the longest distance at which the N–Br bond cleaves, D_2 (2.63 Å), and the shortest distance required for the *trans*-annular C–C bond to be formed, D_1 (2.07 Å). Entry 7, with methyl and hydroxy, and entry 9, with methyl and methoxy substituents, correspond to successful transformations (Scheme CCP-8-A). From these two, the transition state structure of entry 9 appears to be the least favourable and also corresponds to a slightly lower observed yield of the reaction. The geometric parameters of entry 9 can potentially be used as a "minimum requirement", suggesting that other functionalizations of the studied scaffold that result in a concerted step with shorter D_2 and longer D_1 should lead to successful cationic cyclopropanation reactions, as is the case of entry 1, 2 and 6.

The obtained results for the substituent effect can then be rationalized by their contribution to the proximity of the two double bonds that form the *trans*-annular C–C bond (Figure CCP-6-B). A bulky group in the axial position generates a significant steric clash with the methyl group of the double bond that is being brominated. This clash can even impede a concerted pathway for the PCP+ formation. However, if the group in the axial position contains an oxygen atom (hydroxy or methoxy), an intermolecular O-H interaction can counter the steric clash, bringing the double bonds closer together. The substitution of the equatorial position imposes TI effect that can be beneficial if the axial position contains only a hydrogen atom, as the double bonds can be pushed closer to each other. However, if the axial position contains a bulky group, the steric clash to the methyl group on the opposite side of the ring becomes intensified, as can be observed by the difference between entries 4 and 9 (the first being more favorable and containing H in the equatorial position).

The very best candidate to be attempted experimentally is entry 6. However, due to the chirality imposed by the methyl group, the synthesis of the corresponding substrate becomes challenging. As an alternative, the transformation of entry 1 was attempted (Scheme CCP-10). As predicted, the reaction of **S10-1** with both NBS and NCS gave the desired cyclopropane-containing product in 36 % yield (Scheme CCP-10-A). Even though the obtained yield is modest, it is compensated by the achieved direct synthesis of products with high complexity and a challenging cyclopropane moiety. The transformation was also successful with other electrophiles, such as *N*-(phenylseleno) phthalimide, which promoted the electrophilic addition of phenyl selenium, and *meta*-chloroperoxybenzoic acid (*m*CPBA) with subsequent treatment with pivalic acid (PivOH), which promoted a hydroxylation of the double bond (Scheme CCP-10-B). These two reactions gave the desired cyclopropane product in even lower yield (roughly 14 %) but nonetheless highlight the ability of this scaffold to undergo a cationic cyclopropanation reaction through the formation of a PCP+ intermediate in a single step.

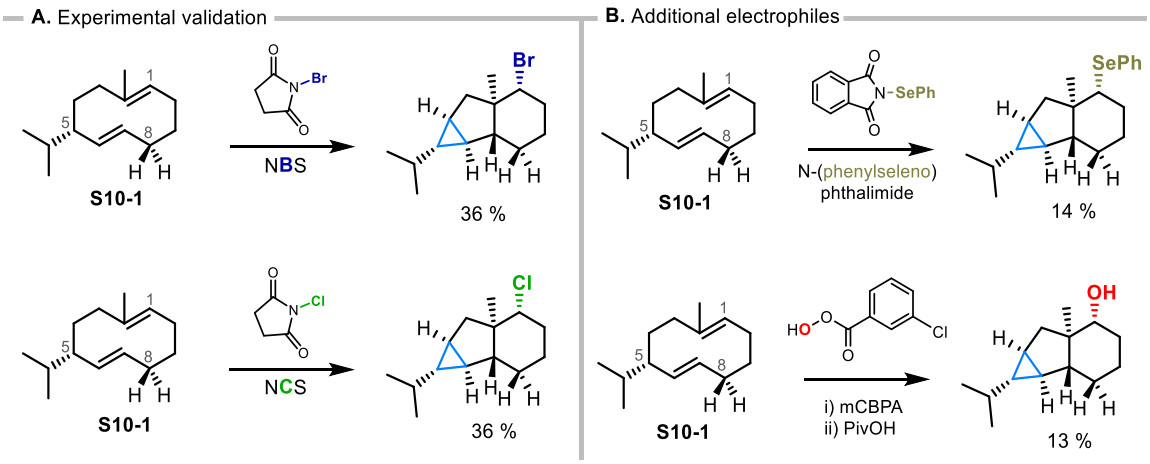

Scheme CCP-10 – A) Successful cationic cyclopropanation reactions performed following the computationally obtained insights; B) Experimental outcome of the use of the predicted substrate with additional electrophiles.

With experimental evidence that **S10-1**, which contains hydrogen atoms as substituents at position 8, can undergo a cationic cyclopropanation event, we decided to turn our attention to the substitution at position 5. It was already discussed that the reaction of **S8-3** with NBS (Scheme CCP-8-B) was not successful. This substrate also has hydrogens at position 8, as well as in position 5, where **S10-1** contains an isopropyl group. The importance of TI effect at position 5 was then investigated by computing an

energy profile for the PCP+ formation without substituents (Figure CCP-7-A) and with a methyl substituent (Figure CCP-7-B).

The cationic cyclopropanation mechanism for the substrate without a substituent in position 5, **F7-1A**, involves the formation of the secondary carbocation intermediate **F7-1B**, which can then be converted into the PCP+ intermediate **F7-1C**. This stepwise process presents a moderate overall activation barrier ($\Delta G^{\ddagger}$(**F7-1A→F7-1C**) = 15.4 kcal/mol) and is exergonic (ΔG(**F7-1A→F7-1C**) = -2.7 kcal/mol). Even though the second step, **F7-1B→F7-1C**, presents a very low activation barrier ($\Delta G^{\ddagger}$(**F7-1B→F7-1C**) = 1.4 kcal/mol), the stabilization of a secondary carbocation intermediate can lead to undesired olefination side reactions. The same is not observed if a methyl group is placed in position 5 (**F7-2A**), resulting in a fully concerted step for the formation of the PCP+ intermediate **F7-2B**. This transformation is similar to the one observed if an isopropyl group is in position 5, as discussed previously (Figure CCP-3-A). These results suggest that although a TI effect is crucial in this position, only a minimal contribution is required.

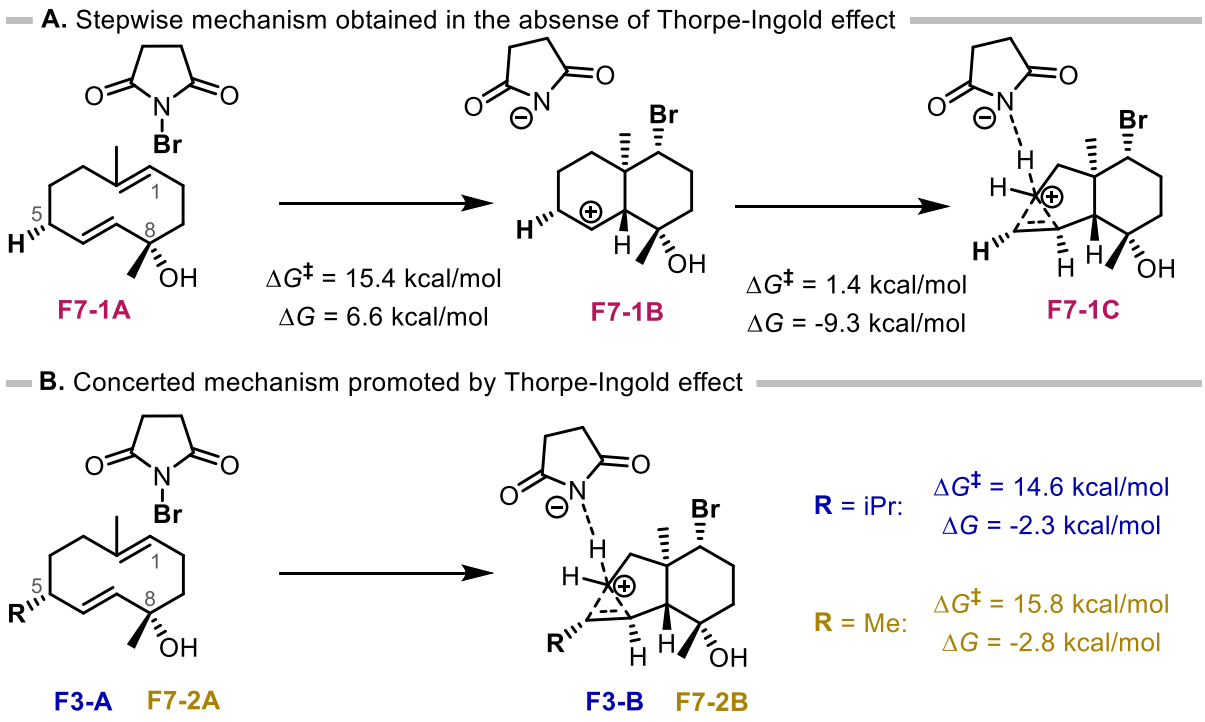

Figure CCP-7 – Verification of the TI effect in the formation of the PCP+ intermediate: A) Substrate involving a stepwise transformation; B) Substrates resulting in fully concerted steps.

4.4. Screening of potential substrates

The computational approach used thus far was employed to predict whether additional scaffold modifications would translate to successful cyclopropanation reactions. To this end, the possibility of a concerted step for the PCP+ intermediate formation was considered, with potential substrates featuring a disconnection of the decadiene ring, which would, therefore, result in a cyclopropanation reaction from a linear diene.

A disconnection between the carbons at position 4 and 2 was initially studied (Figure CCP-8-A). Taking methyl as both the substituent groups at position 5, the two double bonds of the diene substrate can potentially be either *cis*- or *trans*-configured. The energy profiles for the reaction of the three linear dienes with NBS were studied computationally (Figure CCP-8-B). For substrate **F8-1A**, *trans,trans*-configured, the reaction with NBS yields the protonated cyclopropane intermediate **F8-1B** in a single, concerted step (ΔG(**F8-1A→F8-1B**) = 0.6 kcal/mol). In this intermediate, the PCP+ fragment and the methyl substituent at position 2 are *anti*- to each other. A similar trend is observed with the *cis,trans*-substrate **F8-2A**, which also leads to the PCP+ intermediate **F8-2B** in a single step (ΔG(**F8-2A→F8-2B**) = 3.3 kcal/mol). This reaction is slightly less exergonic than **F8-1A→F8-1B,** possibly due to the PCP+ fragment and the methyl substituent at position 2 lying *syn*- to each other. Curiously, the reaction of NBS with the substrate **F8-3A**, presenting the *trans,cis*-configured double bonds, leads to the formation of a thermodynamically unstable classical secondary carbocation intermediate **F8-3B** (ΔG(**F8-3A→F8-3B**) = 21.0 kcal/mol), where the cationic fragment and the methyl substituent at position 2 are *anti*- to each other. While a rearrangement of **F8-3B** would lead to the formation of a PCP+ intermediate equivalent to **F8-1B**, the formation of a secondary carbocation intermediate along the reaction mechanism would likely lead to undesired elimination reactions. The stabilization of **F8-3B**, allowing this structure to be obtained as a minimum of energy, is likely due to the minimal steric repulsion between the methyl group of position 2 and the carbon at position 5 together with its substituents, which also reduces the activation of this step in comparison to the two previous cyclizations. Nonetheless, the obtained activation barriers for these three steps are impedingly high

($\Delta G^{\ddagger}$(**F8-1A→F8-1B**) = 30.2 kcal/mol, $\Delta G^{\ddagger}$(**F8-2A→F8-2B**) = 28.2 kcal/mol and $\Delta G^{\ddagger}$(**F8-3A→F8-3B**) = 27.0 kcal/mol).

The influence of two bulkier groups was also investigated with this approach (Figure CCP-8-C). The introduction of a benzyl group in the *trans,trans*-diene **F8-4A**, results in the unstable secondary carbocation intermediate **F8-4B** from the reaction with NBS (ΔG(**F8-4A→F8-4B**) = 20.2 kcal/mol). The increased steric bulkiness limits the conformational space of the system, as the C_5–C_6 bond can no longer freely rotate and likely hinders the formation of the PCP+ moiety. However, if a phenyl group is introduced into the system, **F8-5A**, a cyclopropane product, **F8-5B**, is formed promptly. A PCP+ intermediate was not obtained, likely due to the influence of the phenyl ring, which increases the acidity of a potential PCP+ intermediate (ΔG(**F8-5A→F8-5B**) = -61.9 kcal/mol). The high thermodynamic stability of **F8-5B** highlights the acidity of PCP+ species, which irreversibly form cyclopropane products through deprotonation events. Once again, these studied steps present very high activation barriers ($\Delta G^{\ddagger}$(**F8-4A→F8-4B**) = 28.7 kcal/mol and $\Delta G^{\ddagger}$(**F8-5A→F8-5B**) = 30.6 kcal/mol), strongly suggesting that cationic cyclopropanation from linear dienes is not plausible. It was shown recently that the decrease in *trans*-annular strain plays a major role in the thermodynamic feasibility of *trans*-annulation reactions. While in the reaction presented in Scheme CCP-7, a highly strained 10-membered ring collapses into three smaller, less strained rings (6-membered, 5-membered, and 3-membered), the same effect is not present if the diene substrate is linear.

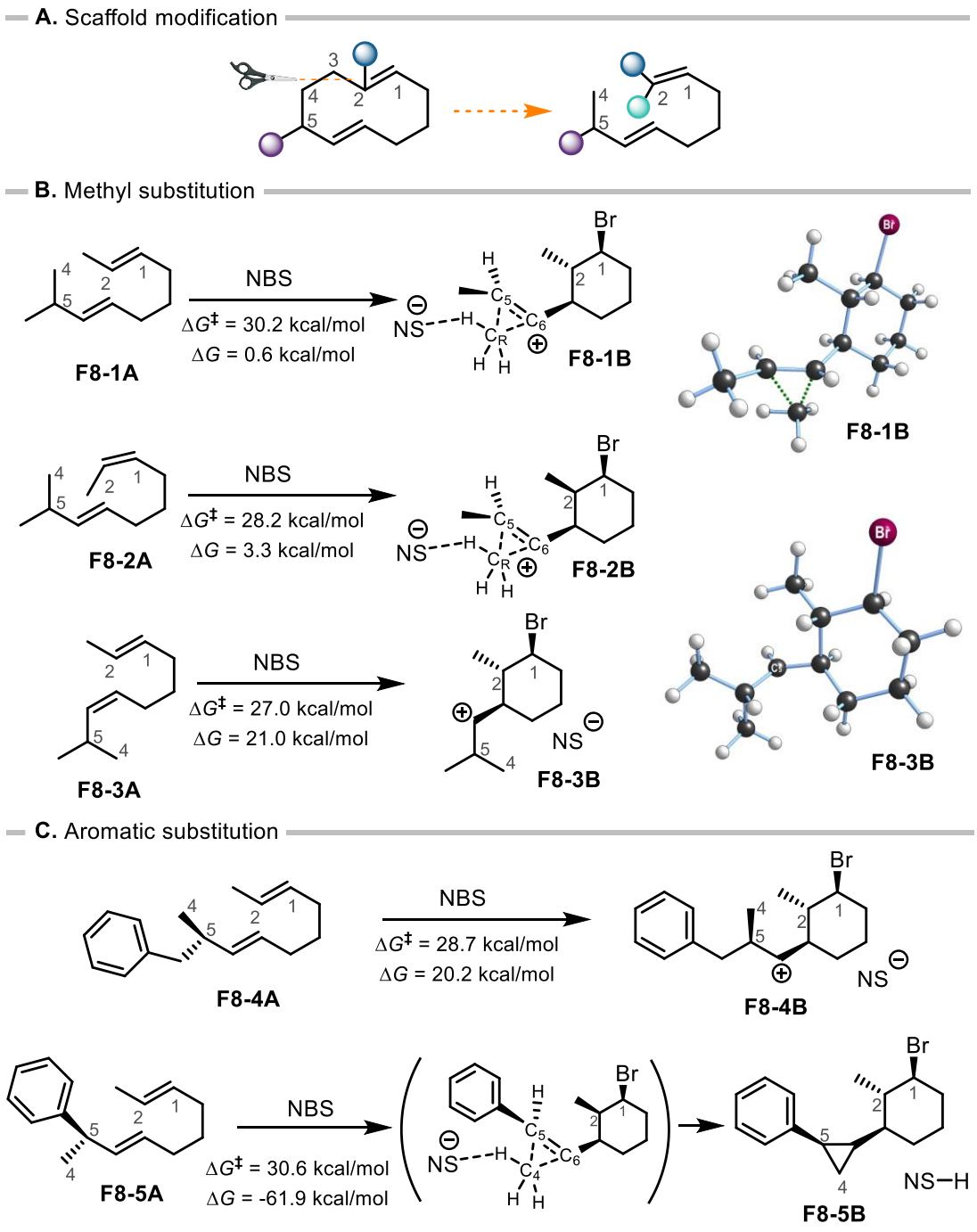

Figure CCP-8 – A) Representation of the attempted scaffold alterations; B) Thermodynamic data obtained for substrates with methyl substituents; C) Thermodynamic data obtained with the introduction of aromatic substituent groups.

Finally, modifications on the opposite side of the decadiene ring were investigated. It was previously discussed that, as observed experimentally, a disconnection between positions 8 and 9 hinders the formation of a cyclopropane product (Scheme CCP-8-B, reaction of **S8-4**), and no further disconnections of the ring that would lead to linear diene substrates were studied. It was then considered the possibility

of implementing in position 9 a replacement by a heteroatom, addition of ester substituents, and also ring extensions (Figure CCP–9-A).

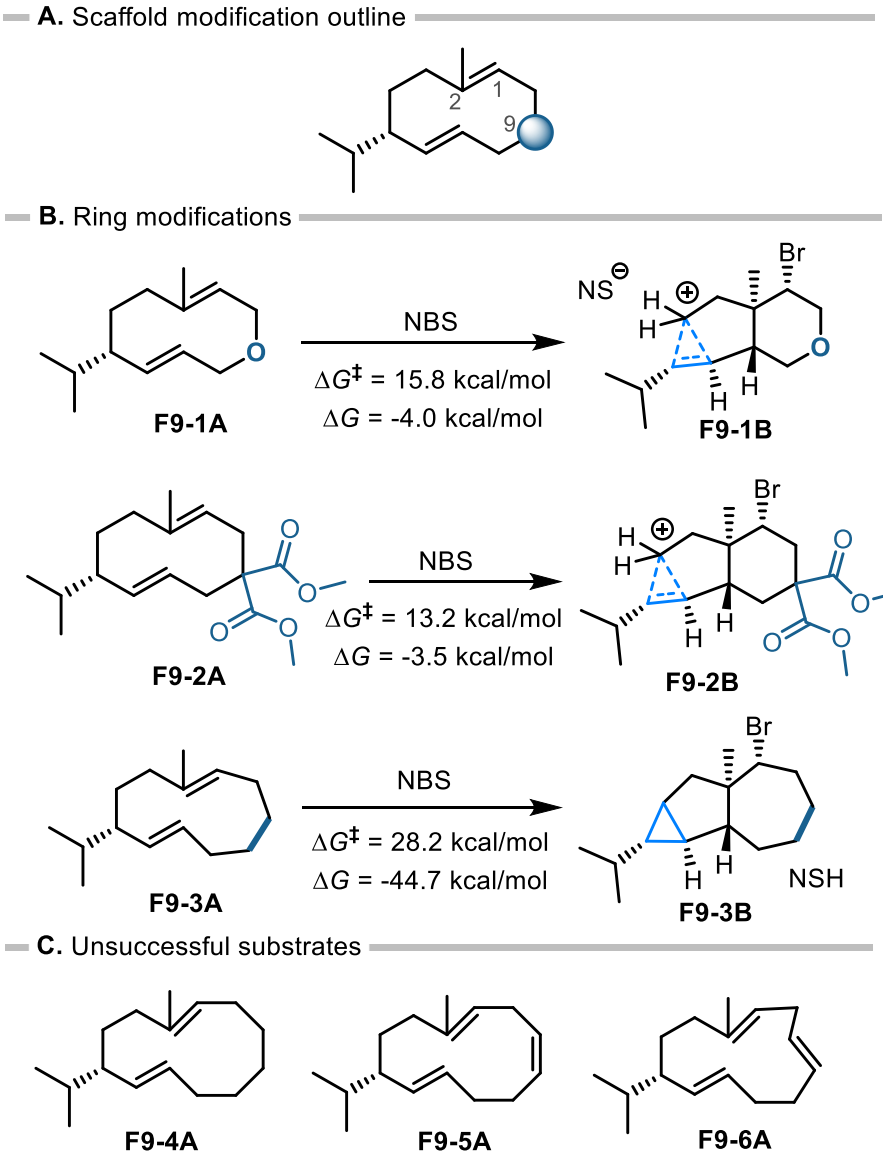

Figure CCP–9 – A) Representation of the attempted scaffold alterations; B) Thermodynamic data obtained for computed concerted steps; C) Substrates for which a single concerted step for the formation of a PCP+ was not obtained.

The introduction of an oxygen atom in position 9, **F9-1A**, does not affect the concertedness of the PCP+ intermediate formation, as a moderate activation barrier of 15.8 kcal/mol was computed for step **F9-1A→F7-1B**. The same concerted step for the PCP+ intermediate formation is observed if the TI effect is augmented through the introduction of a gem-diester substitution in position 9 (Angle(C-C_9-C)$_{F9\text{-}2A}$ = 114.6° while Angle(C-O_9-C)$_{F9\text{-}1A}$ = 116.2° and Angle(C-C_9-C)$_{F3\text{-}A}$ = 117.0°). Notably, it can be observed

a decrease in the activation barrier ($\Delta G^{\ddagger}$(**F9-2A→F7-2B**) = 13.2 kcal/mol, which is 2.6 kcal lower than $\Delta G^{\ddagger}$(**F9-1A→F7-1B**)). Both steps are exergonic (ΔG(**F9-1A→F7-1B**) = -4.0 kcal/mol and ΔG(**F9-2A→F7-2B**) = -3.5 kcal/mol). Therefore, it is expected that although there is a small facilitation of the cationic cyclopropanation process through the TI effect at position 9, its contribution is not crucial for the reaction outcome on cyclic substrates.

We, therefore, investigated the ring size expansion by one (**F9-3A**) and two carbons (**F9-4A**) and also the rigidification of an 11-membered ring with the introduction of an additional desaturation with either *Z*- or *E*- configuration, leading to potential cyclic undecatriene substrates (**F9-5A** and **F9-6A**). The reaction of **F9-3A** with NBS presents an impedingly high activation barrier ($\Delta G^{\ddagger}$(**F9-3A→F7-3B**) = 28.2 kcal/mol). The additional carbon in the ring would lead to the formation of a PCP+ intermediate, which would contain 3-, 5- and 7-membered rings. Due to the conformational constriction of the 7-membered ring, we were unable to optimize a stable PCP+ intermediate. Only the cyclopropane product together with the protonated succinimide was obtained (**F9-3B**), which resulted in a very exergonic step (ΔG(**F9-3A→F7-3B**) = -44.7 kcal/mol), similarly to the sequence of steps **F3-A→F3-B→F3-C** (Figure CCP-3-A). We were unable to find transition state structures for the equivalent reaction with a larger ring (12-membered cyclic diene **F9-4A**) and with 11-membered cyclic trienes (**F9-5A** and **F9-6A**), most likely due to a very high activation barrier associated to these processes.

4.5. Conclusions and outlook

This chapter explored the mechanism of cationic C-H functionalization that leads to cyclopropanation products, focusing on the reaction of cyclodecadiene with an electrophile to form 6,8-cycloeudesmane derivatives. A nonclassical carbocation species, the protonated cyclopropane, was identified as the pivotal intermediate in this process.

Our computational analysis demonstrated that the cyclopropanation reaction for a given cyclodecadiene substrate is only feasible if the mechanism involves a single, concerted step to form the protonated cyclopropane intermediate. We discovered that even though some stepwise processes may appear kinetically and thermodynamically favorable, they are inefficient due to the high probability of side

reactions at each step. Consequently, we propose using a "concertedness degree verification" approach to guide the development of these cyclopropanation reactions.

By applying this approach, we screened the impact of various functional groups to predict new substrates that would likely yield successful reactions. Our predictions were experimentally validated, confirming the effectiveness of our method.

With this validated method in hand, we extended our investigations to novel scaffolds to assess the potential for cyclopropanation reactions. We advocate that future experimental work should be preceded by computational screening using our approach, enabling the avoidance of reactions that are thermodynamically or kinetically implausible.

5. Chapter III: Hydrogen atom transfer in alkylation of polyols

The following results have been partially published in a peer-review journal.[107] The computational investigation of an CO_2 mediated C-H alkylation reaction is described in this chapter.

5.1. C-H alkylation

The constant need to reduce the usage of fossil resources is a major challenge of modern organic synthesis, leading to the development of new processes that utilize alternative feedstocks and innovate classical functionalization strategies. In this setting, symmetric light polyols constitute attractive carbon sources, offering all at once a broad structural diversity and a range of scaffolds stemming from biomass.[108–110] Moreover, their unique pattern characterized by the iteration of hydroxyl functions offers an extensive synthetic potential. Indeed, the direct consequence of this structural property is a leap in molecular complexity when a single alcohol is selectively modified. Among the considered transformations, the catalytic α-C-H alkylation at one site of unprotected acyclic diols and triols constitutes an appealing way to access valuable building blocks quickly. Alkylation reactions are processes by which an alkyl group is attached to an organic substrate molecule via addition or substitution. These processes are highly dependent on the activation of C-H bonds. Thus, the development of efficient processes that can promote this transformation is of great interest.

An efficient approach to promote C-H activation of alcohols is through hydrogen atom transfer (HAT) reactions. These occur through the homolytic cleavage of α-C-H bonds. One major advantage of this method is the selectivity towards C-H activation, while the O-H bond of the hydroxyl group is not affected. The recent development of visible-light photocatalysis techniques has led to the development of powerful methods to achieve the direct α-C-H alkylation of alcohols through catalytic hydrogen atom transfer (HAT) and ketyl radical addition sequences Scheme HAT-1.[111,112]

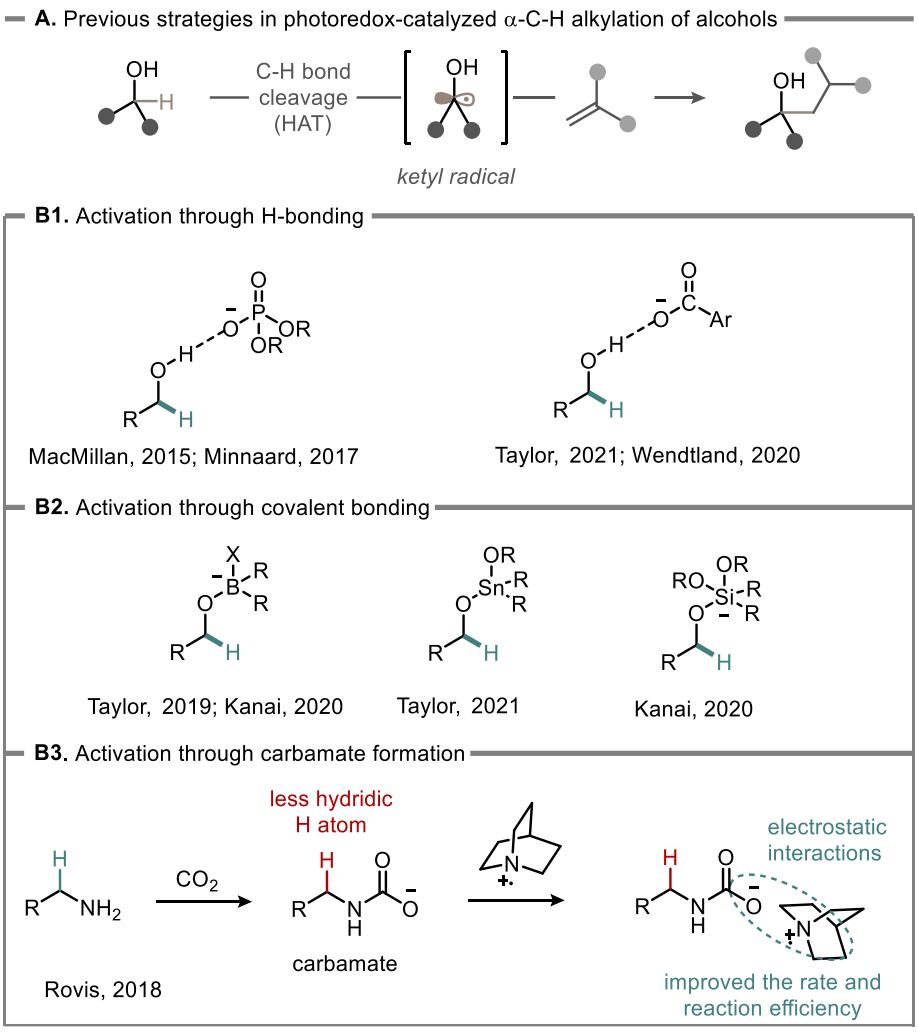

Scheme HAT-1 – A) Representation of a general approach for alkylation of alcohol in photocatalysis stetting; B) Reported methods of C-H activation towards homolytic cleavage of the C-H bond.

Several strategies have been developed with the goal of facilitating the homolytic cleavage of the α-C–H bond of alcohol. For instance, strong but unselective HAT catalysts were reported to catalyze the α-C-H alkylation of simple aliphatic alcohols.[113] Alternatively, the use of H-bonding acceptors (Scheme HAT-1-B1) or Lewis acid (LA) catalysts (Scheme HAT-1-B2) emerged as a powerful approach to increase the efficiency of the photocatalyzed C-H activation of alcohols. Both these interactions result in the increase in electron density of the α-H atom, increasing its hydridic character, which in turn facilitates the homolytic cleavage of the C–H bond. This ability of H-bond acceptors and LA to interact with hydroxyl groups displaying specific orientations has been the source of major advances in site-selective photoredox-catalyzed α-C-H alkylations of alcohols. These processes have been recently developed through ternary catalytic systems[114,115] involving a photoredox catalyst, a cationic HAT

promotor and a H-bond acceptor or LA catalyst.[116,117] Such approaches have also been attempted with polyols, which are chemical compounds containing multiple hydroxyl groups. Although polyols are a cheap and highly abundant chemical resource, the presence of additional OH groups often imposes a problem of selectivity in chemical transformations since multiple groups could react. This is especially the case for catalytic α-C-H alkylations of symmetric polyols, represented in Scheme HAT-2-A. The presence of multiple non-oriented α-C-H bonds in the substrate can result in the catalytic activation of the alkylated group, leading to the formation of undesired products of over-alkylation. Consequently, the development of a general strategy to achieve the photoredox-catalyzed α-C-H mono-alkylation of symmetric light polyols remains an important synthetic challenge.[118]

Recent work from Rovis and co-workers demonstrated that the use of CO_2 as reagent to form a carbamate intermediate that can enhance the efficiency of α-C-H alkylations of primary amines,[119] even though this transformation decreases the hydridic character of the α-H atom due to the electron-withdrawing nature of the carbamate group (Scheme HAT-1-B3). In this reported work, the authors proposed that the increased efficiency of the catalytic system is derived mainly from electrostatic interactions between the carbamate moiety and the quinuclidinium radical (HAT-promoting agent). These interactions keep the two species close to each other in the reaction media, allowing a faster inter-molecular HAT step.

5.2. Catalytic α-C-H alkylation of diols

In collaboration with the Merad group from the University of Lyon, we have studied the possibility of exploiting a reversible CO_2 incorporation to promote the α-C-H mono-alkylation of symmetric light polyols. A ternary catalytic system was then developed (Scheme HAT-2-B), allowing the conversion of symmetric diols, **S2-1**, and methyl acrylate, **S-2**, into hydroxy-functionalized cyclic lactones, **S2-3**. The employment of CO_2 as a HAT-directing group brings many advantages since this species is abundant, non-toxic and traceless.[119,120] However, the formation of carbonated species from the reaction of alcohols and CO_2 is not spontaneous and requires catalytic activation. To overcome the kinetic inertness of alcohols and CO_2, various amine catalysts were tested in association with HAT and photoredox catalysts. The association of carbonation catalyst DBN (1,5-diazabicyclo[4.3.0]non-5-ene) with Ir[(dF-

CF_3-ppy)$_2$dtbpy]PF_6 and quinuclidine was found as an optimal combination (Scheme HAT-2-A). It was also discovered that the alkylation of diol **S2-1** in the presence of methyl acrylate **S2-2** was further improved in aqueous acetonitrile solutions (CH_3CN:H_2O = 10:1), delivering mono-lactone **S2-3** in 86% NMR yield after only 30 minutes of blue LEDs irradiation (Scheme HAT-2-B, entry 1). The requirement of each parameter was confirmed by a set of control experiments shown in Scheme HAT-2-C. A dramatic drop in yield was observed by switching to an argon atmosphere (entry 2), highlighting the key role of CO_2 in the reaction. The same was observed in the absence of DBN (entry 3), quinuclidine (entry 4) and H_2O (entry 5). Moreover, proceeding without a photoredox catalyst (entry 6) or in the dark (entry 7) resulted in a complete shutdown of the reaction.

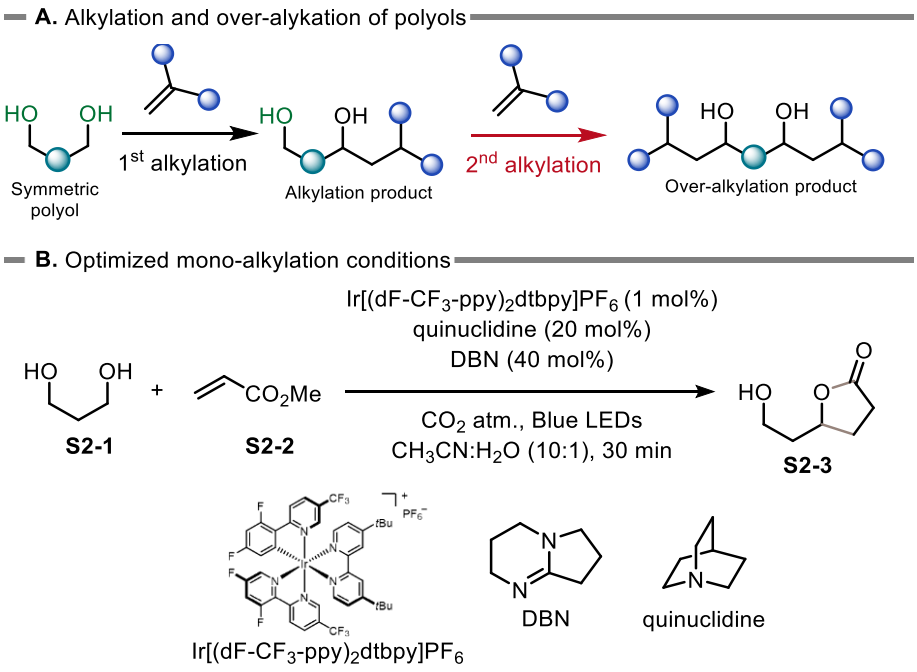

C. Control experiments

Entry	Deviation from standard conditions	Yield of **S2-3**
1	None	86%
2	Argon atmosphere instead of CO_2	15%
3	No DBN	13%
4	No quinuclidine	< 5%
5	No H_2O	21%
6	No Ir cat.	0%
7	No light	0%

Scheme HAT-2 – A) Representation of alkylation and over-alkylation events; B) Optimized experimental conditions for the mono-alkylation of symmetric diols; C) Performed experiments to test the influence of experimental additives and factors in the reaction outcome.

Following the mechanistic hypothesis proposed by Rovis and co-workers for CO_2 incorporation, a catalytic cycle for the ternary system presented in Scheme HAT-2-A is outlined in Scheme HAT-3. It was initially reasoned that after the interaction of DBN and CO_2 to form an activated DBN-CO_2 adduct, a reaction with the diol **S2-1** yields the monocarbonate intermediate **S3-A**. This step would result in the desymmetrization of the substrate under CO_2 atmosphere, distinguishing the reactivity of the targeted α-C-H bonds. Indeed, α-C-H bonds locally deactivated by the electron-deficient carbonate would then coexist with α-C-H bonds activated by an emerging intramolecular H-bonding. A site-selective HAT, promoted by the quinuclidinium radical **S3-Q** would lead to the radical intermediate **S3-B** and a quinuclidinium intermediate, which can be regenerated back to quinuclidine through the loss of a proton. A single electron transfer (SET) with the electronically excited photoredox catalyst, Ir(III)*, closes the quinuclidine cycle back to the quinuclidinium radical, **S3-Q**. It is worth noting that following the hypothesis of Rovis and co-workers, the HAT should occur from the α-H atom from the carbonated alcohol group (Scheme HAT-1-B3).

A C-C bond formation in the presence of the olefin **S2-2** forms the intermediate **S3-C**, from which a SET step mediated by the reduced photoredox catalyst, Ir(II), yields the di-anionic intermediate **S3-D**, regenerating the iridium (III) catalyst. Finally, through a protonation step, which is likely assisted by a water molecule (Scheme HAT-2-B, entry 5), a carbonated intermediate is able to cyclize into the observed monolactone product **S2-3** with the release of methanol and CO_2. In such catalytic systems, it is commonly observed that the rate-determining step is the HAT. Hence, the efficiency of the reaction is highly dependent on the initial activation of the substrate.

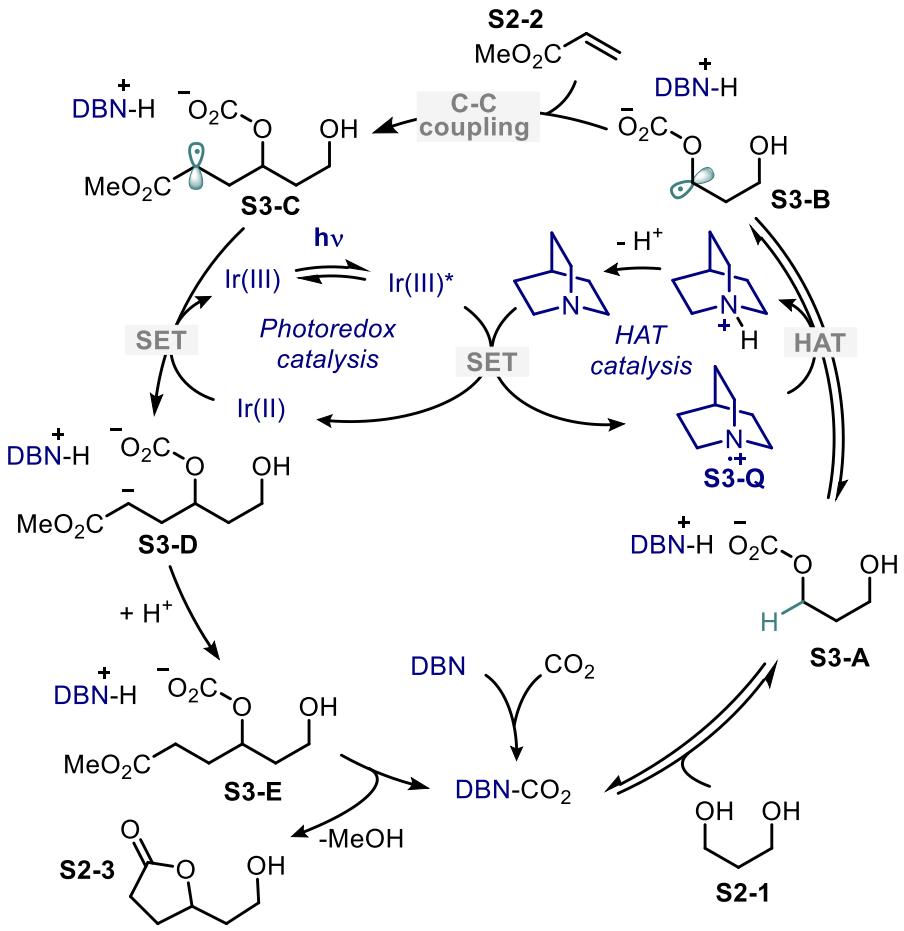

Scheme HAT-3 – Initially proposed mechanism for the ternary catalytic cycle of the alkylation reaction.

The developed ternary catalytic system (photoredox/HAT/carbonation) allows lactonization from several diols, both primary and secondary. Different olefins are also tolerated with the optimized reaction conditions (Scheme HAT-4). The conversion of 1,2- and 1,4-diols (leading to **S4-3b** and **S4-3c**) is tolerated, and increasing the steric shielding at the vicinity of the targeted C-H bond does not significantly affect the reactivity (**S4-3d** and **S4-3e**). A perfect chemoselectivity was observed for Boc-protected serinol (**S4-3f**) and 2-benzylpropane-1,3-diol (**S4-3g**), highlighting the carbonation-induced kinetic activation. Secondary alcohols proved to be even more efficiently alkylated, yielding the corresponding lactones **S4-3h** and **S4-3i** with good yields, even in the presence of a single equivalent of diol (**S4-3h**). Interestingly, the efficiency and stereoselectivity of the reaction proved to be independent of the relative configuration of cyclic substrates. Indeed, cyclohexane-1,2-diol was alkylated with the same yield and diastereoselectivity starting from a *cis*/*trans* mixture or pure *cis* diastereomer (**S4-3j**). This last result is of significant interest. If the HAT occurs from the α-H to the carbonated alcohol, there

should be a difference in the diastereoselectivity of *cis*- and *trans*- 1,2-hexanediol. The transposition of our conditions to the functionalization of triols displays the same exquisite selectivity for monoalkylation, and compound **S4-3k** was isolated in 69% yield. However, the alkylation of glycerol containing both primary and secondary alcohols proceeds without regioselectivity, resulting in a mixture of monolactones (**S4-3l**). The effect of chain length of the diol was also tested, resulting in a slight decrease in yield with larger chain lengths (**S4-3o**-**S4-3t**) until 53% with 1,10-diols. The mechanistic proposal presented by Rovis and co-workers is based on the carbonate group being able to keep the quinuclidinium radical in close proximity, allowing a faster C-H activation of the carbonated hydroxyl group. Assuming this hypothesis, the length of the alkyl chain of the diol should not affect the reaction outcome. However, the observed decrease in yield of the reaction with the increase in length of the alkyl chain brings to light inconsistencies with the initially proposed mechanism.

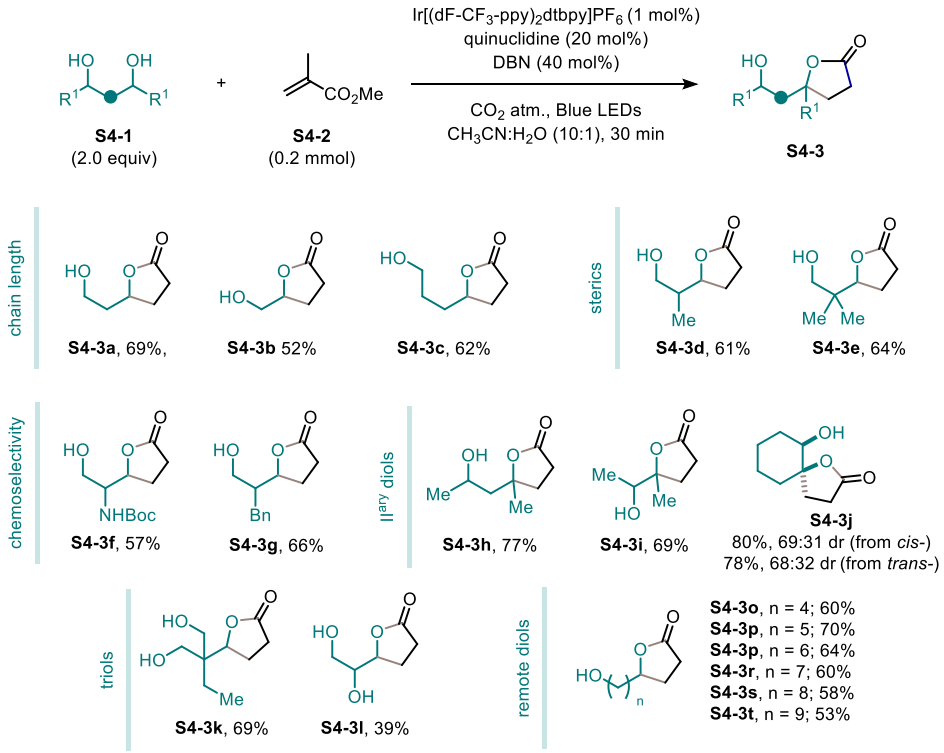

Scheme HAT-4 – Experimentally obtained substrate scope.

To shed further light on the C-H activation process occurring in our catalytic system, the carbonation reaction of 1,3-propanediol was studied with ^{1}H NMR techniques, as shown in Scheme HAT-5-A. An efficient approach to predict if a homolytic C-H bond cleavage is possible is by comparing the hydridic character of the hydrogen atoms. Hydridicity is a property of hydrogen atoms related to the polarity of

the C-H covalent bond. If the electron density of the C-H bond is more shifted towards the carbon, the hydrogen atom is less hydridic and will have a higher tendency towards a heterolytic bond cleavage instead (proton transfer). As a result, a higher hydridic character of a hydrogen atom corresponds to a higher propensity towards a HAT step. One of the best methods to study the hydricity of hydrogen atoms is through ^{1}H NMR spectra, as this property is directly related to the chemical shifts. The experimentally obtained chemical shift for the α-H atom of the diol is 3.56 ppm. After the first carbonation, it is possible to observe that the α-H atom to the alcohol becomes less shielded and, therefore, more hydridic (chemical shift of 3.49 ppm). In contrast, the α-H atom to the carbonated alcohol presents a higher chemical shift (3.89 ppm) and is, thus, significantly less hydridic. This assignment of chemical shifts was further confirmed from the characterization of the di-carbonated species, which presents both the α-H atoms with a chemical shift of 3.80 ppm. These results strongly indicate that the most hydridic hydrogen atom is in α-position to the hydroxy group, raising questions about the initially proposed mechanism of HAT activation in our system. Furthermore, the optimized conditions were also applied to a mixture of 1,3-propanediol and propanol (Scheme HAT-5-B), which showed that the C-H activation is significantly more effective for the diol. Again, following the initially proposed mechanism, both substrates would be expected to be activated in the same proportion.

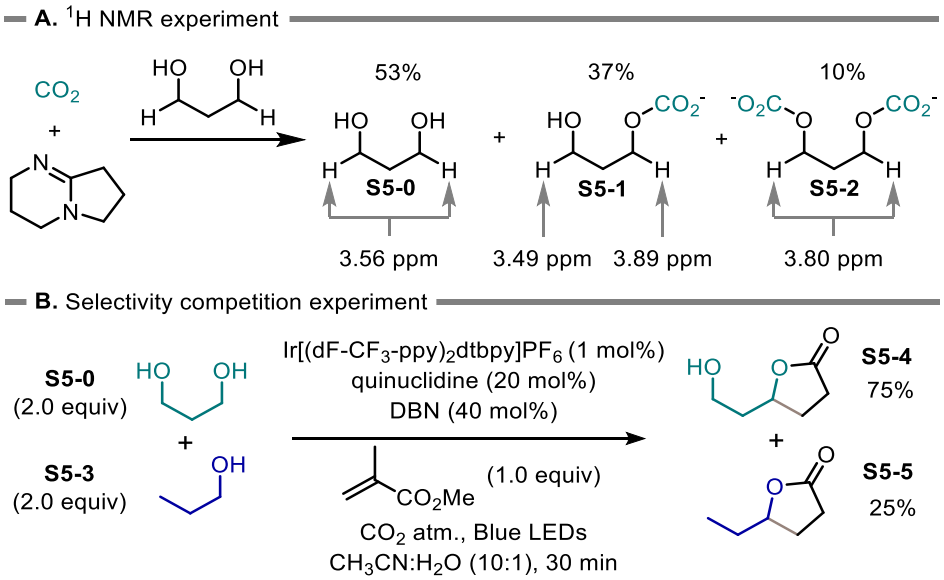

Scheme HAT-5 – Experimentally determined chemical shifts of diols with different degrees of carbonation.

It is worth noting that the presented ternary catalytic system is able to activate simple alcohols, such as propanol, even if the activation is less efficient than with diols. Therefore, it is unclear why the carbonation under CO_2 atmosphere enhances the rate of the reaction while, at the same time, turning the α-H atom less hydridic.

5.3. *In silico* investigation of α-C-H activation factors

To clarify the C-H activation mechanism in this catalytic system, the HAT step of this reaction was computationally investigated at the ωB97X-D(SMD,ACN)/def2-TZVP//ωB97X-D(SMD, ACN)/def2-SVP level of theory. At the first stage, the Δ*H* of the homolytic C-H bond cleavage was investigated in order to understand if the HAT occurrence from the less hydridic α-H atom to the carbonate would be enthalpically favorable. To this end, a relative ΔΔ*H* calculation method, namely the isodesmic reaction approach,[52,121] can be employed (Scheme HAT-6). The Δ*H* of reaction **A** (ΔH_A) can be computed by subtracting the enthalpy of the alcohol **1** (H_1) from the sum of the enthalpy of the two formed radicals from the homolytic C-H bond cleavage (equation 1). The same can be applied to reaction **B** (equation 2). At this point, the direct comparison of Δ*H* of reaction **A** with reaction **B** (equation 3) enables the calculation of relative enthalpies of homolytic C-H bond cleavage reactions without the need to compute the enthalpy of the hydrogen atom.

Reaction **A**

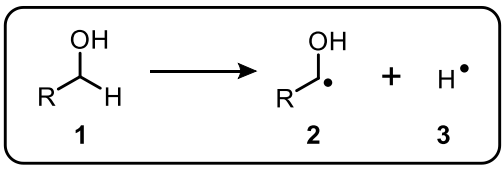

$$\Delta H_A = H_2 + H_3 - H_1 \qquad (1)$$

Reaction **B**

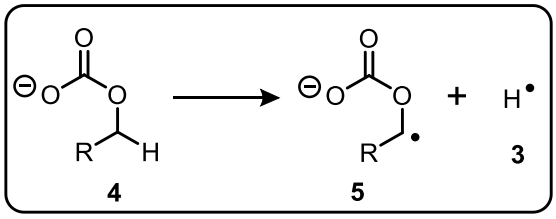

$$\Delta H_B = H_5 + H_3 - H_4 \qquad (2)$$

$$\Delta\Delta H_{AB} = \Delta H_B - \Delta H_A = H_5 + H_3 - H_4 - (H_2 + H_3 - H_1) = H_5 - H_4 - H_2 + H_1 \qquad (3)$$

Scheme HAT-6 – Isodesmic approach used to compute the enthalpy of the formation of the radical intermediates through a HAT event.

With this method, the homolytic cleavage of the α-H of 1,3-propanediol (F1-R0) can be taken as a reference (Figure HAT-1, left, top), and the relative Δ*H* of other systems can be computed. The reaction enthalpies were computed considering the formation of all the possible α-radicals from a 1,3-propanediol with (F1-R0') and without (F1-R0) the explicit inclusion of DBN, carbonated 1,3-propanediol with (F1-R1') and without (F1-R1) the explicit inclusion of protonated DBN (DBN-H^+) and also carboxylic acid again with (F1-R2') and without (F1-R2) the explicit inclusion of DBN in the model.

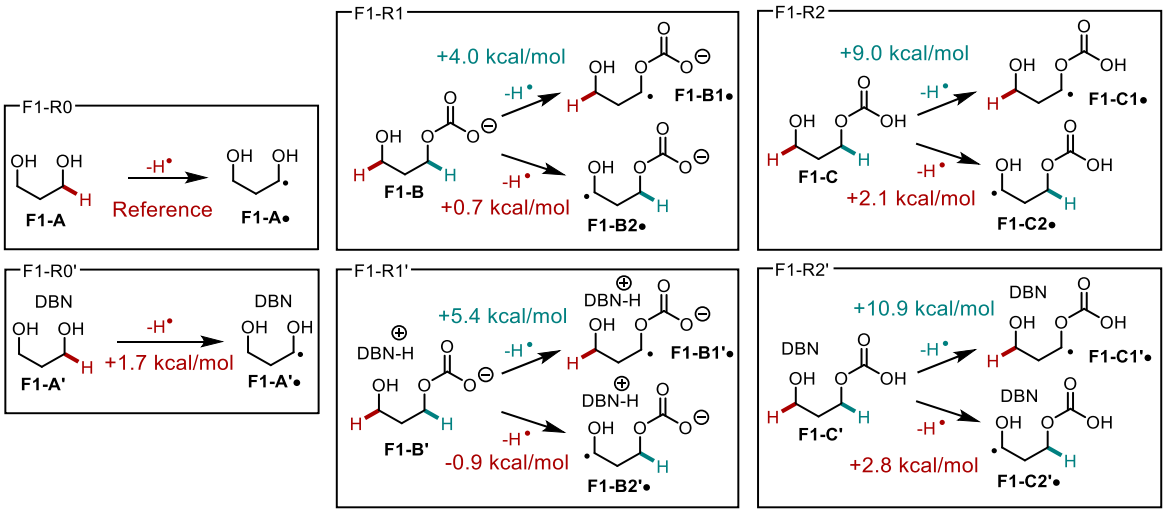

*Figure HAT-1 – Obtained results for the formation of radical intermediates through HAT. The enthalpy of the conversion of **F1-A** into **F1-A•** is taken as a reference, and all presented reaction enthalpy values are relative to this reference.*

The obtained results show that for carbonated diols (**F1-B** in F1-R1 and **F1-B'** in F1-R1'), the homolytic cleavage is enthalpically favored to occur from the α-H atom to the hydroxyl group (ΔΔ*H*(**F1-B→F1-B2•**) = 0.7 kcal/mol while ΔΔ*H*(**F1-B→F1-B1•**) = 4.0 kcal/mol and ΔΔ*H*(**F1-B'→F1-B2'•**) = -0.9 kcal/mol while ΔΔ*H*(**F1-B'→F1-B1'•**) = 5.4 kcal/mol). The inclusion of the protonated DBN species in the computational model enables the formation of an additional H-bond with the carbonate moiety, further stabilizing the radical species **F1-B2'•** and destabilizing the radical species **F1-B1'•**. As a result, the most enthalpically favorable homolytic C-H cleavage overall is step **F1-B'→F1-B2'•**, further supporting the experimental data obtained with ^{1}H NMR studies that characterized the abstracted hydrogen atom in this step as having the most hydridic character. If the carbonated diol becomes protonated by DBN-H^+, yielding **F1-C** in F1-R2 and **F1-C'** in **F1-R2'**, the

homolytic cleavage of the C-H bond becomes enthalpically disfavored when compared to the non-activated system (F1-R0). Finally, it is also possible to observe in F1-R0' that DBN alone is not likely to promote the activation of the HAT process through intermolecular H-bonding ($\Delta\Delta H($**F1-A'→F1-A'•**) = 1.7 kcal/mol).

In the originally proposed mechanism, it was considered that the α-hydrogen to the carbonated hydroxyl group would undergo an HAT event. However, these results highlight a discrepancy to the initial hypotheses as it is shown that the homolytic cleavage at this hydrogen atom is not favored. Therefore, the kinetics of the quinuclidinium radical-promoted HAT step was investigated for simple and carbonated alcohols as well as for 1,3- and mono-carbonated 1,3-diols (Figure HAT-2).

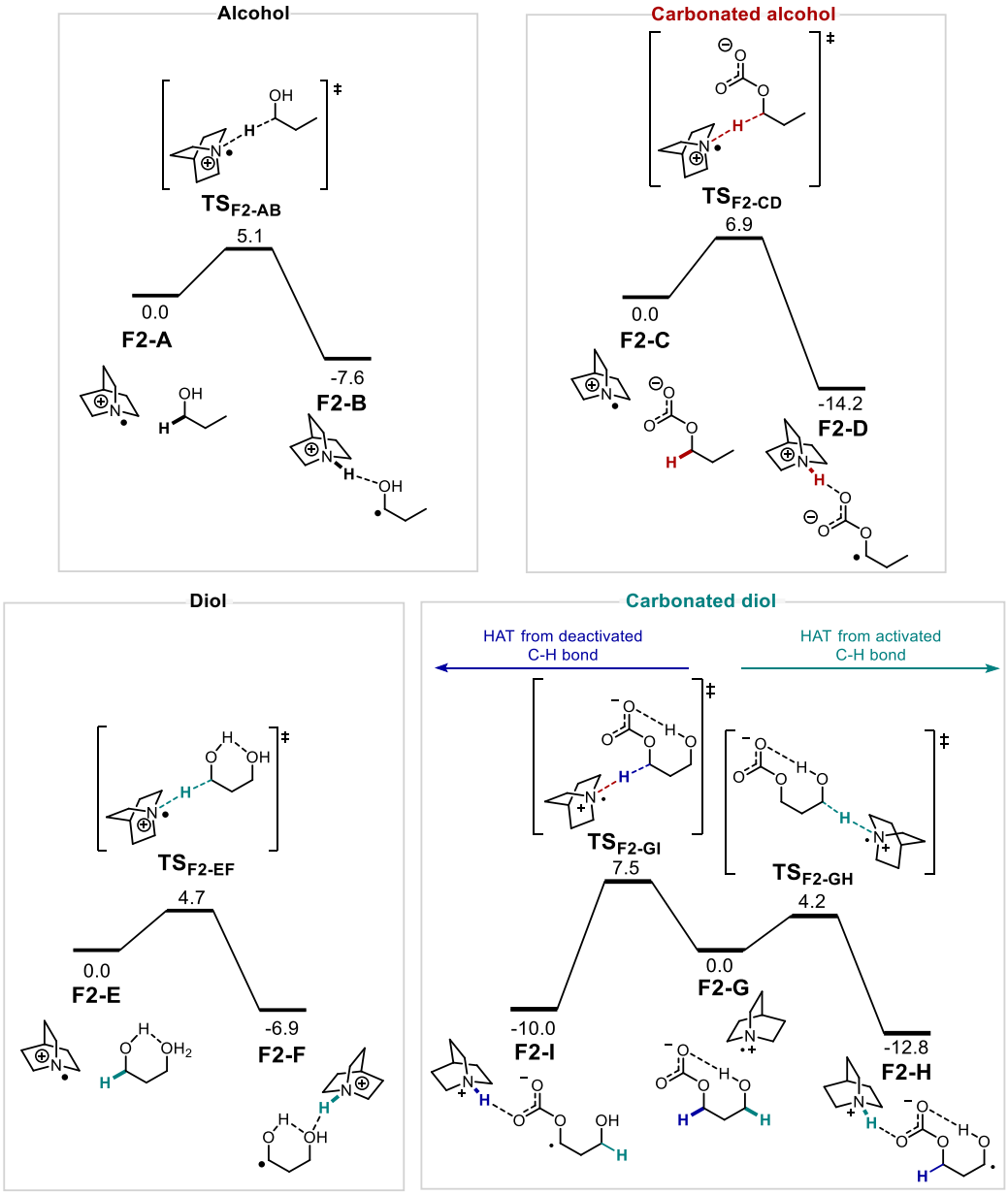

*Figure HAT-2 - Computed Gibbs free energy profile for the quinuclidinium promoted HAT from propanol (top left), carbonated propanol (top right), propanediol (bottom left) and carbonated propanediol (bottom right). The reactant complexes **F2-A**, **F2-C**, **F2-E** and **F2-G** serve as a reference (0.0 kcal/mol) for each profile.*

The reactant complex of propanol with quinuclidinium radical, **F2-A**, can undergo an α-HAT step to form the alkyl radical and quinuclidinium cation **F2-B** with an activation barrier of 5.1 kcal/mol (step **F2-A→F2-B**). This intermolecular reaction is computed to be exergonic (ΔG(**F2-A→F2-B**) = -7.6 kcal/mol), with a major driving force being the formation of a stable quinuclidinium cation, which is highlighted by the vast use of quinuclidine as a HAT catalyst. The intramolecular HAT from the carbonated propanol, step **F2-C→F2-D**, presents an activation barrier 1.8 kcal/mol higher than the HAT from propanol ($\Delta G^{\ddagger}$(**F2-A→F2-B**) = 6.9 kcal/mol). This result follows the previously obtained enthalpic

data, which shows that the HAT from the α-H atom to the carbonate is not favored. Notably, this transformation becomes significantly more exergonic from the carbonated alcohol (ΔG(**F2-C→F2-D**) = -14.2 kcal/mol) due to the stabilization of the radical by the carbonate moiety. The HAT from the diol, step **F2-E→F2-F**, presents a slightly lower activation barrier than the HAT from propanol: $\Delta G^{\ddagger}$(**F2-E→F2-F**) = 4.7 kcal/mol while $\Delta G^{\ddagger}$(**F2-A→F2-B**) = 5.1 kcal/mol. This lower barrier likely results from intramolecular hydrogen bonds established by the two hydroxyl groups. This step is also slightly less exergonic than step **F2-A→F2-B**, (ΔG(**F2-E→F2-F**) = -6.9 kcal/mol), possibly due to the interaction with the quinuclidinium cation, which interferes with the intramolecular H-bond established between the hydroxyl groups of **F2-F**. Finally, the mono-carbonated 1,3-propanediol **F2-G** can undergo α-HAT from the side of the hydroxy (step **F2-G→F2-H**) or the carbonate group (step **F2-G→F2-I**). The latter presents the highest activation barrier obtained thus far ($\Delta G^{\ddagger}$(**F2-G→F2-I**) = 7.5 kcal/mol) and is kinetically the least favorable process, reinforcing the evidence of the decrease in the hydridic character of the α-H atom to the carbonate. From **F2-G**, a HAT from the α-H atom to the hydroxyl group presents the lowest obtained activation barrier from the computed steps, being 0.5 kcal/mol lower than the barrier of step **F2-E→F2-F** ($\Delta G^{\ddagger}$(**F2-G→F2-H**) = 4.2 kcal/mol). Similarly to the structure of **F2-E**, the carbonated diol can establish a strong H-bond between the carbonate and the hydroxyl group. This interaction is a major stabilization factor of the transition state structure $\mathbf{TS_{F2\text{-}GH}}$. It is responsible for the increase in the hydridic character of the α-hydrogen atom involved in this HAT step.

The results thus far suggest that the activation mechanism for the alkylation of diols and alcohols should be different, and the initially proposed mechanism for the ternary catalytic system is incorrect. The combination of computational results and ^{1}H NMR experiments clearly shows that the HAT occurs from the α-H atom to the alcohol. To further verify this new mechanistic hypothesis, a new energy profile was computed for the combination of HAT and C-C coupling steps(Figure HAT-3).

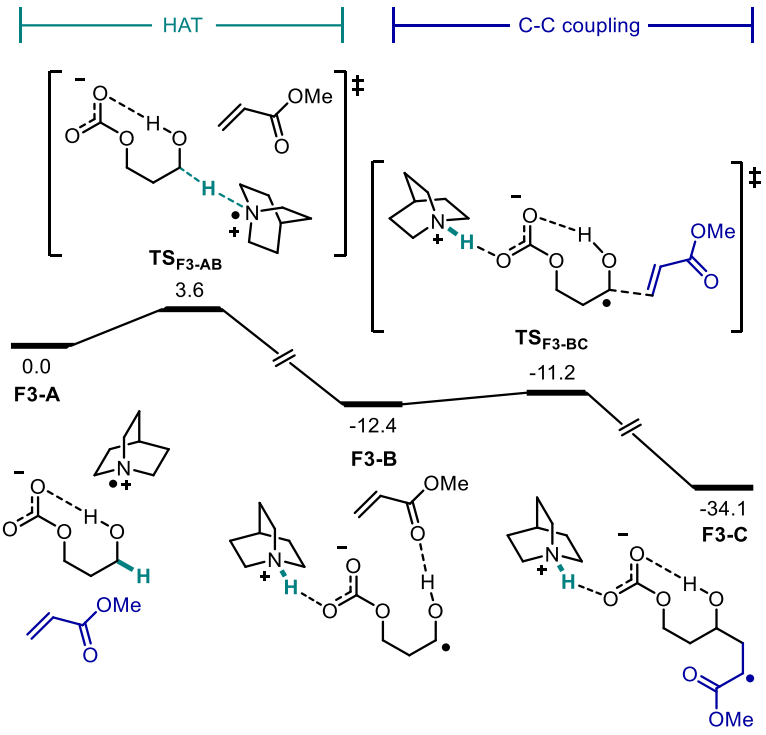

*Figure HAT-3 - Computed Gibbs free energy profile for HAT step from carbonated propanediol, followed by a C-C coupling event. The reactant complex **F3-A** serves as a reference (0.0 kcal/mol).*

The energy profile starts from the reactant complex **F3-A**, composed of the quinuclidinium radical, methyl acrylate and the carbonated 1,3-propanediol. As discussed before (Figure HAT-2), the intramolecular H-bond between the carbonate and the hydroxy group activates the α-H atom to the hydroxy, which undergoes a HAT step with a low barrier ($\Delta G^{\ddagger}$(**F3-A→F3-B**) = 3.6 kcal/mol) to yield the ketyl radical intermediate **F3-B**. This step is followed by a carbon-carbon coupling between the alkyl radical intermediate and the methyl acrylate that generates a radical intermediate **F3-C**. The C-C coupling presents an inferior activation barrier than the HAT step ($\Delta G^{\ddagger}$(**F3-B→F3-C**) = 1.2 kcal/mol), strongly suggesting that it is not a rate-limiting process within the catalytic system. The following steps of the mechanism were not computed due to the high complexity of computational approaches to study SET events and the large dimension of the Iridium catalyst. Nonetheless, the expected mechanism leading to the lactonization from the radical intermediate **S7-1** is presented in Scheme HAT-7. From **S7-1**, an electron transfer step generates a basic intermediate **S7-2**, which, after protonation, can form the carbonated lactone intermediate **S7-4** through an intramolecular nucleophilic attack with the release of methanol. This step involves a proton transfer and is likely assisted by water, which justifies the low yield of the reaction obtained in the absence of this proton shuttle (Scheme HAT-2-B, entry 5). Finally,

the carbonate can be converted back to a hydroxy group to yield the experimentally obtained product **S7-5**.

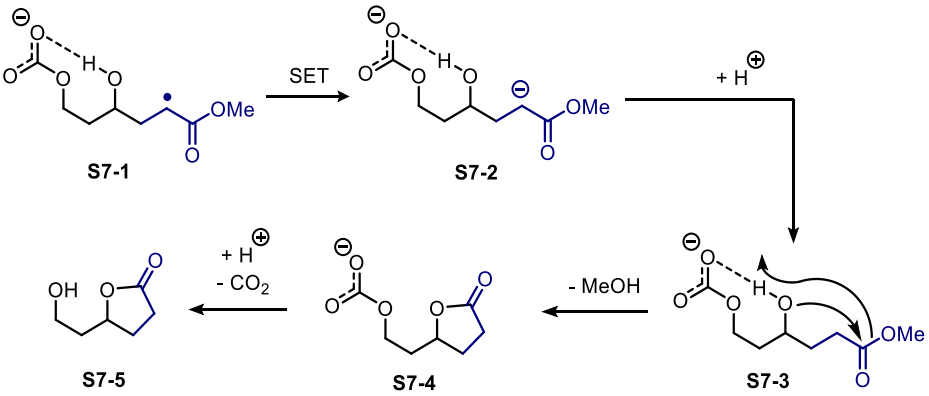

Scheme HAT-7 – Proposed mechanism leading from the radical intermediate formed after the C-C coupling step to the experimentally observed lactone product.

The kinetic favorability of the C-C coupling to the HAT step was verified with diols of different chain lengths (Figure HAT-4). To this end, the activation barrier of the C-C coupling between methyl acrylate and carbonated diol radicals with 2, 3 and 4 carbons in the connecting alkyl chain was computed. It is worth mentioning that the studied experimental conditions are suitable for activating diols with even longer chains, as demonstrated by the scope entries **S4-3o-t** in Scheme HAT-4. It is conceivable that a strong intramolecular H-bond between the hydroxyl and the anionic carbonate fragment is the major HAT activation factor of these substrates, remaining in place despite long and flexible linear alkyl chains connecting these two groups, as demonstrated in the structure of **F4-0n**.

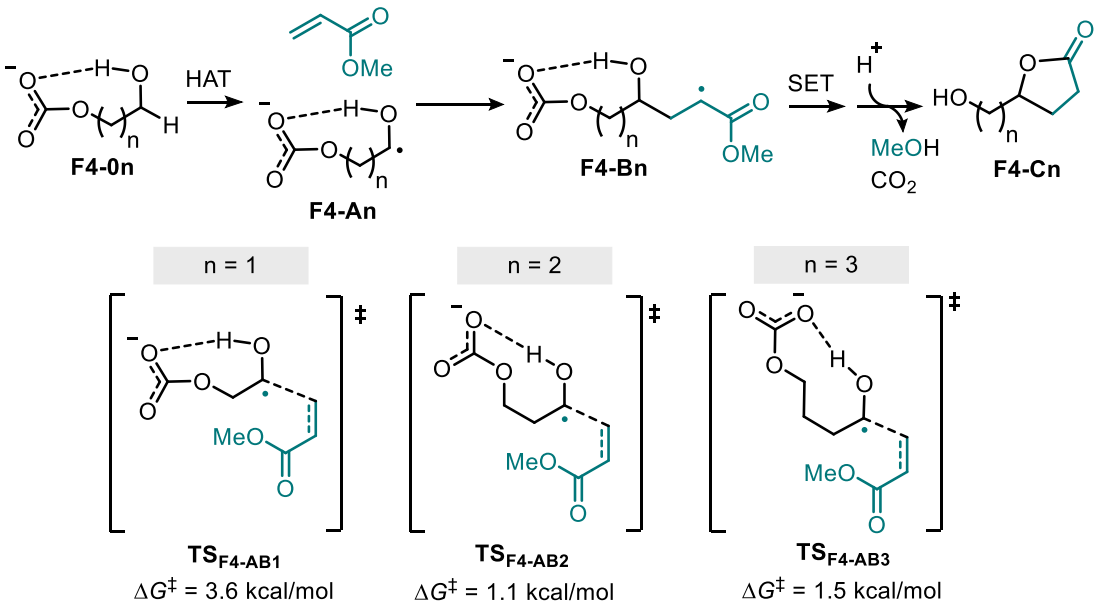

*Figure HAT-4 – Computed activation barriers for C-C coupling steps occurring from diols with varying alkyl chain length. The reactant complexes **F4-An** serve as reference (0.0 kcal/mol).*

The C-C coupling step for the carbonated 1,2-ethanediol presents the highest activation barrier of the computed set ($\Delta G^{\ddagger}$(**F4-A1→F4-B1**) = 3.6 kcal/mol). For the carbonated 1,3-propanediol, the obtained barrier is consistent with the previously computed step comprising the quinuclidinium in the model system ($\Delta G^{\ddagger}$(**F4-A2→F4-B2**) = 1.1 kcal/mol compared to $\Delta G^{\ddagger}$(**F3-B→F3-C**) = 1.2 kcal/mol in Figure HAT-3). A further increase in chain length results in a very small increase in the activation barrier, observed for the C-C coupling event of the carbonated 1,4-butanediol ($\Delta G^{\ddagger}$(**F4-A3→F4-B3**) = 1.5 kcal/mol). The higher activation barrier obtained for step **F4-A1→F4-B1** (1,2-diol) is likely due to the steric clash between the carbonate group and the methyl acrylate, which lie close to each other in $\mathbf{TS_{F4\text{-}AB1}}$ but not during C-C couplings of substrates with longer chains.

Facing these results, it is possible to re-design the proposed catalytic cycle for the general reactivity of the studied transformation, including the activation of the α-H atom of the hydroxyl group after CO_2 incorporation. The alterations to the initially proposed mechanism are highlighted in red in Scheme HAT-8. After the carbonation of the starting material **S8-1**, forming **S8-A**, the HAT occurs from the activated hydrogen atom, leading to intermediate **S8-B** and follows through with a sequence of C-C coupling, SET and cyclization steps to yield the lactone product **S8-3** and regenerating CO_2.

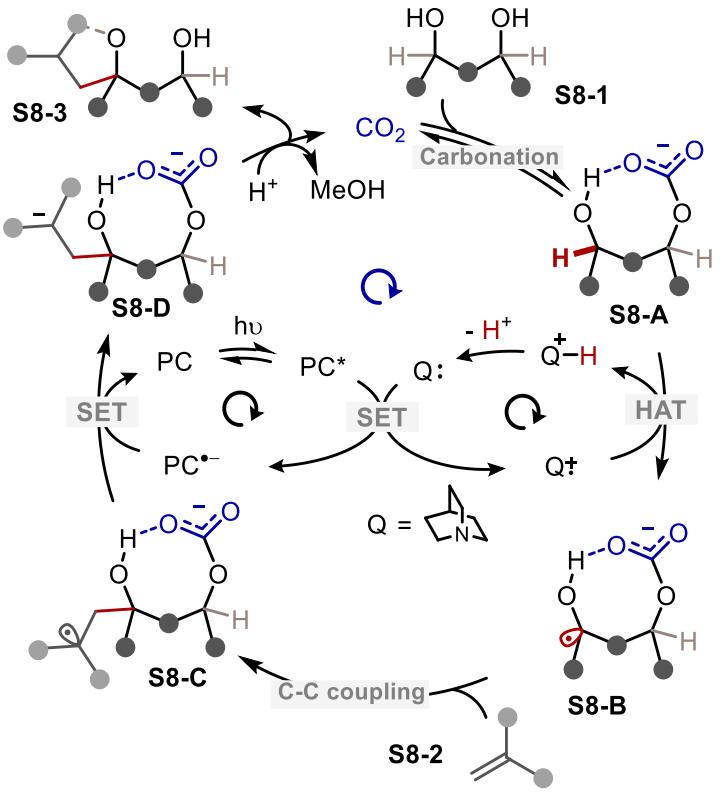

Scheme HAT-8 – Revisited mechanism for the ternary catalytic cycle of the alkylation reaction.

Following this mechanistic hypothesis, the experimentally obtained diastereoselectivity of the alkylation of the 1,2-cyclohexanol was revisited. Nearly the same yield and diastereomeric ratio of *cis*- and *trans*-lactone **S4-3j** (Scheme HAT-4) was observed using either the *cis*- or the *trans*-cyclic diol as starting material (Figure HAT-5). According to the new mechanistic proposal, with the HAT occurring from the α-H atom to the hydroxyl group, either the *cis*- (**F5-1cis**) or *trans*- (**F5-1trans**) diol are converted into the same radical intermediate, **F5-A**. This species can undergo a diastereoselectivity-determining C-C coupling step with methyl acrylate, which leads either to a radical intermediate with the carbonate and the hydroxy groups in *cis*- (**F5-Bcis**) or *trans*- (**F5-Btrans**) position. The higher selectivity towards the **F5-Bcis** results from a slightly lower activation barrier ($\Delta G^{\ddagger}$(**F5-A→F5-Bcis**) = 3.1 kcal/mol while $\Delta G^{\ddagger}$(**F5-A→F5-Btrans**) = 3.5 kcal/mol), that results from a reduced steric clash between the carbonate group and the methyl acrylate, as it was observed for linear 1,2-diols (Figure HAT-4, $\mathbf{TS_{F4\text{-}AB1}}$). The newly proposed mechanism, therefore, explains the experimentally observed diastereoselectivity for the formation of **S4-3j** (Scheme HAT-4) and is also in line with the C-C coupling not being a rate-limiting step since it presents low activation barriers even for conformationally strained systems.

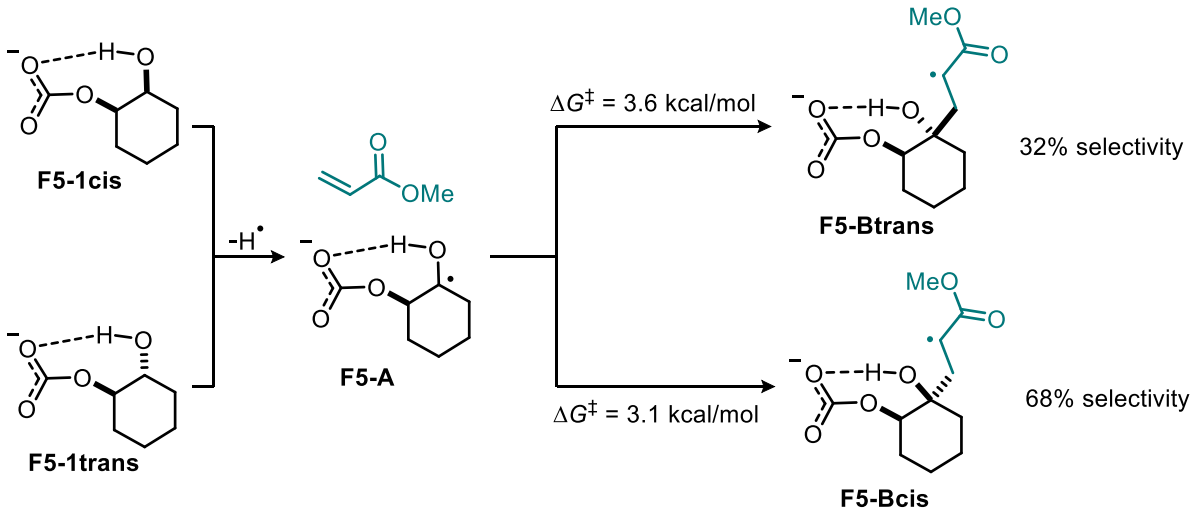

*Figure HAT-5 – Computed activation barriers for the diverged diastereomeric pathways in the C-C coupling during the alkylation of 1,2-hexanediol. The reactant complex **F5-A** serves as a reference (0.0 kcal/mol).*

5.4. α-C-H activation in alcohols

Finally, the HAT activation mechanism was investigated for simple alcohols. It was already shown that the α-H atom to the carbonate is less hydridic and therefore deactivated for the HAT step, and consequently, it is required to understand how the CO_2 incorporation is still able to catalyze the reaction. A Gibbs free energy profile was obtained for the HAT and subsequent C-C coupling event from propanol (Figure HAT-6-A) and carbonated propanol (Figure HAT-6-B).

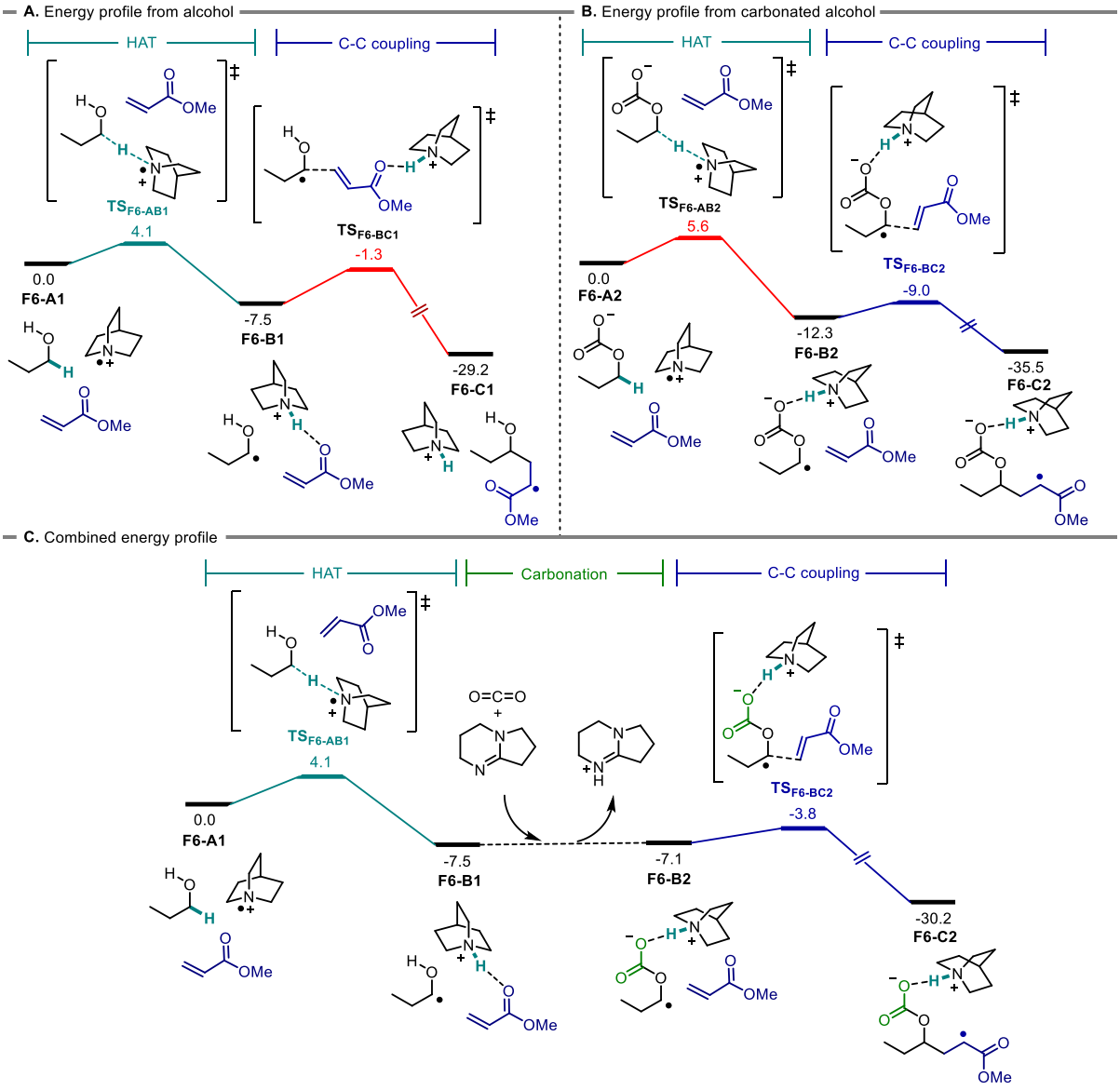

*Figure HAT-6 - Computed Gibbs free energy profile for the HAT step, followed by a C-C coupling event for: A) Propanol; B) Carbonated propanol; C) Combined energy profile showing the lowest-energy pathway that can be obtained. The reactant complexes **F6-A1** and **F6-A2** serve as reference (0.0 kcal/mol) for each profile.*

From the reactant complex consisting of quinuclidinium radical, methyl acrylate and propanol, **F6-A1**, an α-HAT step leads to the ketyl radical intermediate **F6-B1**. This transformation was also computed without the presence of the methyl acrylate in the computational model, as discussed previously (step **F2-A→F2-B** in Figure HAT-2). Interestingly, the subsequent C-C coupling step, **F6-B1→F6-C1**, presents a higher activation barrier than the preceding HAT ($\Delta G^{\ddagger}$(**F6-A1→F6-B1**) = 4.1 kcal/mol while $\Delta G^{\ddagger}$(**F6-B1→F6-C1**) = 6.2 kcal/mol), which makes the C-C coupling the rate-limiting step of the computed transformation. The thermodynamic destabilization of $\mathbf{TS_{F6\text{-}BC1}}$ is likely due to a strong H-bond between the carbonyl moiety of the methyl acrylate and the quinuclidinium. It leads to a decrease

in the electron-rich character of the terminal alkene, responsible for the homolytic bond formation. After the carbonation of the alcohol, from which the reactant complex **F6-A2** can be considered, the HAT step is 1.5 kcal/mol less favorable ($\Delta G^{\ddagger}$(**F6-A2→F6-B2**) = 4.1 kcal/mol), similarly to the results obtained for the same step without including methyl acrylate in the computational model (step **F2-C→F2-D** is 1.8 less favored than step **F2-A→F2-B** in Figure HAT-2) resulting from the decrease in hydridic character of the α-H atom. Step **F6-A2→F6-B2** is also more exergonic than **F6-A1→F6-B1** due to the stabilization of the ketyl radical intermediate **F6-B2** (ΔG(**F6-A2→F6-B2**) = -12.3 kcal/mol while ΔG(**F6-A1→F6-B1**) = -7.5 kcal/mol). The computed barrier for the C-C coupling of the carbonated alcohol reveals that the carbonation affects not only the activation of the HAT step but also the C-C coupling step. In $\mathbf{TS_{F6\text{-}BC2}}$, the quinuclidinium cation establishes an H-bond with the most electron-negative fragment of the system, which is the carbonate group. As a result, on the one hand, the ketyl radical becomes more electron deficient due to the induction of the carbonate acting as an H-bond acceptor, and on the other, the methyl acrylate becomes free to undergo homolytic bond formation with the ketyl radical, without the inference of an H-bond between the carbonyl and the quinuclidinium, as observed in the less favorable transition state $\mathbf{TS_{F6\text{-}AB1}}$. In this profile, the HAT is the rate-limiting step, imposing an apparent activation barrier of 5.6 kcal/mol, which is lower than the apparent activation barrier obtained for the profile with the alcohol ($\Delta G^{\ddagger}$(**F6-B1→F6-C1**) = 6.2 kcal/mol). These results show that even though the CO_2 incorporation may deactivate the HAT step, this effect is countered by the facilitation of the C-C coupling. Thus, it is even possible to obtain a profile with the most kinetically favored steps of both profiles (Figure HAT-6-C). This mechanistic pathway would involve the HAT from the non-deactivated alcohol, step **F6-A1→F6-B1**, followed by CO_2 incorporation, promoted by DBN. This carbonation is slightly endergonic (ΔG(**F6-B1→F6-B2**) = 0.4 kcal/mol) and is followed by the facilitated C-C coupling of the carbonated ketyl radical and methyl acrylate, step **F6-B2→F6-C2**. The apparent activation barrier of the C-C coupling can then be determined by the difference in relative Gibbs free energy of **F6-B1** and $\mathbf{TS_{F6\text{-}BC2}}$ ($\Delta G^{\ddagger}$(**F6-B1→F6-C2**) = 3.7 kcal/mol), which is still lower than the activation barrier of the HAT step ($\Delta G^{\ddagger}$(**F6-A1→F6-B1**) = 4.1 kcal/mol), resulting in the latter to become the rate-limiting step.

The obtained computational data shows that the studied ternary catalytic system presents different reaction mechanisms for alcohols and diols. While alcohols only benefit from the incorporation of CO_2 to facilitate the C-C coupling step, diols have full benefit from the carbonation of one hydroxyl group, which lowers the kinetic barrier of both the HAT and the C-C coupling steps. The computational studies performed in this work were then able to shed light on the factors activating the HAT activation of alcohols and diols, as shown in Scheme HAT-9. While the carbonation deactivates the α-H atom by reducing its hydridic character, the intramolecular H-bond present in diols is enhanced with the introduction of an anion H-bond acceptor moiety, activating the α-H atom to the H-bond donor hydroxyl group.

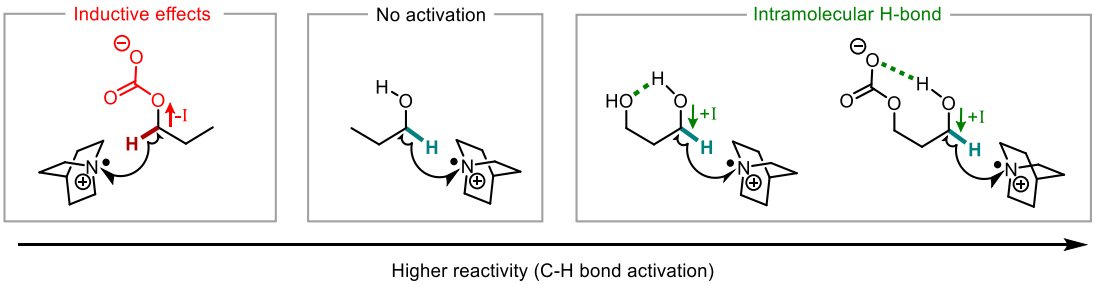

Scheme HAT-9 – Schematic representation of the C-H activation effects observed in alcohols and diols within the studied catalytic system.

5.5. Conclusions and outlook

In this chapter, the factors affecting the activation of a C-H bond in a photocatalytic system that promotes the alkylation of symmetric polyols were studied. It was observed that the incorporation of CO_2 gas would increase the rate of product formation in the considered reaction. The initially proposed catalytic cycle was refined through computational analysis, uncovering that a strong intramolecular H-bond is key to activating the α-C-H bond of an alcohol group, leading to a more efficient homolytic cleavage.

The revised mechanistic model also allowed us to explain other experimental observations, such as ^{1}H NMR spectra and diastereoselectivities observed in cyclic product formations. Furthermore, our investigation into the alkylation of alcohols under the same catalytic system sheds light on the role of CO_2 in the reaction mechanism.

Once more, the insights gained from elucidating the mechanism suggest adaptations to the experimental conditions that could enhance the reaction's efficiency. Specifically, our results indicate that introducing electron-withdrawing groups into alcohols could allow efficient C-H activation via H-bonding to the hydroxyl group.

6. General conclusions

The computational work presented in this dissertation was conducted in close collaboration with experimental efforts, providing a complementary perspective to advance the understanding of various metal-free C-H activation processes.

One of the key contributions of this work is the elucidation of factors influencing hydride shifts in carbocationic systems. Computational investigations revealed a clear preference for [1,2]-hydride shifts over the less favorable [1,3]- and [1,4]-hydride shifts. The reaction mechanism of an enantioselective Lewis acid-catalyzed coupling of alkenes and aldehydes was also investigated, uncovering a *trans*-annular [1,5]-hydride shift step responsible for the observed selectivity.

In the study of the cationic cyclopropanation process that converts cyclic dienes into 6,8-cycloeudesmanes, this work identified a protonated cyclopropane intermediate–a crucial yet highly unstable species involved in cyclopropane ring formation. Due to its instability, this intermediate could only be explored computationally. A predictive computational framework was developed to assess reaction outcomes with different substrates, including the verification of a concerted step leading to this intermediate. These computational insights were pivotal in steering experimental efforts toward substrates that yielded better results while evaluating the effects of functional group modifications. Moreover, this approach helped to identify reactions unlikely to succeed experimentally, thereby saving valuable resources and time.

The alkylation of polyols to form lactams within a ternary catalytic system involving the reversible incorporation of CO_2 was also investigated. Computational studies clarified the role of CO_2 incorporation into polyols and alcohols, providing a detailed understanding of two critical reaction steps: hydrogen atom transfer and C-C coupling. The findings highlighted the significance of an intramolecular hydrogen bond, facilitated by CO_2 incorporation, as a key factor in enhancing the catalytic activity of the system.

These studies significantly contribute to the broader field of C-H activation, providing fundamental insights and computational methodologies that can aid in developing future processes. This work

highlights the vital role of computational chemistry as a guiding tool in advancing experimental organic chemistry and exemplifies the potential for innovation through interdisciplinary collaboration.

7. List of publications

Although this thesis focuses solely on the projects involving C-H activation, the following list contains all the publications resulting from the work developed in several additional projects during the stay at the Institutes of Organic Chemistry and Theoretical Chemistry, including the three published works deriving from the work presented in this thesis (entries 6, 10 and 15):

1. H. Chuang, M. Schupp, **R. Meyrelles**, B. Maryasin, N. Maulide, „*Redox-Neutral Selenium-Catalyzed Isomerisation of para-Hydroxamic Acids into para-Aminophenols*", Angew. Chem. 60, 13778-13782, (**2021**)

a. Cover Image: *Angew. Chem.* 60, (**2021**)

2. M. Lemmerer, M. Riomet, **R. Meyrelles**, B. Maryasin, L. González, N. Maulide, "*HFIP Mediates a Direct C-C Coupling Between Michael Acceptors and Eschenmoser's Salt*", Angew. Chem. Int. Ed. 61, e202109933, (**2022**)
3. J. Merad, P. Grant, T. Stopka, J. Sabbatani, **R. Meyrelles**, A. Preinfalk, J. Matyasovsky, B. Maryasin, L. González, N. Maulide, "*Direct Stereodivergent Olefination of Carbonyl Compounds with Sulfur Ylides*", J. Am. Chem. Soc. 144, 12536–12543, (**2022**)
4. M. Feng, R. Tinelli, R. **Meyrelles**, L. González, B. Maryasin, N. Maulide, "*Direct Synthesis of α-Amino Acid Derivatives via Hydrative Amination of Alkynes*", Angew. Chem. Int. Ed. 62, e202212399, (**2022**)
5. R. Meyrelles, Y. Fetisleam, B. Maryasin, "*Computational Investigation of the Aza-Cope Rearrangement Leading to Angularly Substituted 1-Azabicyclic Rings*", Synlett 34(05): 437-440 (**2023**)
6. P. S. Grant‡, **R. Meyrelles**‡, O. Gajsek, G. Niederacher, B. Maryasin, N. Maulide, "*Biomimetic Cationic Cyclopropanation Enables an Efficient Chemoenzymatic Synthesis of 6,8-Cycloeudesmanes*", J. Am. Chem. Soc. 145, 5855–5863, (**2023**)
7. M. Feng, A. J. Fernandes, **R. Meyrelles**, N. Maulide, "*Direct Enantioselective α-Amination of Amides Guided by DFT Prediction of E/Z Selectivity in a Sulfonium Intermediate*", Chem 9, 1538–1548, (**2023**)

8. P. Spieß, A. Sirvent, I. Tiefenbrunner, J. Sargueil, A. J. Fernandes, A. Arroyo-Bondía, **R. Meyrelles**, D. Just, A. Prado-Roller, S. Shaaban, D. Kaiser, N. Maulide, "*Nms-sulfonamide: a New Amine Protecting Group enables Unique Stability and Selectivity*", Chem. Eur. J. 29, e202301312, (**2023**)
9. **R. Meyrelles**, M. Schupp, B. Maryasin, "*Mechanistic Study on Selenium- and Sulfur-mediated Isomerisation of Hydroxamic Acids*", Chem. Eur. J. , e202302386, (**2023**)
10. G. Archer‡, **R. Meyrelles**‡, I. Eder, N. Kovács, B. Maryasin, M. Médebielle, J. Merad, *„Photoredox-Catalyzed α-C-H Monoalkylation of Symmetric Polyols in the Presence of CO_2*", Angew. Chem. Int. Ed. , e202315329, (**2023**)
11. J. Hipólito, **R. Meyrelles**, B. Maryasin, L. G. Alves, A. M. Martins, "*Reactions of Heteroallenes with Salan-based Ti(IV) Complexes: A Joint Experimental and Computational Study*", Chem. Asian J. , e202400165, (**2024**)
12. P. Spiess, J. Brześkiewicz, **R. Meyrelles**, D. Just, N. Maulide,"*Deprotective Functionalization: a Direct Conversion of Nms-Amides to Carboxamides Using Carboxylic Acids*", Angew. Chem. Int. Ed. , e202318304, (**2024**)
13. P. S. Grant*, M. Vavrík*, V. Porte‡, **R. Meyrelles**‡, N. Maulide, "*Remote Proton Elimination: C–H Activation Enabled by Distal Acidification*", Science 384, 815-820, **(2024**)
14. K. Song, **R. Meyrelles**, G. Pilet, B. Maryasin, M. Médebielle, J. Merad, "*Dication Disulfuranes as Photoactivatable Sources of Radical Organocatalysts*", Angew. Chem. Int. Ed. , 64, e202419751, (**2024**)
15. **R. Meyrelles**, B. R. Brutiu, B. Maryasin, "*Computational Insights into the Mechanism of Lewis Acid-Catalyzed Alkene-Aldehyde Coupling*", ChemPlusChem, , e202400751, (**2025**)
16. G. Iannelli, P. Spieß, **R. Meyrelles**, D. Kaiser, L. González, N. Maulide, "*Diastereoselective Umpolung Cyclisation of Ketones Promoted by Hypervalent Iodine*", (submitted), (**2025**)

8. References

[1] A. S. Goldman, K. I. Goldberg, in *Act. Funct. C—H Bonds*, American Chemical Society, **2004**, pp. 1–43.

[2] T. Rogge, N. Kaplaneris, N. Chatani, J. Kim, S. Chang, B. Punji, L. L. Schafer, D. G. Musaev, J. Wencel-Delord, C. A. Roberts, R. Sarpong, Z. E. Wilson, M. A. Brimble, M. J. Johansson, L. Ackermann, *Nat. Rev. Methods Primer* **2021**, *1*, 1–31.

[3] J. Chatt, J. M. Davidson, *J. Chem. Soc. Resumed* **1965**, 843–855.

[4] R. H. Crabtree, *J. Chem. Soc. Dalton Trans.* **2001**, 2437–2450.

[5] R. H. Crabtree, A. Lei, *Chem. Rev.* **2017**, *117*, 8481–8482.

[6] C. Jia, T. Kitamura, Y. Fujiwara, *Acc. Chem. Res.* **2001**, *34*, 633–639.

[7] S. J. Tremont, H. U. Rahman, *J. Am. Chem. Soc.* **1984**, *106*, 5759–5760.

[8] J. He, M. Wasa, K. S. L. Chan, Q. Shao, J.-Q. Yu, *Chem. Rev.* **2017**, *117*, 8754–8786.

[9] S. G. Ouellet, A. Roy, C. Molinaro, R. Angelaud, J.-F. Marcoux, P. D. O'Shea, I. W. Davies, *J. Org. Chem.* **2011**, *76*, 1436–1439.

[10] T. Dalton, T. Faber, F. Glorius, *ACS Cent. Sci.* **2021**, *7*, 245–261.

[11] J. Zhao, T. Nanjo, E. C. de Lucca, M. C. White, *Nat. Chem.* **2019**, *11*, 213–221.

[12] J. Kweon, S. Chang, *Angew. Chem. Int. Ed.* **2021**, *60*, 2909–2914.

[13] S. Roy, S. Panja, S. R. Sahoo, S. Chatterjee, D. Maiti, *Chem. Soc. Rev.* **2023**, *52*, 2391–2479.

[14] A. Shamsabadi, V. Chudasama, *Org. Biomol. Chem.* **2019**, *17*, 2865–2872.

[15] L. Shi, T. Li, G.-J. Mei, *Green Synth. Catal.* **2022**, *3*, 227–242.

[16] Y. Bai, W. Yu, R. Chen, G. Yu, B. Wei, *Green Synth. Catal.* **2024**, DOI 10.1016/j.gresc.2024.04.007.

[17] V. Chudasama, R. J. Fitzmaurice, S. Caddick, *Nat. Chem.* **2010**, *2*, 592–596.

[18] M. Pastor, M. Vayer, H. Weinstabl, N. Maulide, *J. Org. Chem.* **2022**, *87*, 606–612.

[19] S. Shaaban, A. Roller, N. Maulide, *Eur. J. Org. Chem.* **2015**, *2015*, 7643–7647.

[20] P. S. Grant, M. Vavrík, V. Porte, R. Meyrelles, N. Maulide, *Science* **2024**, *384*, 815–820.

[21] T. Rogge, Q. Zhou, N. J. Porter, F. H. Arnold, K. N. Houk, *J. Am. Chem. Soc.* **2024**, *146*, 2959–2966.

[22] A. Ghosh, J. T. Yarranton, J. K. McCusker, *Nat. Chem.* **2024**, 1–8.

[23] E. G. Lewars, *Computational Chemistry: Introduction to the Theory and Applications of Molecular and Quantum Mechanics*, Springer International Publishing, Cham, **2024**.

[24] S. K. De, *Applied Organic Chemistry: Reaction Mechanisms and Experimental Procedures in Medicinal Chemistry*, Wiley, **2021**.

[25] Q. Peng, F. Duarte, R. S. Paton, *Chem. Soc. Rev.* **2016**, *45*, 6093–6107.

[26] T. Sperger, I. A. Sanhueza, F. Schoenebeck, *Acc. Chem. Res.* **2016**, *49*, 1311–1319.

[27] F. Jensen, *Introduction to Computational Chemistry*, John Wiley & Sons, Chichester, UK ; Hoboken, NJ, **2017**.

[28] M. Born, R. Oppenheimer, *Ann. Phys.* **1927**, *389*, 457–484.

[29] D. R. Hartree, *Math. Proc. Camb. Philos. Soc.* **1928**, *24*, 89–110.

[30] J. P. Perdew, in *AIP Conf. Proc.*, AIP, Antwerp (Belgium), **2001**, pp. 1–20.

[31] Chr. Møller, M. S. Plesset, *Phys. Rev.* **1934**, *46*, 618–622.

[32] S. F. Sousa, P. A. Fernandes, M. J. Ramos, *J. Phys. Chem. A* **2007**, *111*, 10439–10452.

[33] In *Chem. Guide Density Funct. Theory*, John Wiley & Sons, Ltd, **2001**, pp. 33–40.

[34] J.-L. Calais, *Int. J. Quantum Chem.* **1993**, *47*, 101–101.

[35] J. A. Pople, P. M. W. Gill, B. G. Johnson, *Chem. Phys. Lett.* **1992**, *199*, 557–560.

[36] R. G. Parr, S. R. Gadre, L. J. Bartolotti, *Proc. Natl. Acad. Sci.* **1979**, *76*, 2522–2526.

[37] D. C. Langreth, J. P. Perdew, *Phys. Rev. B* **1980**, *21*, 5469–5493.

[38] D. C. Langreth, M. J. Mehl, *Phys. Rev. B* **1983**, *28*, 1809–1834.

[39] A. D. Becke, *Phys. Rev. A* **1988**, *38*, 3098–3100.

[40] C. Lee, W. Yang, R. G. Parr, *Phys. Rev. B* **1988**, *37*, 785–789.

[41] J. P. Perdew, K. Burke, M. Ernzerhof, *Phys. Rev. Lett.* **1996**, *77*, 3865–3868.

[42] J. P. Perdew, *Phys. Rev. B* **1986**, *33*, 8822–8824.

[43] M. Bursch, J.-M. Mewes, A. Hansen, S. Grimme, *Angew. Chem. Int. Ed.* **2022**, *61*, e202205735.

[44] A. D. Becke, *J. Chem. Phys.* **1993**, *98*, 5648–5652.

[45] M. T. de Oliveira, J. M. A. Alves, N. L. Vrech, A. A. C. Braga, C. A. Barboza, *Phys. Chem. Chem. Phys.* **2023**, *25*, 1903–1922.

[46] S. K. Nistanaki, C. G. Williams, B. Wigman, J. J. Wong, B. C. Haas, S. Popov, J. Werth, M. S. Sigman, K. N. Houk, H. M. Nelson, *Science* **2022**, *378*, 1085–1091.

[47] S. Grimme, J. Antony, S. Ehrlich, H. Krieg, *J. Chem. Phys.* **2010**, *132*, 154104.

[48] S. Grimme, S. Ehrlich, L. Goerigk, *J. Comput. Chem.* **2011**, *32*, 1456–1465.

[49] J. U. Reveles, A. M. Köster, *J. Comput. Chem.* **2004**, *25*, 1109–1116.

[50] D. A. McQuarrie, J. D. Simon, *Molecular Thermodynamics*, University Science Books, **1999**.

[51] J. W. Ochterski, *Gaussian, inc.* **2000**.

[52] Y. Wei, T. Singer, H. Mayr, G. N. Sastry, H. Zipse, *J. Comput. Chem.* **2008**, *29*, 291–297.

[53] J. A. Pople, M. Head-Gordon, D. J. Fox, K. Raghavachari, L. A. Curtiss, *J. Chem. Phys.* **1989**, *90*, 5622–5629.

[54] E. Cancès, B. Mennucci, J. Tomasi, *J. Chem. Phys.* **1997**, *107*, 3032–3041.

[55] A. V. Marenich, C. J. Cramer, D. G. Truhlar, *J. Phys. Chem. B* **2009**, *113*, 6378–6396.

[56] M. Rahbar, C. J. Stein, *J. Phys. Chem. A* **2023**, *127*, 2176–2193.

[57] T. I. U. of P. and A. Chemistry (IUPAC), "IUPAC - complex (C01203)," DOI 10.1351/goldbook.C01203can be found under https://goldbook.iupac.org/terms/view/C01203, **n.d.**

[58] M. G. Evans, M. Polanyi, *Trans. Faraday Soc.* **1935**, *31*, 875–894.

[59] S. Kozuch, S. Shaik, *Acc. Chem. Res.* **2011**, *44*, 101–110.

[60] H. Ryu, J. Park, H. K. Kim, J. Y. Park, S.-T. Kim, M.-H. Baik, *Organometallics* **2018**, *37*, 3228–3239.

[61] S. Grimme, *J. Chem. Theory Comput.* **2019**, *15*, 2847–2862.

[62] P. Pracht, F. Bohle, S. Grimme, *Phys. Chem. Chem. Phys.* **2020**, *22*, 7169–7192.

[63] S. Spicher, S. Grimme, *Angew. Chem. Int. Ed.* **2020**, *59*, 15665–15673.

[64] P. Pracht, F. Bohle, S. Grimme, *Phys. Chem. Chem. Phys.* **2020**, *22*, 7169–7192.

[65] M. J. Frisch, G. W. Trucks, H. B. Schlegel, G. E. Scuseria, M. A. Robb, J. R. Cheeseman, G. Scalmani, V. Barone, G. A. Petersson, H. Nakatsuji, X. Li, M. Caricato, A. V. Marenich, J. Bloino, B. G. Janesko, R. Gomperts, B. Mennucci, H. P. Hratchian, J. V. Ortiz, A. F. Izmaylov, J. L. Sonnenberg, Williams, F. Ding, F. Lipparini, F. Egidi, J. Goings, B. Peng, A. Petrone, T. Henderson, D. Ranasinghe, V. G. Zakrzewski, J. Gao, N. Rega, G. Zheng, W. Liang, M. Hada, M. Ehara, K. Toyota, R. Fukuda, J. Hasegawa, M. Ishida, T. Nakajima, Y. Honda, O. Kitao, H. Nakai, T. Vreven, K. Throssell, J. A. Montgomery Jr., J. E. Peralta, F. Ogliaro, M. J. Bearpark, J. J. Heyd, E. N. Brothers, K. N. Kudin, V. N. Staroverov, T. A. Keith, R. Kobayashi, J. Normand, K. Raghavachari, A. P. Rendell, J. C. Burant, S. S. Iyengar, J. Tomasi, M. Cossi, J. M. Millam, M. Klene, C. Adamo, R. Cammi, J. W. Ochterski, R. L. Martin, K. Morokuma, O. Farkas, J. B. Foresman, D. J. Fox, **2016**.

[66] C. Peng, H. Bernhard Schlegel, *Isr. J. Chem.* **1993**, *33*, 449–454.

[67] F. Weigend, R. Ahlrichs, *Phys. Chem. Chem. Phys.* **2005**, *7*, 3297–3305.

[68] A. D. Becke, E. R. Johnson, *J. Chem. Phys.* **2005**, *123*, 154101.

[69] J.-D. Chai, M. Head-Gordon, *Phys. Chem. Chem. Phys.* **2008**, *10*, 6615–6620.

[70] J. Tomasi, B. Mennucci, R. Cammi, *Chem. Rev.* **2005**, *105*, 2999–3094.

[71] R. Fittig, *Justus Liebigs Ann. Chem.* **1859**, *110*, 17–23.

[72] J. B. Sweeney, *Angew. Chem.* **2016**, *128*, 14132–14132.

[73] D. J. S. Sandbeck, D. J. Markewich, A. L. L. East, *J. Org. Chem.* **2016**, *81*, 1410–1415.

[74] R. G. Epton, A. K. Clarke, R. J. K. Taylor, W. P. Unsworth, J. M. Lynam, *Eur. J. Org. Chem.* **2019**, *2019*, 5563–5571.

[75] H. Xu, B. Goldfuss, J. S. Dickschat, *Chem. – Eur. J.* **2021**, *27*, 9758–9762.

[76] D. Kaldre, B. Maryasin, D. Kaiser, O. Gajsek, L. González, N. Maulide, *Angew. Chem. Int. Ed Engl.* **2017**, *56*, 2212–2215.

[77] B. Maryasin, D. Kaldre, R. Galaverna, I. Klose, S. Ruider, M. Drescher, H. Kählig, L. González, M. N. Eberlin, I. D. Jurberg, N. Maulide, *Chem. Sci.* **2018**, *9*, 4124–4131.

[78] P. Hoyos, J.-V. Sinisterra, F. Molinari, A. R. Alcántara, P. Domínguez de María, *Acc. Chem. Res.* **2010**, *43*, 288–299.

[79] B. R. Brutiu, G. Iannelli, M. Riomet, D. Kaiser, N. Maulide, *Nature* **2024**, *626*, 92–97.

[80] F. H. Allen, O. Kennard, D. G. Watson, L. Brammer, A. G. Orpen, R. Taylor, *J. Chem. Soc. Perkin Trans. 2* **1987**, S1–S19.

[81] B. R. Brutiu, Harnessing Carbocations for the Remote Functionalization of Alkenes and Silyl Enol Ethers, PhD Thesis, University of Vienna, **2024**.

[82] T. I. U. of P. and A. Chemistry (IUPAC), “IUPAC - chair, boat, twist (C00964),” DOI 10.1351/goldbook.C00964can be found under https://goldbook.iupac.org/terms/view/C00964, **n.d.**

[83] J. Li, A. Preinfalk, N. Maulide, *Angew. Chem. Int. Ed.* **2019**, *58*, 5887–5890.

[84] J. Li, A. Preinfalk, N. Maulide, *J. Am. Chem. Soc.* **2019**, *141*, 143–147.

[85] R. Meyrelles, B. R. Brutiu, B. Maryasin, *ChemPlusChem* **2025**, e202400751.

[86] K. D. Nguyen, B. Y. Park, T. Luong, H. Sato, V. J. Garza, M. J. Krische, *Science* **2016**, *354*, aah5133.

[87] M. Holmes, L. A. Schwartz, M. J. Krische, *Chem. Rev.* **2018**, *118*, 6026–6052.

[88] A. E. Wright, J. C. Botelho, E. Guzmán, D. Harmody, P. Linley, P. J. McCarthy, T. P. Pitts, S. A. Pomponi, J. K. Reed, *J. Nat. Prod.* **2007**, *70*, 412–416.

[89] J. Yu, N. Q. Su, W. Yang, *JACS Au* **2022**, *2*, 1383–1394.

[90] P. S. Grant, R. Meyrelles, O. Gajsek, G. Niederacher, B. Maryasin, N. Maulide, *J. Am. Chem. Soc.* **2023**, *145*, 5855–5863.

[91] C. Ebner, E. M. Carreira, *Chem. Rev.* **2017**, *117*, 11651–11679.

[92] W. Wu, Z. Lin, H. Jiang, *Org. Biomol. Chem.* **2018**, *16*, 7315–7329.

[93] L. A. Wessjohann, W. Brandt, T. Thiemann, *Chem. Rev.* **2003**, *103*, 1625–1648.

[94] H. E. Simmons, R. D. Smith, *J. Am. Chem. Soc.* **1958**, *80*, 5323–5324.

[95] J. Furukawa, N. Kawabata, J. Nishimura, *Tetrahedron* **1968**, *24*, 53–58.

[96] W. von E. Doering, A. K. Hoffmann, *J. Am. Chem. Soc.* **1954**, *76*, 6162–6165.

[97] A. B. Sanford, T. A. Thane, T. M. McGinnis, P.-P. Chen, X. Hong, E. R. Jarvo, *J. Am. Chem. Soc.* **2020**, *142*, 5017–5023.

[98] C. J. Collins, *Chem. Rev.* **1969**, *69*, 543–550.

[99] J. K. Lee, K. N. Houk, *Angew. Chem. Int. Ed. Engl.* **1997**, *36*, 1003–1005.

[100] Y. J. Hong, D. J. Tantillo, *J. Org. Chem.* **2007**, *72*, 8877–8881.

[101] T. Ll, K. D. Janda, R. A. Lerner, *Nature* **1996**, *379*, 326–327.

[102] A. Bauer, G. Di Mauro, J. Li, N. Maulide, *Angew. Chem.* **2020**, *132*, 18365–18369.

[103] S.-H. Chen, S. Huang, V. Farina, *Tetrahedron Lett.* **1994**, *35*, 41–44.

[104] D. E. Cane, J. K. Sohng, P. G. Williard, *J. Org. Chem.* **1992**, *57*, 844–851.

[105] Q. Liu, G. Yue, N. Wu, G. Lin, Y. Li, J. Quan, C. Li, G. Wang, Z. Yang, *Angew. Chem.* **2012**, *124*, 12238–12242.

[106] G. Guella, D. Skropeta, I. Mancini, F. Pietra, *Z. Für Naturforschung B* **2002**, *57*, 1147–1151.

[107] G. Archer, R. Meyrelles, I. Eder, N. Kovács, B. Maryasin, M. Médebielle, J. Merad, *Angew. Chem. Int. Ed.* **2024**, *63*, e202315329.

[108] A. N. Marchesan, M. P. Oncken, R. M. Filho, M. R. W. Maciel, *Green Chem.* **2019**, *21*, 5168–5194.

[109] O. Gómez-Jiménez-Aberasturi, J. R. Ochoa-Gómez, *J. Chem. Technol. Biotechnol.* **2017**, *92*, 705–711.

[110] X. Liu, X. Wang, S. Yao, Y. Jiang, J. Guan, X. Mu, *RSC Adv.* **2014**, *4*, 49501–49520.

[111] L. Capaldo, D. Ravelli, *Eur. J. Org. Chem.* **2017**, *2017*, 2056–2071.

[112] L. Capaldo, D. Ravelli, M. Fagnoni, *Chem. Rev.* **2022**, *122*, 1875–1924.

[113] A. Matsumoto, M. Yamamoto, K. Maruoka, *ACS Catal.* **2022**, *12*, 2045–2051.

[114] J. Twilton, M. Christensen, D. A. DiRocco, R. T. Ruck, I. W. Davies, D. W. C. MacMillan, *Angew. Chem. Int. Ed.* **2018**, *57*, 5369–5373.

[115] W. Xu, Q. Shao, C. Xia, Q. Zhang, Y. Xu, Y. Liu, M. Wu, *Chem. Sci.* **2023**, *14*, 916–922.

[116] S. Paul, D. Filippini, F. Ficarra, H. Melnychenko, C. Janot, M. Silvi, *J. Am. Chem. Soc.* **2023**, *145*, 15688–15694.

[117] J. A. Turner, T. Adrianov, M. S. Taylor, *J. Org. Chem.* **2023**, *88*, 5713–5730.

[118] H. Nakao, H. Mitsunuma, M. Kanai, *Chem. Pharm. Bull. (Tokyo)* **2022**, *70*, 540–543.

[119] J. Ye, I. Kalvet, F. Schoenebeck, T. Rovis, *Nat. Chem.* **2018**, *10*, 1037–1041.

[120] P. K. Sahoo, Y. Zhang, S. Das, *ACS Catal.* **2021**, *11*, 3414–3442.

[121] Y. Wei, B. Sateesh, B. Maryasin, G. N. Sastry, H. Zipse, *J. Comput. Chem.* **2009**, *30*, 2617–2624.